Title	Phase Behavior and Dynamics of Tetramethylsilane Condensed Phase at Mono-and Multilayer Coverages Adsorbed on Solid Surfaces
Author(s)	崎里, 直己
Citation	大阪大学, 2002, 博士論文
Version Type	VoR
URL	https://hdl.handle.net/11094/269
rights	
Note	

DOCTORAL THESIS

PHASE BEHAVIOR AND DYNAMICS OF TETRAMETHYLSILANE CONDENSED PHASE AT MONO- AND MULTILAYER COVERAGES ADSORBED ON SOLID SURFACES

BY

NAOKI SAKISATO

DEPARTMENT OF CHEMISTRY
GRADUATE SCHOOL OF SCIENCE
OSAKA UNIVERSITY

2002

DOCTORAL THESIS

Phase Behavior and Dynamics of Tetramethylsilane Condensed Phase at Mono- and Multilayer Coverages Adsorbed on Solid Surfaces

by

Naoki Sakisato

Department of Chemistry
Graduate School of Science
Osaka University

2002

Doctoral Committee

Professor Takasuke Matsuo, Chairman
Professor Michio Sorai
Professor Toshio Kasai
Associate Professor Akira Inaba

Acknowledgements

The works described in this thesis have been carried out under the direction of Professor Takasuke Matsuo. I would like to express my sincere gratitude to Professor Matsuo for his patient guidance, kind encouragement and valuable discussions.

I am very grateful to Associate Professor Akira Inaba for his direct guidance and cooperation in the experiments, and his repeated encouragement, many critical advice and stimulated suggestions throughout the course of this work.

I would like to acknowledge Dr. Osamu Yamamuro for his valuable discussions.

I wish to acknowledge the members of the LAM group at KEK for technical assistance in performing neutron scattering experiments.

I also wish to acknowledge Suzuki Scholarship for financial support.

I wish to thank the members of the Matsuo's Laboratory for their warm support and encouragement.

Finally, I express my heartfelt thanks to my parents.

Abstract

We have investigated the monolayers and the multilayers of tetramethylsilane (TMS) physically adsorbed on the basal plane of graphite and on the (100) surface of MgO by means of calorimetry, neutron scattering and MD simulation.

For TMS/graphite, an orientational order-disorder phase transition in the 2-D solid is found at 107 K at the coverage $\theta < 1$ and at 138 K at $1 < \theta < 2$. It is accompanied by a large entropy change (ranging from $R \ln 8$ to $R \ln 3$) depending on the coverage. A clear evidence of the orientational order-disorder transition with respect to the reorientation of the TMS molecules is obtained from the incoherent neutron scattering. In the high-temperature phase, the molecules execute fairly excited rotational motion around the axis perpendicular to the surface, and some of the molecules undergo also translational diffusion. Activation energies obtained for molecular motions (reorientation and diffusion) in the monolayer are substantially smaller than those for the bulk α-phase, indicating high mobility in the monolayer. An evidence for such high mobility in diffusional motion in the monolayer is also obtained from MD simulation. The transition temperature and entropy associated with the transition between the 2-D liquid and the 2-D fluid depend on the coverage. This may be related to possible formation of a bilayer fluid. Vibrational properties of the monolayers are deduced from the low-temperature heat capacities. The 2-D Debye temperatures of the monolayers are found to be approximately 60% of the Debye temperature of the bulk γ-phase, reflecting the dimensionality of lattice vibrations.

For TMS/MgO, the monolayer is found to undergo a 2-D solid-solid phase transition around 100 K similar as the one on graphite. However, it is demonstrated that the molecules on the (100) surface of MgO are less mobile than on graphite.

For TMS/graphite at the coverage $\theta > 2$, the bulk phases are formed on top of the solid TMS monolayer adsorbed on graphite at low temperature. The solid monolayer persists at the interface between the bulk liquid and the graphite surface, and it melts around 185 K, well above the melting point of any of the bulk solid phases (165.9 K for the α-phase, 171.0 K for the β-phase, and 174.1 K for the γ-phase). The monolayer undergoes an orientational order-disorder transition at 150 K. However, the ordering appears to be incomplete below 150 K, and the monolayer undergoes a glass transition at low temperature (around 60 K, depending on the coverage) to form an orientational glass. With the increasing coverage, α and β phase, both of which are metastable in the isolated bulk solid, are preferentially formed and stabilized near the graphite surface. Three bulk phases formed in this system coexist at equilibrium. The stabilized α-phase formed in this system is found to undergo a phase transition at 160 K to form an ordered solid at low temperature.

Contents

Chapter 1

Introduction

1.1 Plastic crystals

Orientationally disordered crystals are characterized by small entropy of melting (less than 20 $JK^{-1}mol^{-1}$ according to Timmermans [1]) and existence of a phase transition below which the crystal becomes brittle. The large entropy change at the transition point suggests a considerable motional disorder in the disordered phase. In fact, overall rotation of a molecule is highly excited, and even the self-diffusion is appreciable [2].

1.2 Properties of the bulk tetramethylsilane

Tetramethylsilane (hereafter referred to as TMS) molecule is tetrahedral in shape. TMS belongs to the series of the tetramethyl compounds of the group-IV, $M(CH_3)_4$, where M=C, Si, Ge, Sn, or Pb. Because of their simple molecular structures, the molecular crystals of $M(CH_3)_4$ have been extensively investigated by calorimetric [3–9], spectroscopic [10–12], and NMR [13–18] techniques. Despite of their spherical shape of the molecule, neopentane (M=C) is the only crystal hitherto known to have an order–disorder phase transition [3, 6]; the high-temperature phase is orientationally-disordered with an f.c.c. structure [19]. The larger molecules (M=Ge, Sn, Pb) are known to have no orientationally-disordered phase [5, 7]. Among them, the solid-state properties of TMS are located on the boundary between the properties of neopentane and the last three larger molecules. Namely, TMS forms an orientationally-disordered crystal only as a metastable (α) phase [9,20]. Two other phases (another metastable β and stable γ-phase) are both ordered. The melting points and entropies reported in [9] are summarized in Table 1.1 and the Gibbs energy diagram for TMS is illustrated in Fig. 1.1. The stability of metastable phases appears to be intricate. It has been argued that the stability probably depends on the purity of the sample, the shape of the container and the nature of the inner surface of the container [9].

Table 1.1: Melting points and entropies for three different solid phases of bulk tetramethylsilane [9].

Phase	T_{fus} / K	$\Delta_{\mathrm{fus}}S$ / JK^{-1}mol^{-1}
α	165.920	4.24
β	171.016	34.37
γ	174.074	39.51

1.3 Physisorbed monolayers on solid surfaces

Monolayers of atoms and molecules adsorbed on the (0001) planes of graphite have attracted considerable attention during the last 30 years since the work of Thomy and Duval [21]. Early experiments concentrated on adsorbed rare gas atoms, whose interactions (adsorbate–adsorbate and adsorbate–substrate) are simple and well understood [22–24]. Rare gas atoms tend to form closed-packed structures, which leads to structures with lattice parameters close to $\sqrt{3} \times a_c$ where $a_c = 0.246$ nm is the lattice parameter of the hexagonal graphite substrate. One of the specific phenomena in adsorbed monolayers is a commensurate–incommensurate transition, a transition from the structure commensurate with the underlying potential corrugation to the one incommensurate with the underlying potential. The krypton/graphite system is the most extensively studied example for a commensurate–incommensurate transition [25–29].

Molecules with orientational degrees of freedom show more complicated behavior. Monolayers of simple linear molecules like N_2 or CO show a variety of structures and hence more complicated phase diagrams [30–33]. The monolayers of tetrahedral molecules of methane and its derivatives CX_4 where X=F, Cl, Br, I, shows a large variety of structures with lattice constants in the vicinity of the commensurate $\sqrt{3} \times \sqrt{3}R30°$ structures (see for example the review article by Knorr [34] and references therein). Variety appeared in structures and phase behaviors in adsorbed monolayers is considered to be consequences of the subtle balance of adsorbate–adsorbate and adsorbate–substrate interactions.

As mentioned above, a relatively large number of investigation have been carried out with relatively small molecules adsorbed on graphite, whereas less works has been done on larger molecules. As for the molecular series of $M(CH_3)_4$, few works have been carried out; the monolayers of neopentane [35] (M=C) and tetramethylgermane [36] (M=Ge) on graphite have been found to exhibit an order-disorder phase transition in the 2-D solid, while those for M=Sn and Pb do not show any phase transition [37–39].

The (100) planes of MgO have quite different features from those of the (0001) planes of graphite. The (100) surfaces of MgO offers a square symmetry whereas the graphite do a hexagonal one. The heat of adsorption is considered to be different to each other, for example, 15.6 $kJmol^{-1}$ for Xe on MgO [40] and 20 $kJmol^{-1}$ [41] for Xe on graphite. Also different is the potential surface corrugation, which for MgO (100) is higher (ξ = 0.046 nm [42]) compared to graphite (ξ = 0.021 nm [43]). Since the recent development of preparing MgO (100) sample with high homogeneity [44], several adsorbates have been investigated; rare gases [40, 45], CD_4 [46], NH_3 [47], N_2 [48] and CH_2Cl_2 [49]. Methane/MgO system is one of the most striking example showing the differences in the behavior of the monolayer due to the substrate. The methane molecules form a hexagonal $\sqrt{3} \times \sqrt{3}$ structure with tripod-down orientation on graphite [50], whereas they form a square c(2 × 2) structure with dipod-down orientation on MgO [46]. Furthermore, the methane monolayer on graphite undergoes the commensurate–incommensurate transition below completion of the monolayer [51], whereas the one on MgO undergoes no commensurate–incommensurate transition [46].

Most of the studies on physisorbed monolayers have focused on the phase behaviors and the structures of the monolayers and also on the 2-D melting mechanism, whereas relatively few studies have been done on diffusive motions (rotation and translation) of molecules in the monolayer. We consider that this subject should be studied more extensively, particularly from the point of view of comparison with bulk solids. So far, they have been studied on only few adsorbate/graphite systems by means of incoherent neutron scattering [52–55], NMR [56, 57] and Mössbauer spectroscopy [37].

1.4 Condensed phases at multilayer coverages

Condensed phases at the multilayer coverages adsorbed on graphite have been favored two main subjects. One is the study of formation of multilayers and wetting phenomena, of which the key interest is the propagation of the effects of the surface through successive layers, usually at temperatures below the triple point. Wetting has been extensively studied by many physical techniques [58]. Another is the study of solid monolayers formed at the interface between liquid and the graphite surface. The bulk phase is formed on the monolayer at the interface at the coverage $\theta \sim 10$. The existence of such solid monolayers has been demonstrated for several liquid/graphite systems such as alkanes/graphite [59–65], and carboxylic acid/graphite [59, 66, 67]. These monolayers melt at temperatures approximately 10% higher than the melting points of the bulk solid.

1.5 The purpose of the present study

The purpose of the present study is to investigate the behavior of the condensed phase of TMS formed near the solid surface, including the monolayer as a 2-D condensed phase. We employed heat capacity measurement and incoherent neutron scattering experiment, and also molecular dynamics (MD) simulation. The heat capacity measurement is a powerful technique to detect phase transitions and thus enables us to determine phase diagrams. Since we employ an adiabatic method, we can obtain the absolute values of the heat capacities with high reliability, enabling us to deduce mechanism of the phase transition from entropy estimated. Furthermore, vibrational properties of the monolayer such as lattice vibrations or librations can be deduced from analysis of the low-temperature heat capacity.

Incoherent neutron scattering is one of the most outstanding technique to investigate dynamics directly. Since a TMS molecule involves protons with a large incoherent scattering cross section ($\sigma_{\text{inc}} = 79.90$ barns), we can investigate dynamics of adlayers in spite of the small ratio of the adsorbate to the whole sample in terms of the number of atoms. When the protons in the sample remain their stationary position at low temperature, neutrons scattered by them cause an elastic scattering centered at energy transfer $E = 0$. If the protons vibrate with a certain energy excitation, the scattered neutrons are observed as an inelastic scattering, from which we can obtain intra- and intermolecular vibrational properties of the adlayers. If the protons in the sample are undergoing some random motion, quasielastic scattering events occur outside the elastic window. With increasing temperature, the number of quasielastic scattering events increases accordingly. At a temperature where the correlation time τ of the random motion becomes comparable to the time equivalent to the energy width δE of an instrumental resolution of the spectrometer (i.e., $\tau/\hbar \sim 1/\delta E$), the elastic intensity starts to decrease and quasielastic wings are appeared. Thus, we employed two spectrometers with different instrumental resolution ($\delta E = 200$ μeV and 15 or 5.6 μeV) to investigate molecular motions with different correlation times. Activation energy may be obtained from the temperature dependence of the width of the quasielastic component. Furthermore, the Q-dependence of the intensity ratio of the incoherent elastic scattering to the total incoherent scattering, i.e., elastic incoherent structure factor (EISF), gives us the geometrical information of the rotational motion of the molecules.

MD simulation is also an effective method for the study of the physisorbed layers on solid surfaces since the information available experimentally is limited. We can obtain macroscopic physical properties from an ensemble average of the relevant instantaneous properties obtained at each calculation step in the MD simulation. However, our purpose of employing MD simulation focused on the complementary use to the experiments rather than on the precise reproduction of the macroscopic properties. We calculated some dynamical properties in the present study.

This thesis is organized as follows: Chapter 2 is devoted to the sample and the experimental setup. The results obtained are presented in Chapter 3. Chapter 4 contains analyses of the results and discussion. Conclusion is described in Chapter 5.

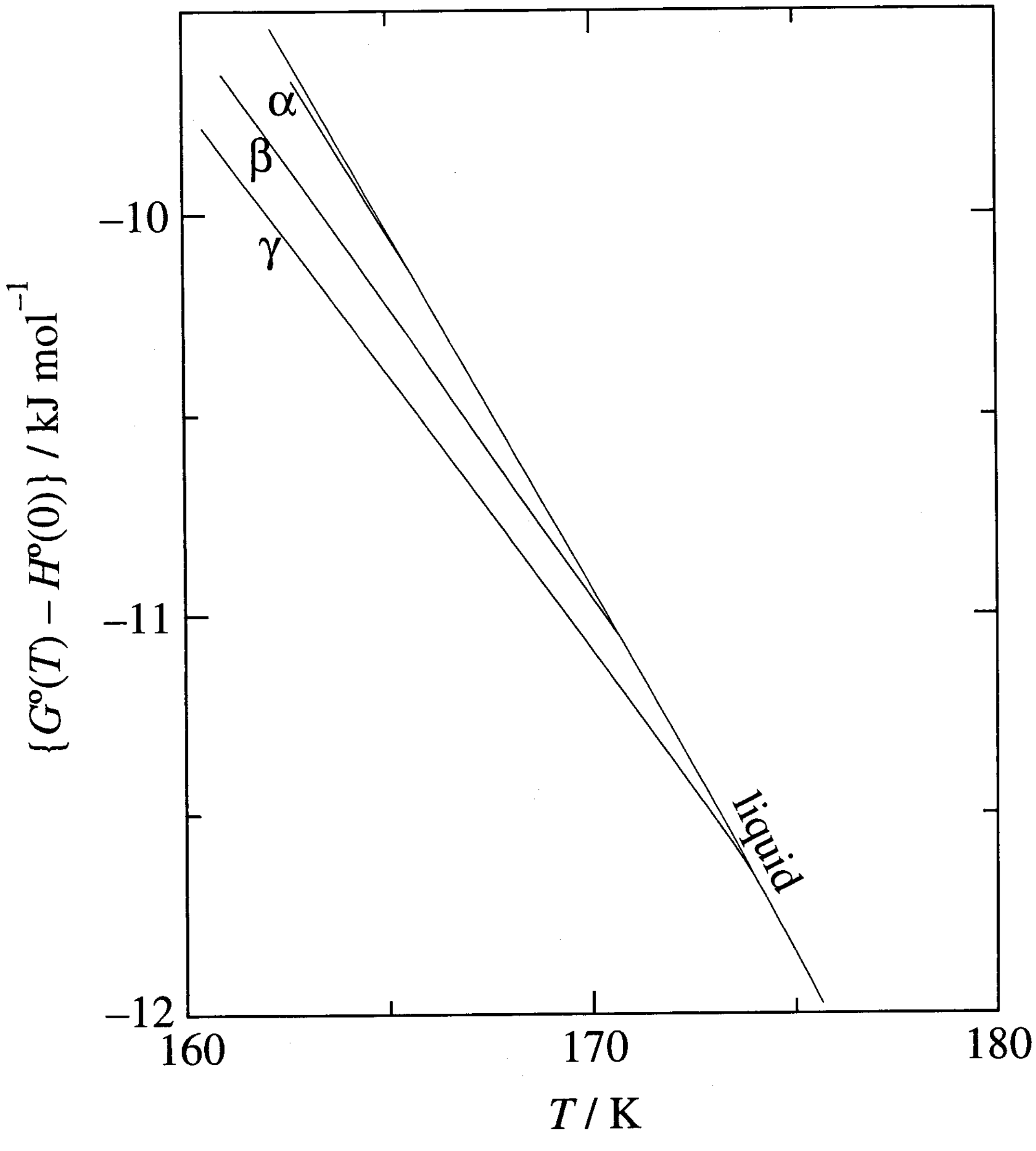

Fig. 1.1: Curves of Gibbs energy against temperature for bulk tetramethylsilane [9].

Chapter 2

Experimental

2.1 Sample

The graphite substrate used was a partially-oriented exfoliated graphite, Papyex (Le Carbone Lorraine). It consists of a mosaic spread in the orientation of the basal planes of about 30° [53]. Since the specific surface area varied with different batches from the supplier, it was determined for each specimen by adsorption isotherm measurements at 77.4 K using nitrogen. The monolayer capacities were determined from BET isotherms. At this temperature the N_2 monolayer forms the orientationally disordered solid with a commensurate $\sqrt{3} \times \sqrt{3}$ structure [30, 31], where one molecule occupies an area of 0.157 nm^2. The specific surface area of four specimens subjected to this study was determined to be 15.6 (A), 16.6 (B), 8.81 (C) and 15.3 (D) m^2g^{-1}, respectively. The designations of A–D will be used in the following chapter. The sample Papyex was outgassed under vacuum at 400 °C before use.

The MgO substrate was prepared by us according to the procedure reported before [44]. Briefly, Mg ribbons (minimum assay 99.9 %, The Nilaco Corporation) were burned in an atmosphere of a mixture of argon (80 %) and oxygen (20 %) (Sumitomo Seika Chemicals). Floating particles in the smoke were collected and immediately degassed under vacuum at 950 °C for 12 ~ 14 hours. 23 g of MgO was obtained from 200 g of magnesium ribbon. The sample was prepared in two batches separately. Here, we designate them as E (13.40 g of MgO obtained from 100 g of Mg) and F (9.60 g from 100 g of Mg) in this thesis. The characterization by SEM demonstrated that the cube-like particles with (100) surfaces were typical with a side of approximately 0.2 μm. The powder was shaped into pellets to have better thermal contact in the experimental vessel. The radius of the pellet was 13 mm for neutron scattering experiments or 20 mm for heat capacity and isotherm measurements. The pellets were outgassed immediately before use. The specific surface areas of these specimens were determined to be 10.7 m^2g^{-1} (E) and 11.7 m^2g^{-1} (F), respectively.

NMR standard grade of TMS (minimum assay 99.5 %, Wako Pure Chemical Industries) was dried over Molecular Sieve 4A and purified further by fractional distillation-condensation cycles. Quantities of the adsorbates introduced into the experimental vessels were determined volumetrically.

2.2 Coverage

Although we do not know the 2-D structure for TMS on graphite, all coverages referred in this study are given in units of MLs on the assumption of the commensurate $\sqrt{7}\times\sqrt{7}R19^\circ$ structure, where each molecule occupies an area of 0.367 nm^2 on the surface (the lattice constant 0.651 nm). This measure has been assumed because tetramethylgermane actually forms this structure [36]. For TMS/MgO, the coverages are also given on the same basis as for TMS/graphite.

2.3 Calorimetry

The adiabatic calorimeter used was essentially the same as described before [33]. The calorimeter vessel used was made of copper, equipped with a needle valve through which known quantities of the adsorbate were added from the vapor. No helium gas was introduced. A platinum resistance thermometer (MINCO Products, Inc.) was used above 14 K. Below 15 K, a germanium resistance thermometer was used, either the one supplied by Scientific Instr., Inc. (for TMS/graphite) or the one by Lake Shore Cryotronics, Inc. (for TMS/MgO). The resistance of the platinum thermometer was measured by an a. c. resistance bridge (model 5840D, H. Tinsley & Co., Ltd.), while that of the germanium thermometer was measured by a digital multimeter (model 195A, KEITHLEY Inst., Inc.). The temperature scale is based on ITS-90 [68]. The heat capacity of the adsorbed layers was determined as the difference between that of the calorimeter, adsorbent and adsorbate, and that of the calorimeter and adsorbent only. Heat capacity measurements were made in the temperature range between 4 and 260 K for TMS/graphite and between 4 and 200 K for TMS/MgO.

2.4 Neutron scattering

Incoherent neutron scattering experiments were performed with three spectrometers of an inverted-geometry time-of-flight type, installed at KEK, Japan. Pulsed neutrons with a wide energy distribution emitted from either a thermal moderator (H_2O at room temperature) or a cold moderator (solid CH_4 at 20 K) are incident on the sample after flying through the first flight path. The scattered neutrons with a fixed energy are selected with analyzer mirrors and detected with neutron counters. The high resolution was achieved on LAM–80ET by using an array of Mica analyzers in backscattering geometry [69]. The medium resolution was achieved on LAM–40 by using an array of pyrolytic graphite (PG) analyzers [70]. These two spectrometers receive cold neutrons. They were employed to investigate quasielastic scattering due to diffusive motions (translation and rotation) of molecules. The LAM–D spectrometer with analyzer mirrors of PG receives thermal neutrons to cover a wide range of energy (up to 300 meV) [71]. It was employed for molecular spectroscopy. Characteristic parameters for each spectrometer are summarized in Table 2.1.

Table 2.1: Characteristic parameters of the three spectrometers employed for neutron scattering. E_k, ΔE, 2θ and Q stand for the analyzing energy, the energy resolution at the elastic position, the scattering angles and the momentum transfer at the elastic position, respectively.

	LAM–80ET		LAM–40	LAM–D
Analyzer	mica(004)	mica(006)	PG(002)	PG(002)
Number of bank	8		7	4
E_k / meV	0.847	1.91	4.59	4.59
ΔE / μeV	5.6	15	200	400
2θ / degree	15–118		24–120	35, 85
Q / nm^{-1}	1.7–11.0	2.5–16.5	6.2–25.8	9.0, 20.0

We used a cylindrical can made of aluminum with a diameter of 15 mm, equipped with a needle valve similar to the one for the calorimeter vessel. The temperature was controlled within 0.2 K.

Multiple scattering should be considered when one performs any neutron scattering experiments. However, the effect can be neglected when the transmission is greater than 90%. Table 2.2 shows the transmission of neutrons and the ratios of either the scattered or absorbed neutrons by our samples, to the incident neutrons calculated from the scattering cross sections. Table 2.2 shows that the ideal transmission has not been achieved in our experiments due to large contribution from coherent scattering of the substrate. This is unavoidable for the experiments of adsorbed systems. Although TMS contains a large number of protons, the ratio of incoherent scattering from the adsorbate to the scattering from the substrate is considerably small, indicating that longer-measurement time is needed to obtain better spectral quality of the adsorbate.

2.5 Molecular dynamics simulation

We used a software MASPHYC–SP (Fujitsu Ltd.) to generate the constant-NVT ensemble. The constant-T was achieved by the method proposed by Nosé [72]. In this method, the physical system of interest consists of N particles, to which an extra degree of freedom s is added. s acts as external system and the interaction between the physical system and s is expressed via the scaling of the velocity of the particles. This can be interpreted as an exchange of heat between the physical system and the external system. A special choice of the potential energy for the variable s and its conjugated momentum makes the system equivalent to the canonical ensemble. The conserved quantities in this extended system are the hamiltonian, the total momentum and the total angular momentum.

We performed the integration of the equations of motion with a Gear predictor-corrector scheme of fifth order [73]. At first, molecular positions $\mathbf{r}_i$ at time $t+\Delta t$ are predicted using a fifth-order Taylor series based on positions and their derivatives at time t. Next, the intermolecular force $\mathbf{F}_i$ on each molecule is evaluated at time $t + \Delta t$ using the predicted positions. Finally the predicted positions and their derivatives are corrected using the discrepancy between the predicted acceleration and that given by the evaluated force $\mathbf{F}_i$. This method gives us high-accuracy solution of the integration but needs a rather small integration time step than other methods such as the Verlet algorithm [74]. Since the scheme is not perfectly time reversible, there will be some drift in the total energy of the system.

The simulation box applied for the monolayer is 10.1 × 10.2 nm^2 in size which is comparable to the coherence length of Papyex used in our experiments. For the multilayer, we took a smaller size, 8.1 × 8.1 nm^2, to save the computing time. A 2-D periodic boundary condition was applied in the X-Y plane. DREIDING force field [75] was used for the potential functions. However, for the parameters of the non-bonding interaction of Si, we adopted the parameters used in DREIDING/A [75] instead of the original ones in DREIDING. Generally a cutoff distance is chosen to be 2.5σ, where σ is the van der Waals bond length used for the Lennard Jones potential. We used a cutoff distance of 1.3 nm which is longer than 2.5σ. At this distance, the intermolecular potential is 0.3% of the potential minimum.

Table 2.2: The transmission of neutrons and the ratios of either the scattered or absorbed neutrons by our samples to the incident neutrons.

System	Transmission (%)	Ratio (%)		
		coherent	incoherent	absorption
<TMS/graphite>	64			
graphite (26.67 g)		31	0	0.02
TMS(1.958 mmol)		0.2	4.7	0.01
<TMS/MgO>	69			
MgO (12.49 g)		26	0.26	0.21
TMS(0.400 mmol)		0.19	4.1	0.00092

Chapter 3

Results

3.1 TMS/graphite at the coverage $\theta < 2$

3.1.1 Heat capacity

Heat capacity measurements were performed for the monolayers at seven different coverages θ ranging from 0.337 to 1.81. The amounts of adsorbent and adsorbate for each sample are summarized in Table 3.1. The contribution of the heat capacity from the adsorbate at $\theta = 0.337$, for example, was 1% of the total heat capacity below 15 K, 0.3% at 40 K, and 0.1% at higher temperatures except at the transition temperatures. The overall inaccuracy of the measurements

Table 3.1: Amounts of adsorbent and adsorbate for each sample at $\theta < 2$.

Coverage	Papyex / g	TMS / mmol
0.337	9.164 (B)	0.232
0.609	10.57 (A)	0.454
0.756	11.42 (C)	0.344
1.05	11.42 (C)	0.480
1.21	11.42 (C)	0.552
1.44	11.43 (C)	0.656
1.81	11.43 (C)	0.826

was estimated to be $\approx 5\%$ or better over the whole temperature range. For the measurements at higher coverages, the accuracy was improved accordingly.

Fig. 3.1 illustrates the molar heat capacities obtained for TMS on graphite at selected coverages $\theta = 0.337, 1.44$ and 1.81. They clearly indicated three anomalies; a prominent anomaly at the transition point of 107 K at $\theta < 1$ or at 138 K at $1 < \theta < 2$, an anomaly at the melting point of 149 K at $\theta < 1$ or around 155 K at $1 < \theta < 2$, and an additional broad anomaly around 200 K due to the transition between the 2-D liquid and the 2-D fluid. The phase transition in the 2-D solid is quite sharp so that one can describe it as a first-order transition. For other two anomalies, the shape depends on the coverage.

The entropies associated with the transition, the melting and the transition between the 2-D liquid and the 2-D fluid are summarized in Table 3.2, indicating that the 2-D solid-phase transitions are accompanied by a large entropy change depending on the coverage.

Table 3.2: Entropy changes associated with the transition, the melting and the transition between the 2-D liquid and the 2-D fluid for TMS on graphite at $\theta < 2$. Note that "200 K" stands for the transition between the 2-D liquid and the 2-D fluid. For the sample at $\theta = 0.609$, measurements were made only below 190 K.

	ΔS / JK^{-1}mol^{-1}		
Coverage	Transition	Melting	200 K
0.337	15	3.6	6.9
0.607	16	6.0	–
0.756	16	4.8	7.6
1.05	13	0.7	5.8
1.21	11	4.4	~5.0
1.44	12	8.4	2.1
1.81	8.9	11	0.5

Fig. 3.2 illustrates the low-temperature heat capacity for the monolayers at $\theta = 0.609$ and 1.81. The one reported for the bulk γ-phase [9] is also plotted for comparison. It is evident that the molar heat capacity of the monolayers is substantially larger than that of the bulk solid.

3.1.2 Neutron scattering

The TMS monolayer at $\theta = 1.04$ was investigated by high-resolution LAM–80ET spectrometer. The amount of TMS was 1.958 mmol for 26.67 g of graphite (A). Fig. 3.3 and Fig. 3.4 illustrate some of the spectra at the selected momentum vectors $Q = 8.1$ and 12.1 nm^{-1}, respectively. These spectra indicated that quasielastic broadening appeared above the transition temperature (107 K), which was more prominent at higher Q. The quasielastic scattering component was still visible even in the 2-D liquid phase and the width did not change dramatically across the melting. While the elastic scattering intensity decreased substantially across the transition point, the remaining contribution died out completely at the melting point.

Fig. 3.5 illustrates some of the spectra obtained on the medium-resolution LAM–40 spectrometer, at the momentum vector $Q = 14.0$ nm^{-1}. The sample investigated was the TMS monolayer at $\theta = 1.02$. The amount of TMS was 1.942 mmol for 26.86 g of graphite (A). Another quasielastic scattering component appeared above the transition point, which was broader than that observed on LAM–80ET. It was still visible in the 2-D liquid phase and the width did not change dramatically across the melting.

Fig. 3.6 illustrates the inelastic neutron scattering spectra obtained on LAM–D for TMS/-graphite at $\theta = 1.02$ (1.906 mmol of TMS and 26.36 g of graphite (A)) at $T = 16$ K. Lattice vibrational modes appeared in the low-energy region below 12 meV. Some of the intramolecular vibrational modes appeared in the higher energy region.

The TMS monolayers at 1.5ML were also investigated by neutron scattering. Fig. 3.7–Fig. 3.9 illustrates some of the spectra obtained on LAM–80ET, at selected Q. The sample investigated was the monolayer at $\theta = 1.55$. The amount of TMS was 2.914 mmol for 26.69 g of graphite (A). The spectra obtained at the scattering angle 52° on LAM–80ET (corresponding $Q = 8.4$ nm^{-1} for mica (006) or $Q = 5.6$nm^{-1} for mica (004)) were noisy presumably due to the cryostat used for the experiments. Quasielastic broadening was also observed above the transition point at this coverage, which appeared to be slightly narrower than that observed at $\theta = 1.04$. Fig. 3.7 shows that an elastic-like component still appears in the spectra at $T = 160$ and 170 K, above the melting point (around 155 K). We consider that they are probably attributed to either an experimental error or an incomplete subtraction of the background contribution, or more likely to both of them, for the following reasons: (i) the spectra at $Q = 8.1$ nm^{-1} were obtained with the mica (004) mode on LAM–80ET, yielding an experimental error of about $\sqrt{3}$ times larger than that of the spectra obtained with the mica (006) mode according to the intensity–wavelength character of the pulsed cold-neutron source at KEK, and (ii) the measurement time for the empty cell (containing the graphite substrate only) was about one-third of the measurements of the sample cell (containing both TMS and graphite), also yielding an experimental error of about $\sqrt{3}$ times larger. For the spectra obtained with the (006) mode, the accuracy was estimated to be $\approx 6\%$ for the measurements of 1.5ML of TMS. Thus the spectra obtained with the (004) mode resulted in containing large inaccuracy. In fact, the elastic component died out for 1.5ML of TMS at the same temperatures at the slightly higher Q obtained with the instrumental resolution $\Delta E = 15$ μeV (Fig. 3.9), showing that the molecular motions of such a longer correlation time ($\tau > 8.8 \times 10^{-11}$) would no longer exist at this temperature.

Fig. 3.10 illustrates some of the spectra obtained on the LAM–40 at $Q = 14.0$ nm^{-1} for the monolayer at $\theta = 1.54$. The amount of TMS was 2.914 mmol for 26.86 g of graphite (A). Also observed was quasielastic broadening with a broader component above the transition point ($T = 138$ K).

3.1.3 MD simulation

Two surface coverages were explored by MD simulation, $\theta = 0.724$ and 1.40. Fig. 3.11 illustrates the initial configuration in the simulation at $\theta = 0.724$. The simulation system contained either 203 or 392 of TMS molecules. Initially they were placed in a hexagonal arrangement with a lattice constant of 0.7 nm, which is significantly larger than that of the $\sqrt{7} \times \sqrt{7}R19^\circ$ structure (0.651 nm). At $\theta = 1.40$, the molecules were placed to form a bilayer, where the distance between the first and second layer was 1.0 nm. Each of TMS molecule was placed on the surface of graphite with dipod-down orientation. None of the atoms were united for the TMS molecules and all the bond length and bond angles were allowed to vary.

For simulation of monolayer/graphite system, the potential function proposed by Steele [77] is widely used to represent the adsorbate–adsorbent interactions. However, we took the graphite substrate into the calculation as a normal object in the sense that they consisted of individual atoms, from the point of view that dynamics of graphite should be took into account. Each of graphite sheet consisted of 3936 carbons with a bond length of 0.1418 nm in practice. They were placed in every 0.3348 nm. Since the cutoff distance was 1.3 nm, we considered that three graphite sheets were sufficient for our simulation system. The carbon atoms of only the lowest layer were fixed in the position to fix the center of mass of the simulation box. This can be considered as the representation of *bulk* state in graphite substrate.

Two temperatures were simulated at each coverage, 40 K and 140 K at θ = 0.724 and 120 K and 150 K at θ = 1.40. At both coverages, as discussed later, the monolayers form an ordered solid at the lower temperature, and they do an orientationally disordered one at the higher temperature. The simulating time ranged from 250 ps (at θ = 0.724 at 40 K) to 1 ns (at θ = 0.724 at 140 K). The simulation conditions are summarized in Table 3.3.

Table 3.3: Simulation conditions for the TMS monolayers on graphite. Note that N_m, N_a, T and t stand for the number of TMS molecules, the total number of atoms in the simulation system, the simulating temperature and the total simulating time, respectively.

θ	N_m	Surface area (nm^2)	N_a	Ensemble	T / K	t/ ps
0.724	203	10.2096 × 10.0698	15259	*NVT*	40	250
0.724	203	10.2096 × 10.0698	15259	*NVT*	140	1000
1.40	392	10.2096 × 10.0698	18472	*NVT*	120	600
1.40	392	10.2096 × 10.0698	18472	*NVT*	150	340

Fig. 3.12 illustrates the time evolution of the instantaneous temperature of the system, the internal energy and the hamiltonian obtained at θ = 0.724 at the simulating temperature 40 K. The instantaneous temperature of the system was calculated by averaging over the kinetic energies of all the particles in the simulation box. The energy drift of the hamiltonian was 0.09%/ps. Also illustrated in Fig. 3.12 (b) is the instantaneous temperature of the admolecules only, calculated from their center-of-mass velocities, which demonstrates that there has been a discrepancy between the system temperature and the monolayer temperature. We consider that this might be caused by the timestep size used in this study (Δt = 0.5 fs) being too long to handle properly the highest frequency mode in the molecule, i.e., C–H stretching. In fact, to be shown in later section, for the simulations of multilayers where the unified molecules were used, i.e., there was no explicit C–H bond, the adlayer temperature converged to the simulating temperature at equilibrium with Δt = 0.5 fs even at higher temperature. Thus, the energy drift of 0.09%/ps in the hamiltonian was supposed to be unnegligible from the point of view of precise reproduction of the system being studied. Nevertheless, almost all the properties to which we pay

attention can be calculated from either the coordinates or the velocities of the center-of-mass of the molecule, or at least the central 5 atoms (Si and four C). Although the monolayer did not reach equilibrium completely, the temperature of the admolecules was not far from the simulating temperature. Thus we consider that static properties and dynamical properties with a correlation time of short-range order such as lattice vibrations can be calculated from the data obtained over the last 50 ps.

Fig. 3.13 illustrates the time evolution of physical quantities obtained at $\theta = 0.724$ at the simulating temperature 140 K. Although there was the discrepancy between the system temperature and the monolayer temperature, the monolayer reached equilibrium at about 130 K after c. a. 300 ps.

A snapshot is illustrated in Fig. 3.14 and Fig. 3.15 to show the molecular configuration of TMS, at different temperatures 40 K and 140 K, respectively. These were obtained after 250 ps of the simulation at 40 K and after 500 ps at 140 K. They demonstrate that the molecules form an ordered solid at 40 K, where the molecules sit on the surface of graphite with the dipod-down orientation, and the molecules form an orientationally disordered one at 140 K with an almost hexagonal arrangement.

Fig. 3.16 and Fig. 3.17 illustrate the time evolution of the physical quantities obtained at $\theta = 1.40$ at the simulating temperature 120 and 150 K. The discrepancy between the system temperature and the monolayer temperature was slightly larger than that at $\theta = 0.724$, which can be understood by considering the larger number of C-H bonds than that at $\theta = 0.724$. From the time evolution of the monolayer temperature, one could say that the monolayers have reached equilibrium roughly after 400 ps at 120 K and 250 ps at 150 K. At this coverage, TMS molecules formed a bilayer except only few molecules in the third layer, which is illustrated in Fig. 3.18. The molecules sit on the surface of graphite with the dipod-down orientation, which is not explicitly illustrated in the figure.

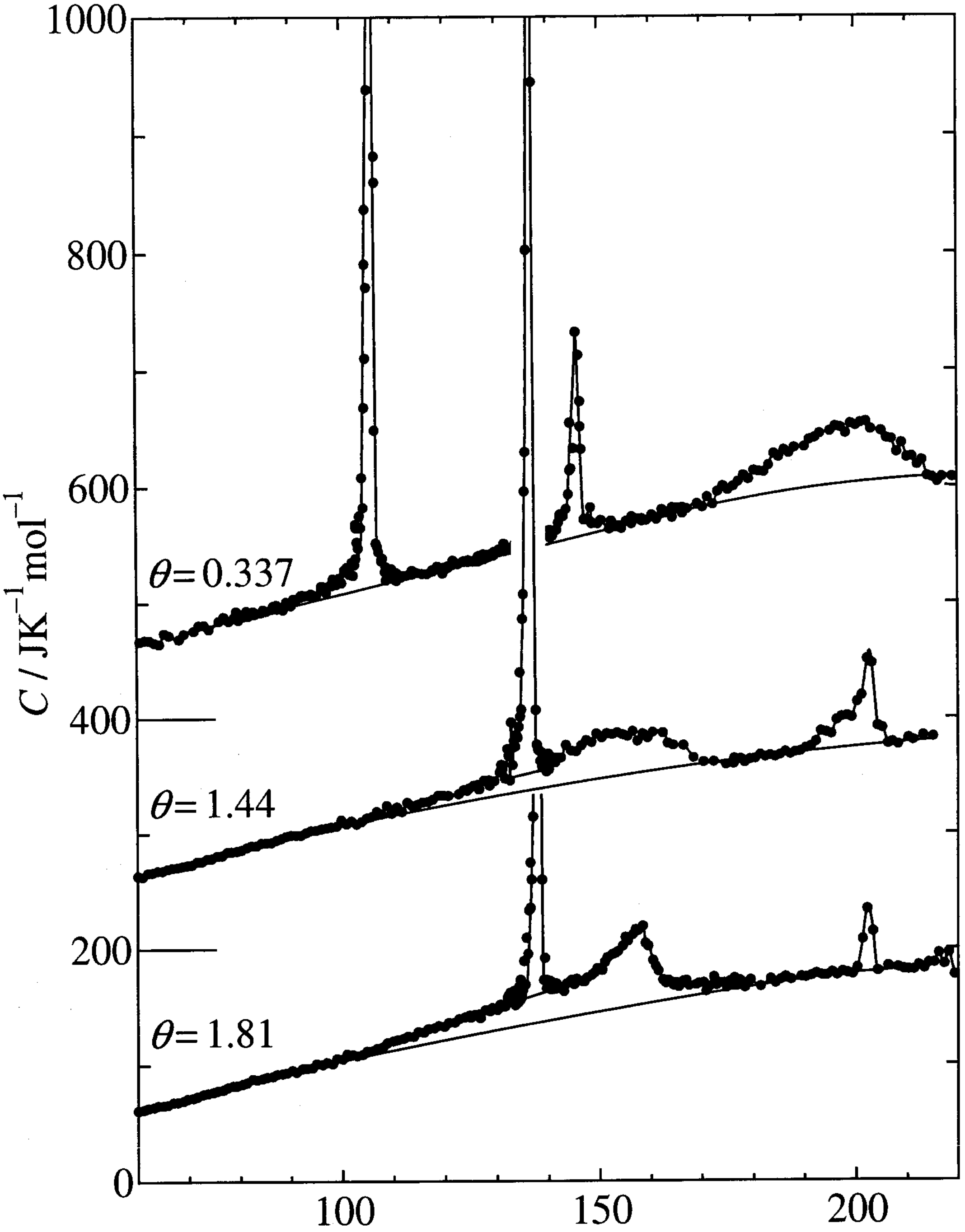

Fig. 3.1: Molar heat capacities of TMS on graphite determined at coverage θ = 0.337, 1.44 and 1.81. The estimated baselines are also indicated. Note that vertical scale of each curve is shifted from the next by 200 JK^{-1}mol^{-1}

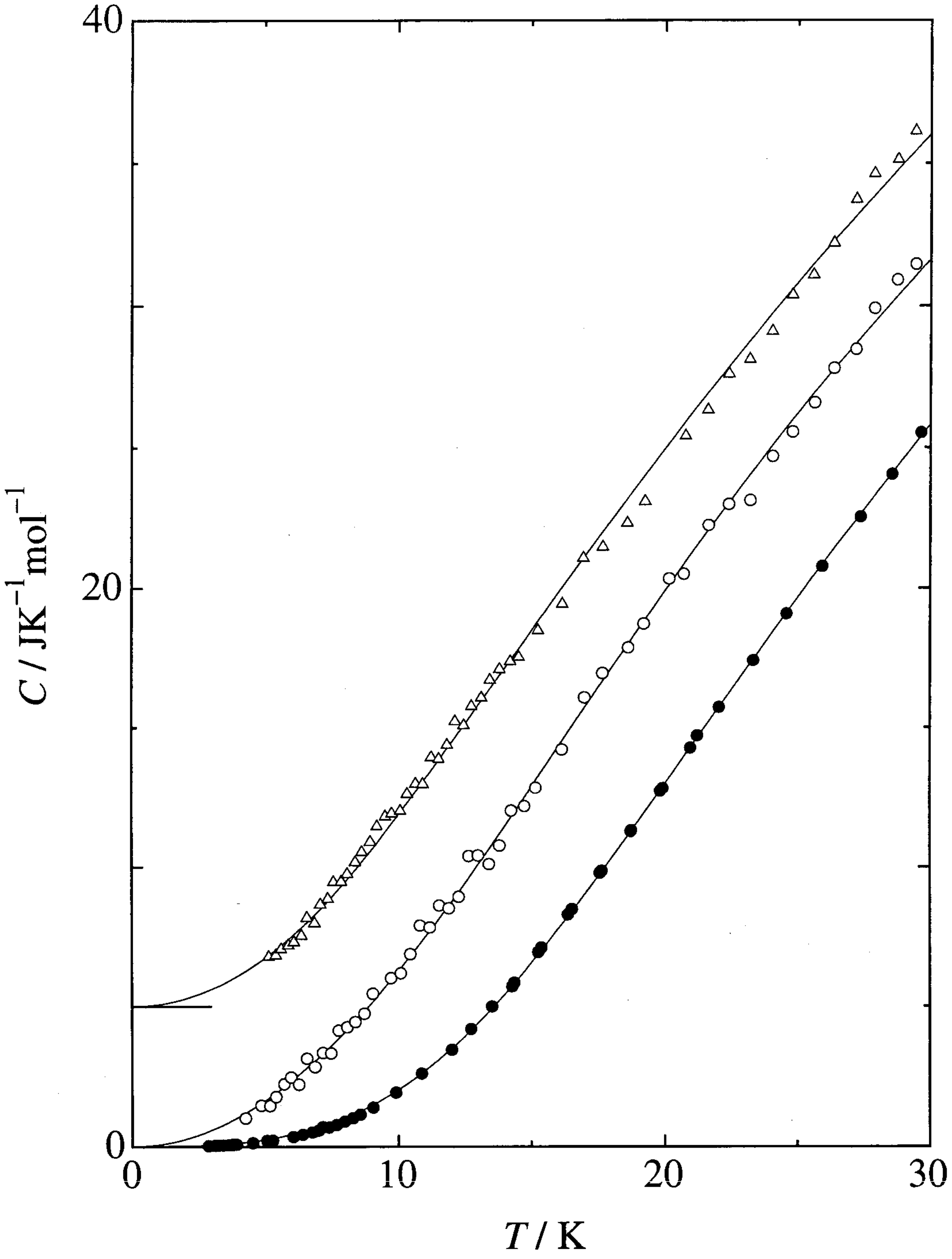

Fig. 3.2: Low-temperature heat capacity of TMS on graphite at θ = 0.609 (open circles) and 1.81 (triangles). The one reported for the bulk γ-phase [9] is also plotted (filled circles) for comparison. Note that the vertical scale for the monolayer at θ = 1.81 is shifted from the next by 5 JK^{-1}mol^{-1}

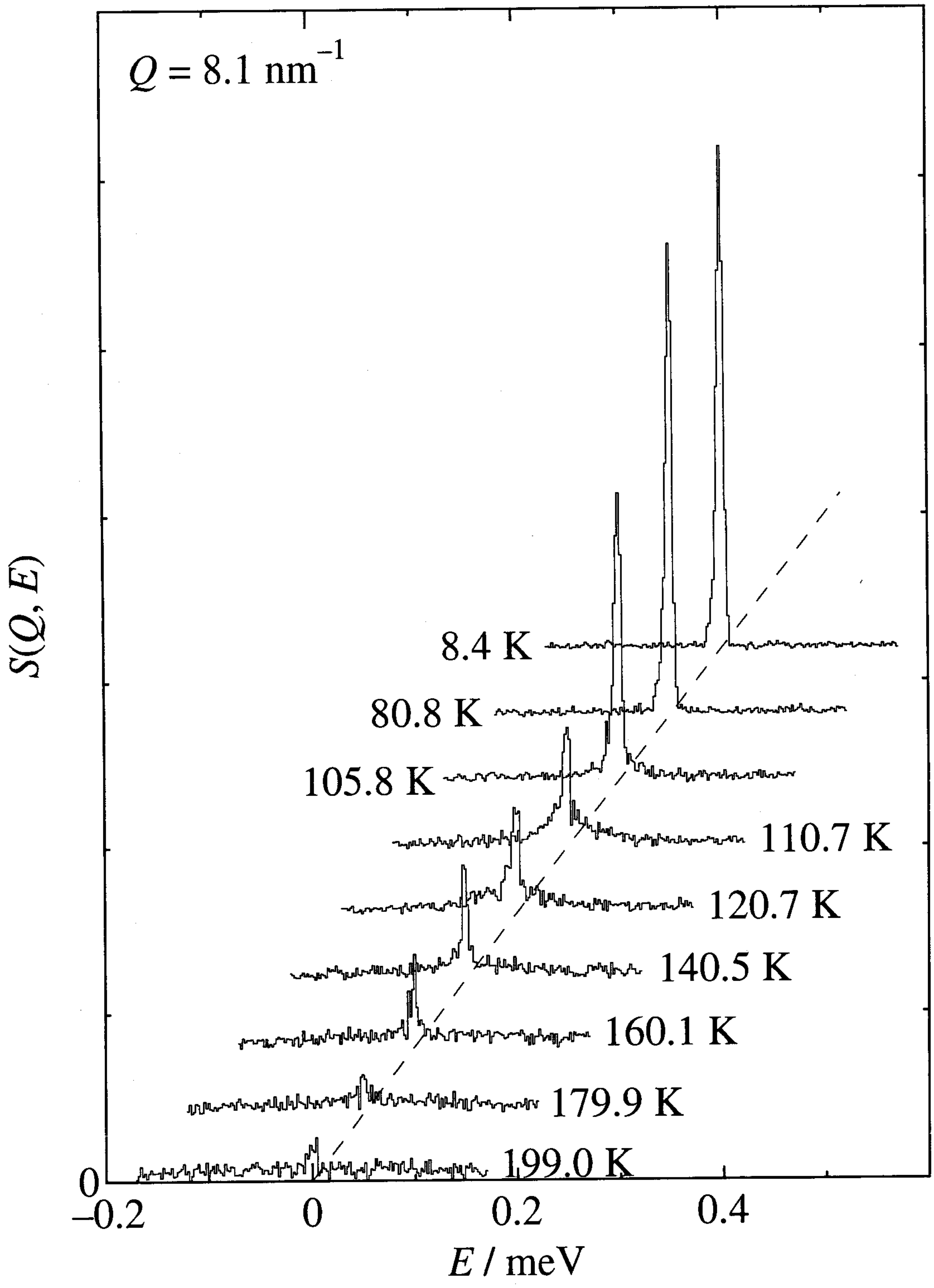

Fig. 3.3: Neutron scattering spectra obtained on LAM–80ET for TMS/graphite at $\theta = 1.04$ at $Q = 8.1\ \mathrm{nm}^{-1}$ with an instrumental resolution $\Delta E = 5.6\ \mu\mathrm{eV}$. The background contribution has already been subtracted.

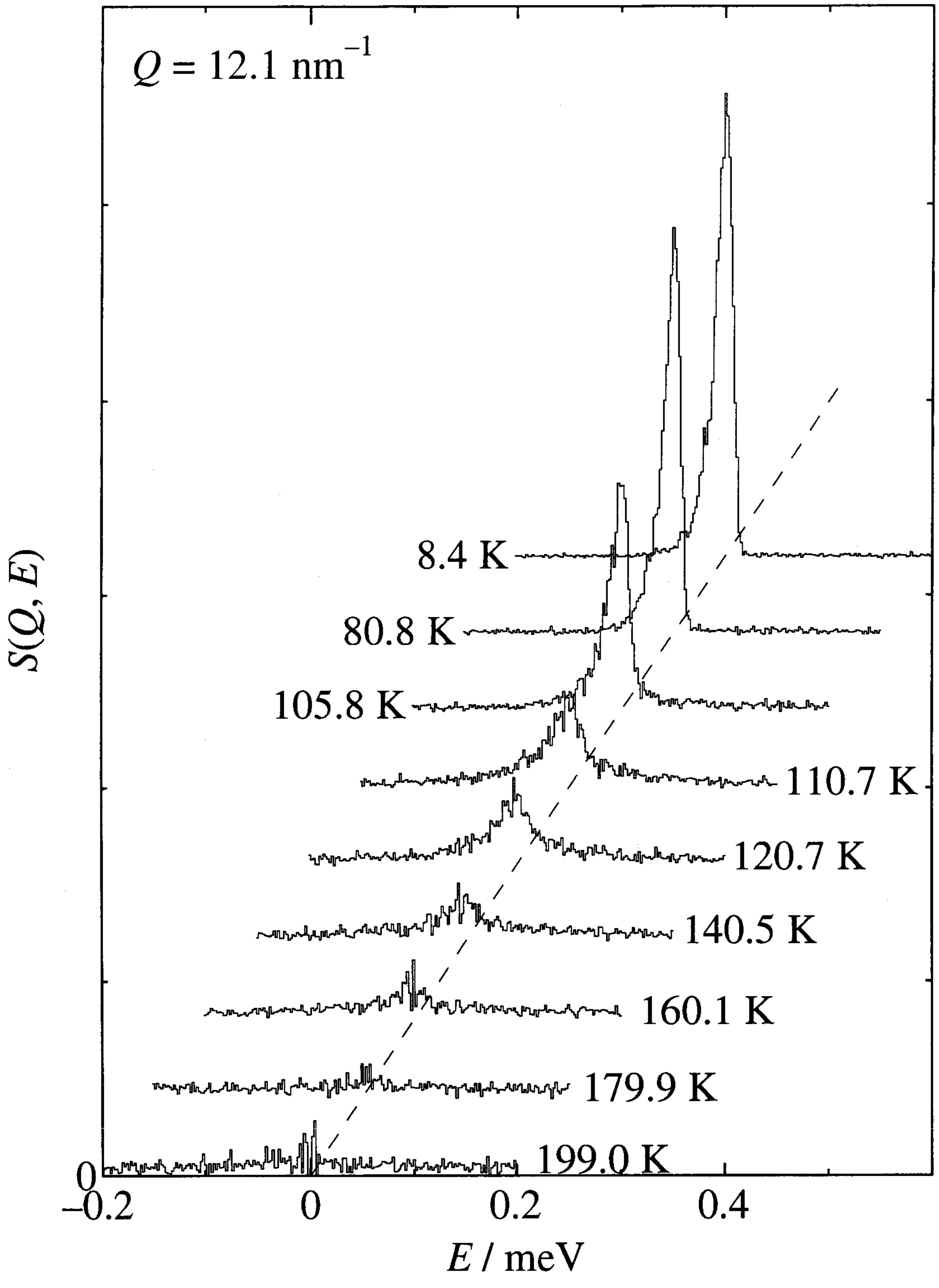

Fig. 3.4: Neutron scattering spectra obtained on LAM–80ET for TMS/graphite at $\theta = 1.04$ at $Q = 12.1\ \mathrm{nm}^{-1}$ with an instrumental resolution $\Delta E = 15\ \mu\mathrm{eV}$. The background contribution has already been subtracted.

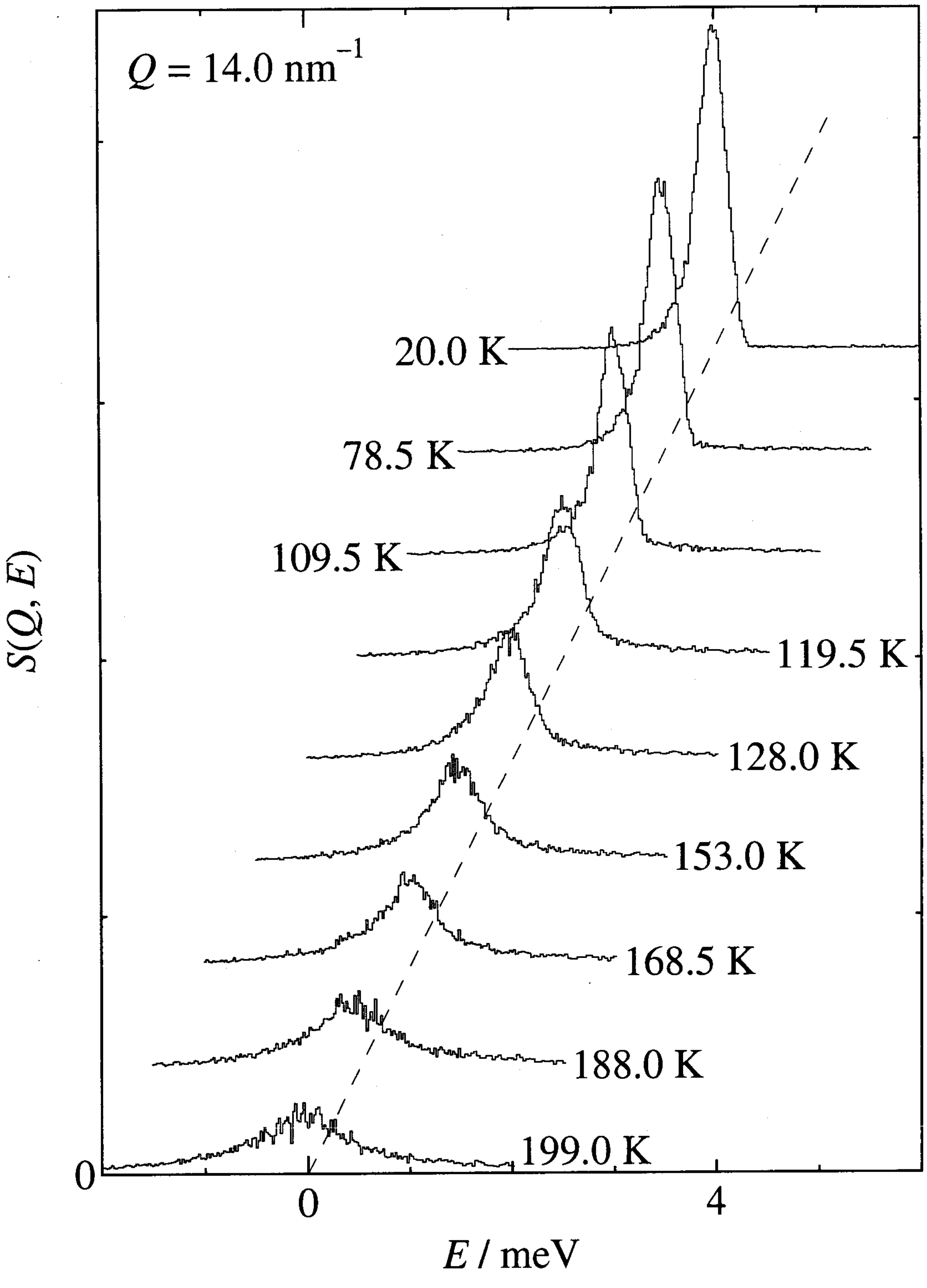

Fig. 3.5: Neutron scattering spectra obtained on LAM–40 for TMS/graphite at $\theta = 1.02$ at $Q = 14.0\ \mathrm{nm}^{-1}$ with an instrumental resolution $\Delta E = 200\ \mu\mathrm{eV}$. The background contribution has already been subtracted.

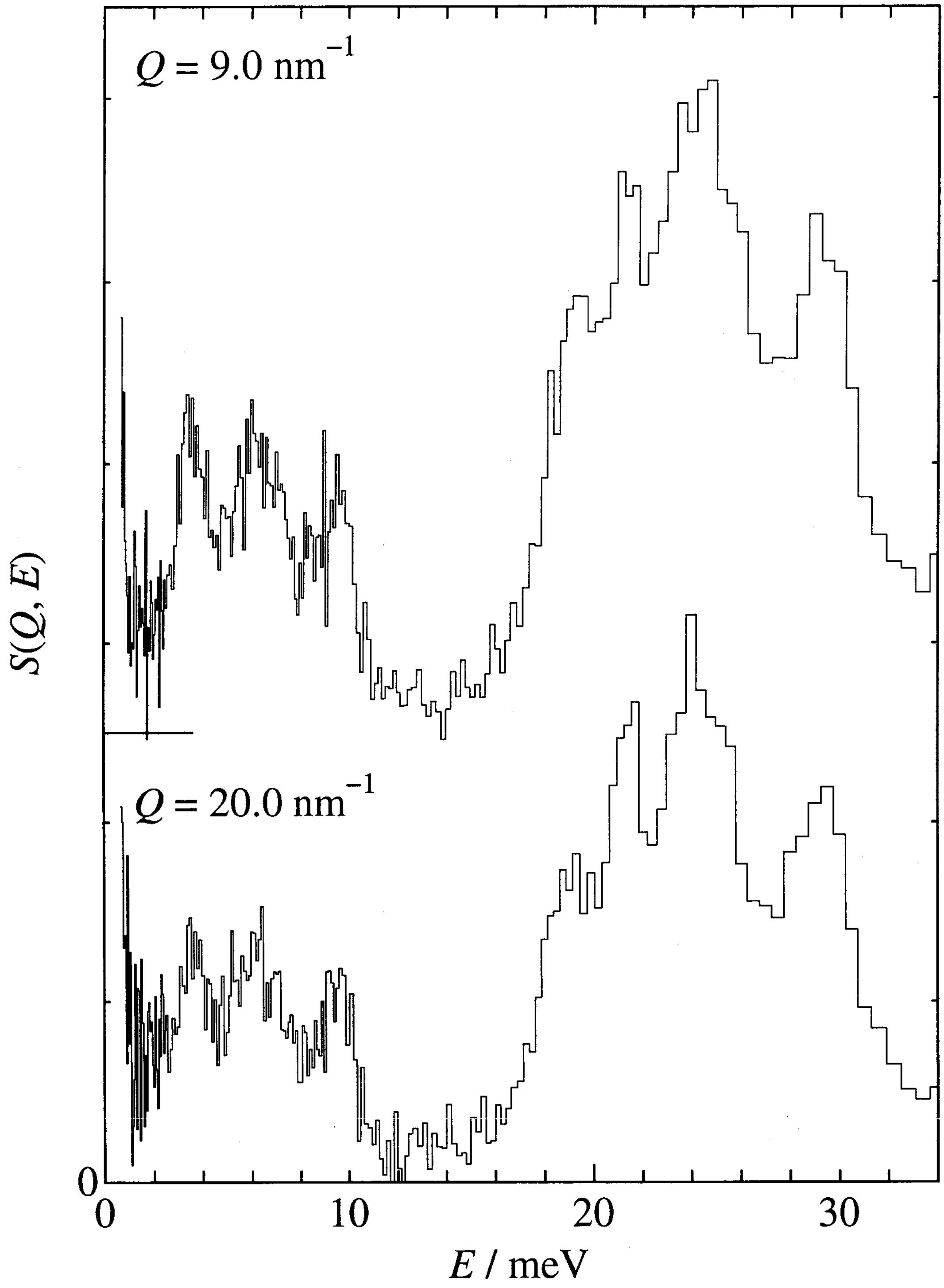

Fig. 3.6: Neutron scattering spectra obtained on LAM–D for TMS/graphite at $\theta = 1.02$ at $T = 16$ K. The background contribution has already been subtracted.

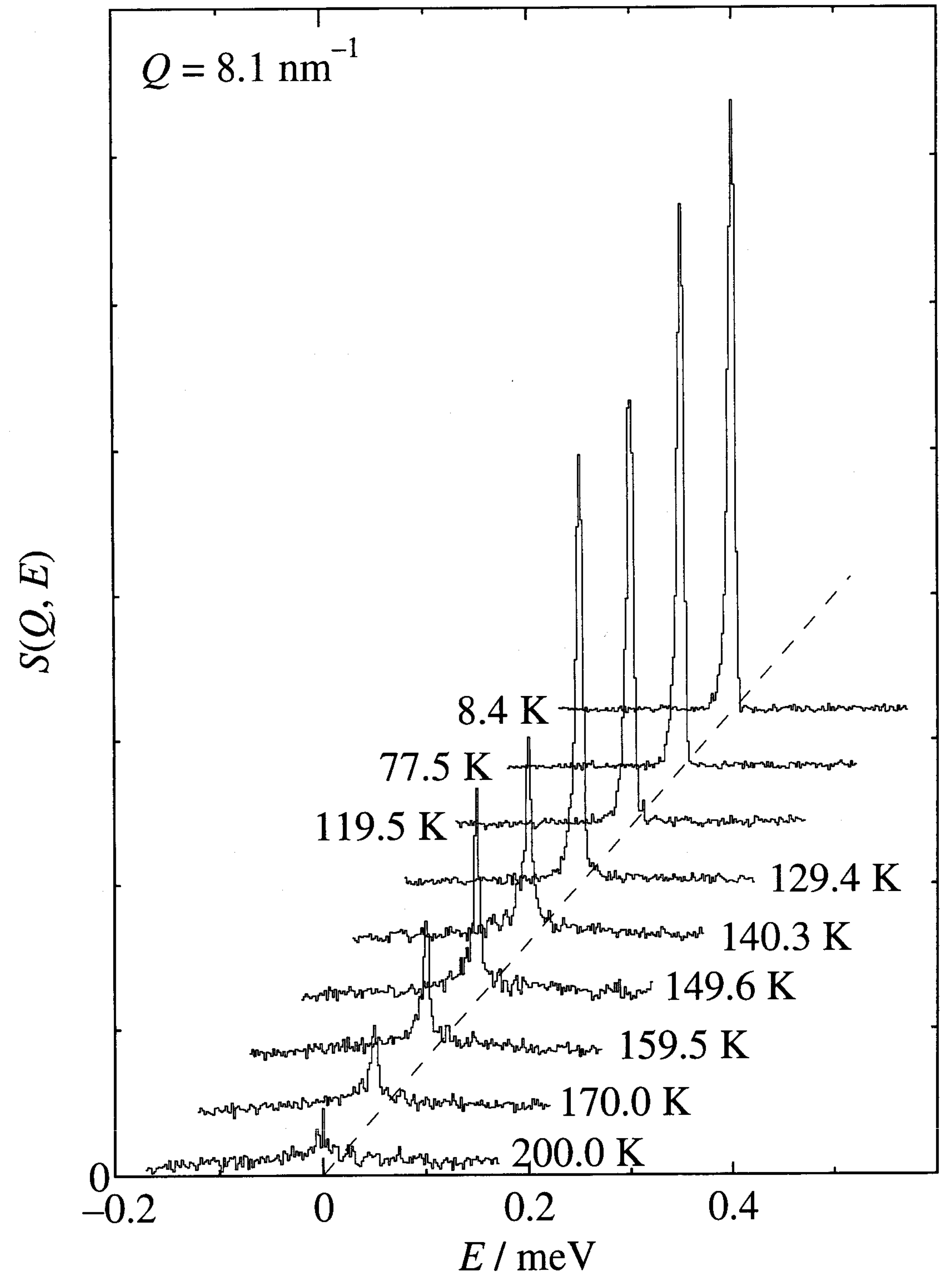

Fig. 3.7: Neutron scattering spectra obtained on LAM–80ET for TMS/graphite at $\theta = 1.55$ at $Q = 8.1\ \mathrm{nm}^{-1}$ with an instrumental resolution $\Delta E = 5.6\ \mu\mathrm{eV}$. The background contribution has already been subtracted.

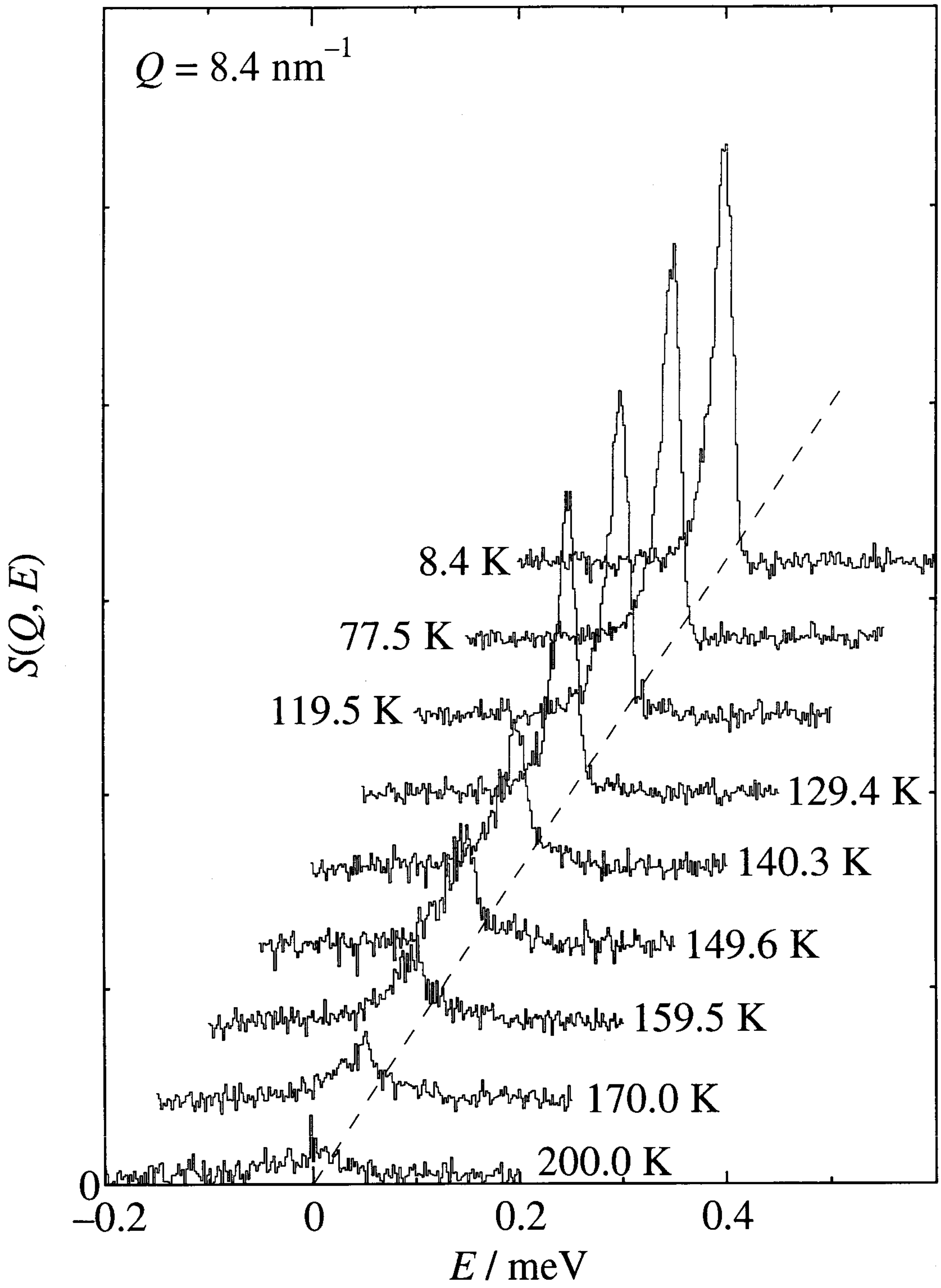

Fig. 3.8: Neutron scattering spectra obtained on LAM–80ET for TMS/graphite at $\theta = 1.55$ at $Q = 8.4\ \mathrm{nm}^{-1}$ with an instrumental resolution $\Delta E = 15\ \mu\mathrm{eV}$. The background contribution has already been subtracted.

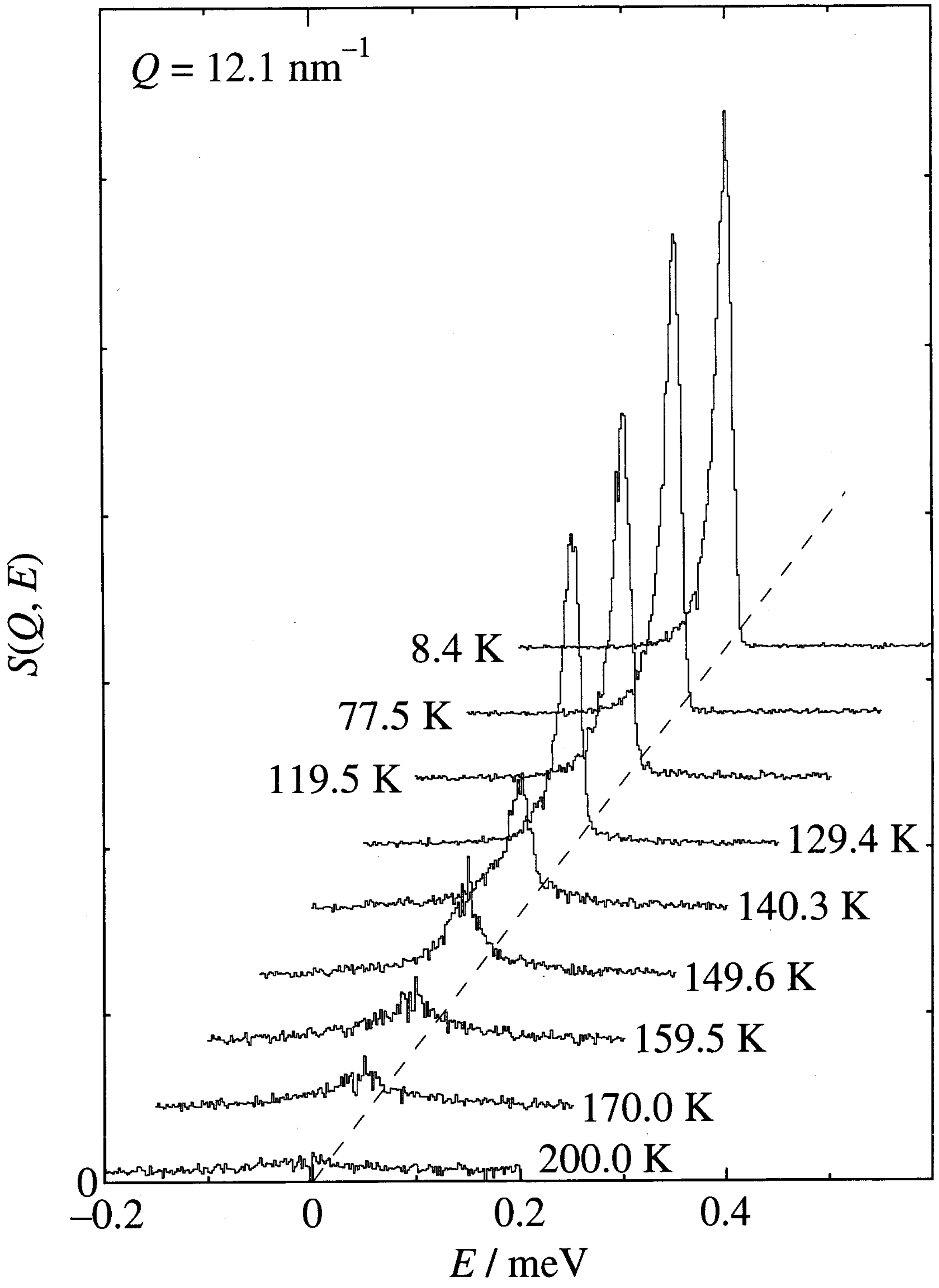

Fig. 3.9: Neutron scattering spectra obtained on LAM–80ET for TMS/graphite at θ = 1.55 at Q = 12.1 nm^{-1} with an instrumental resolution ΔE = 15 μeV. The background contribution has already been subtracted.

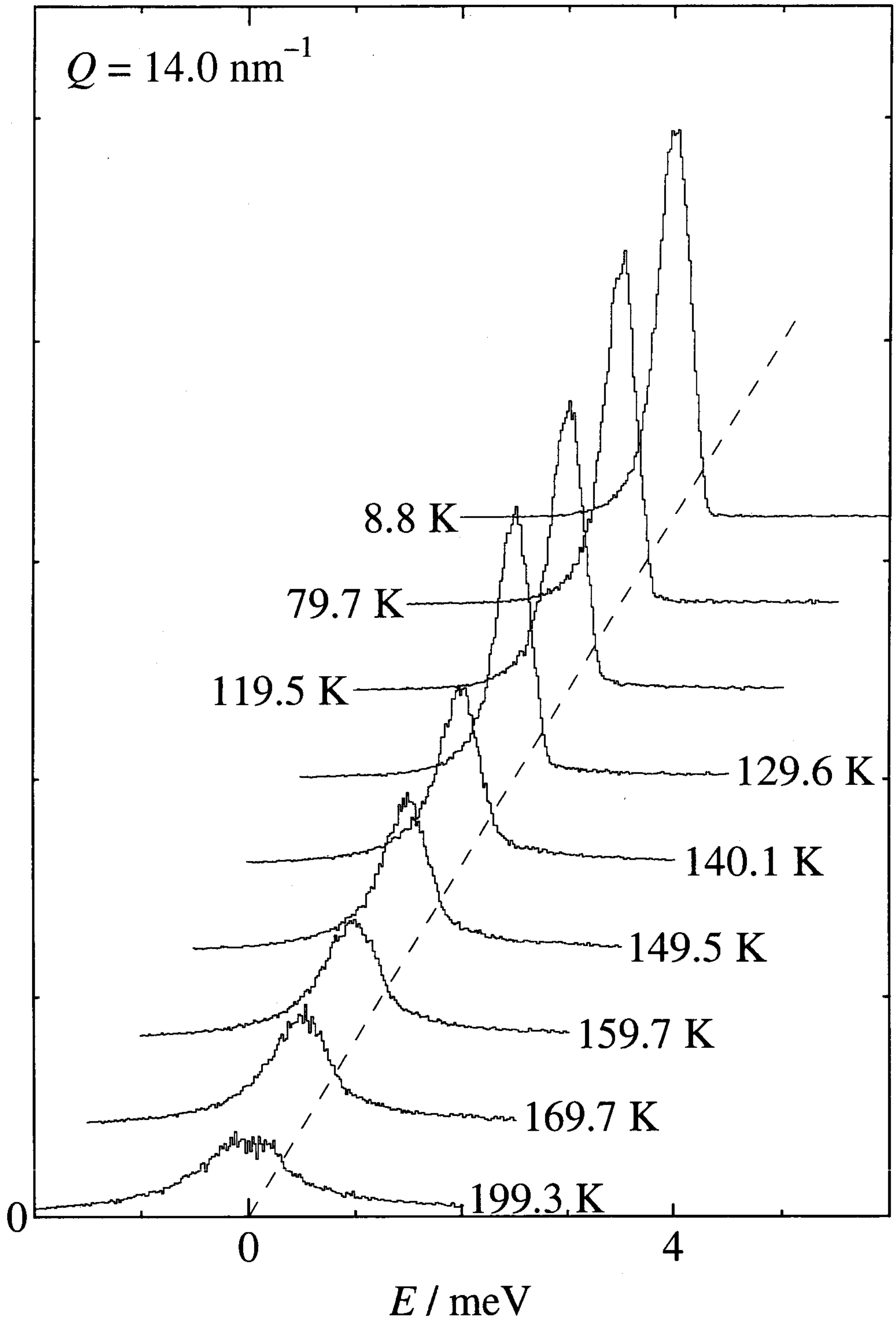

Fig. 3.10: Neutron scattering spectra obtained on LAM–40 for TMS/graphite at $\theta = 1.54$ at $Q = 14.0\ \mathrm{nm}^{-1}$ with an instrumental resolution $\Delta E = 200\ \mu\mathrm{eV}$. The background contribution has already been subtracted.

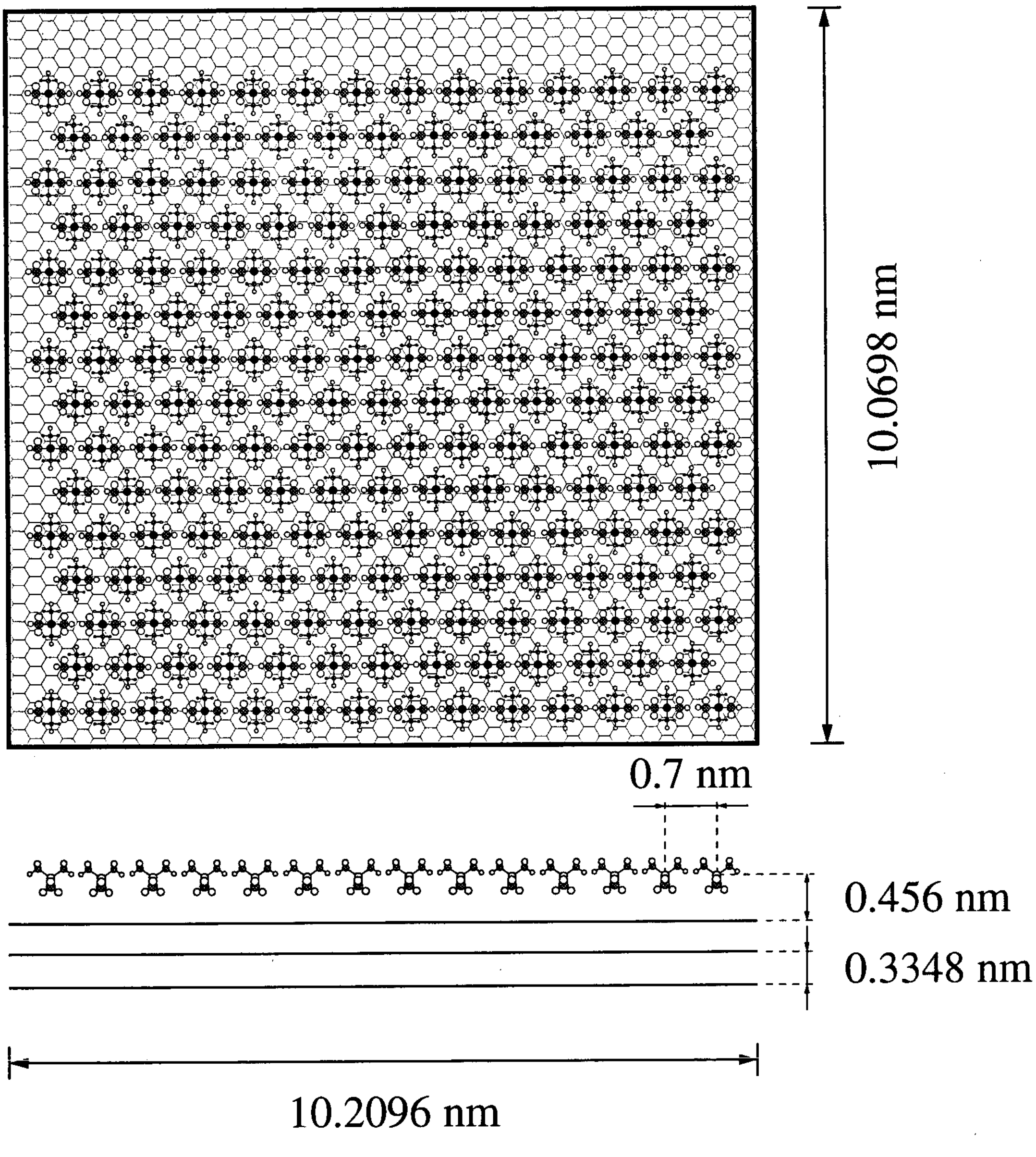

Fig. 3.11: Initial configuration for the MD simulation of TMS/graphite at $\theta = 0.724$.

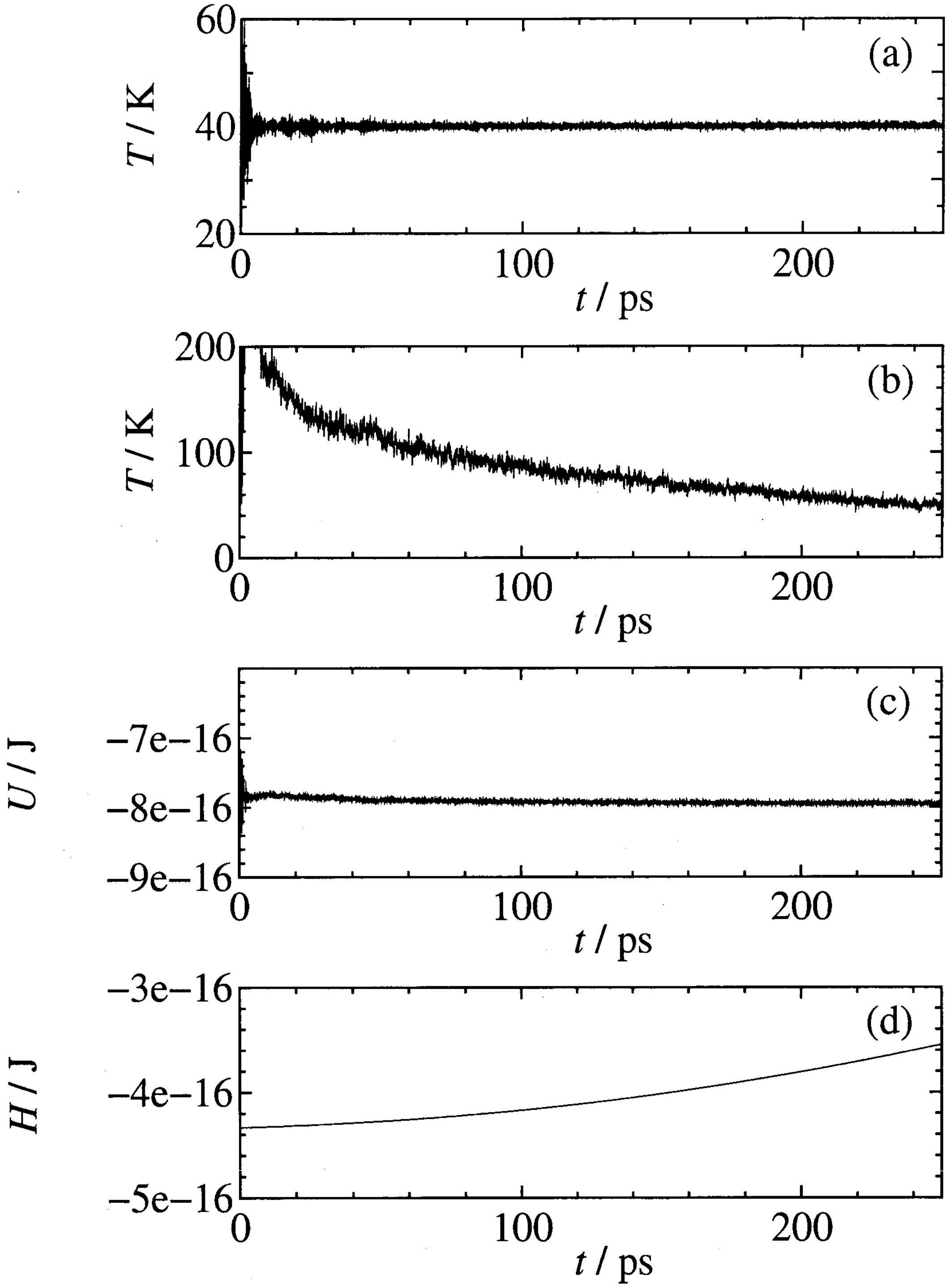

Fig. 3.12: Time evolution of the instantaneous temperature (a), the instantaneous temperature of the adsorbate calculated from their center-of-mass velocities (b), the internal energy (c) and hamiltonian (d) obtained from the MD simulation of TMS/graphite at θ = 0.724 at the simulating temperature 40 K.

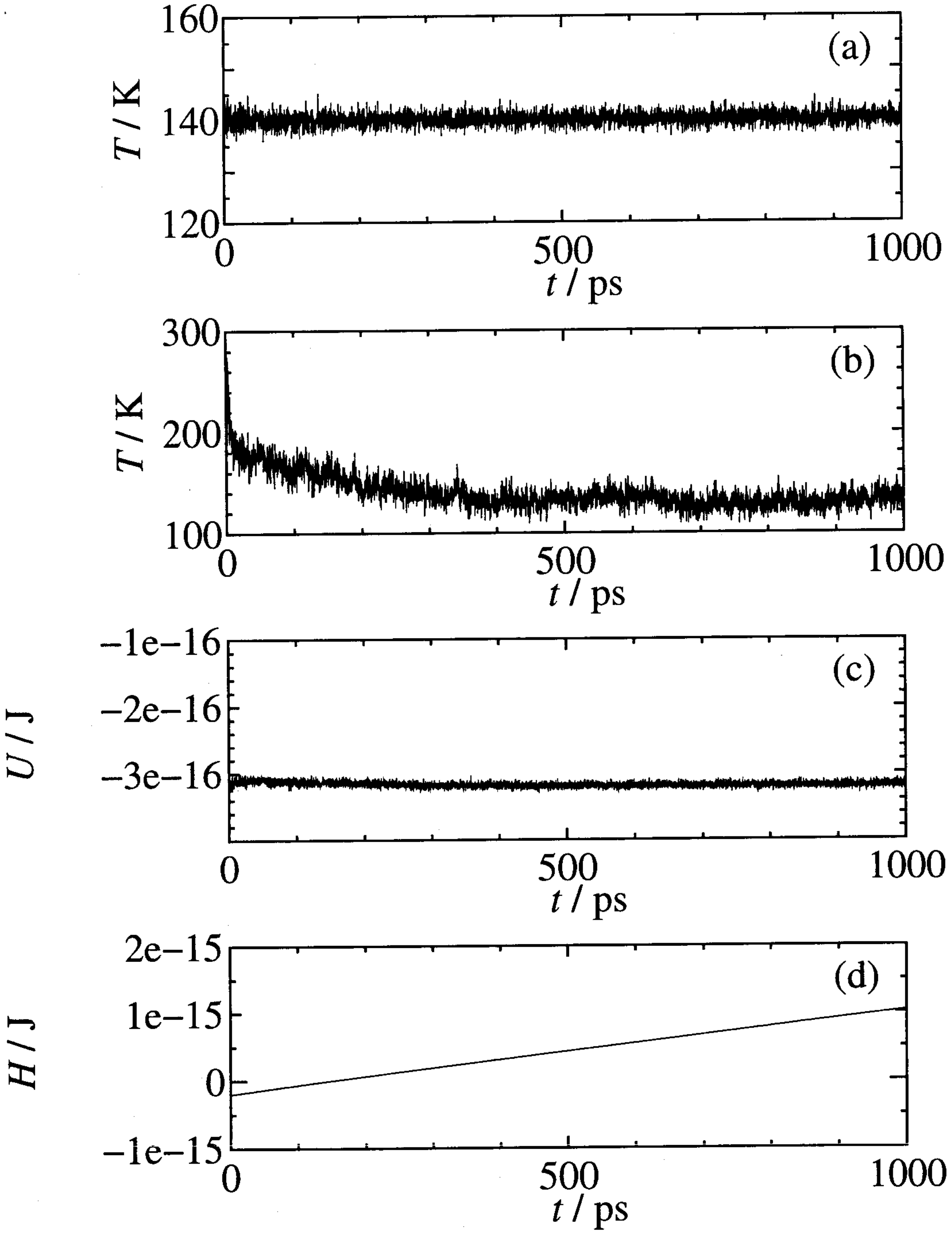

Fig. 3.13: Time evolution of the instantaneous temperature (a), the instantaneous temperature of the admolecules calculated from their center-of-mass velocities (b), the internal energy (c) and hamiltonian (d) obtained from the MD simulation of TMS/graphite at $\theta = 0.724$ at the simulating temperature 140 K.

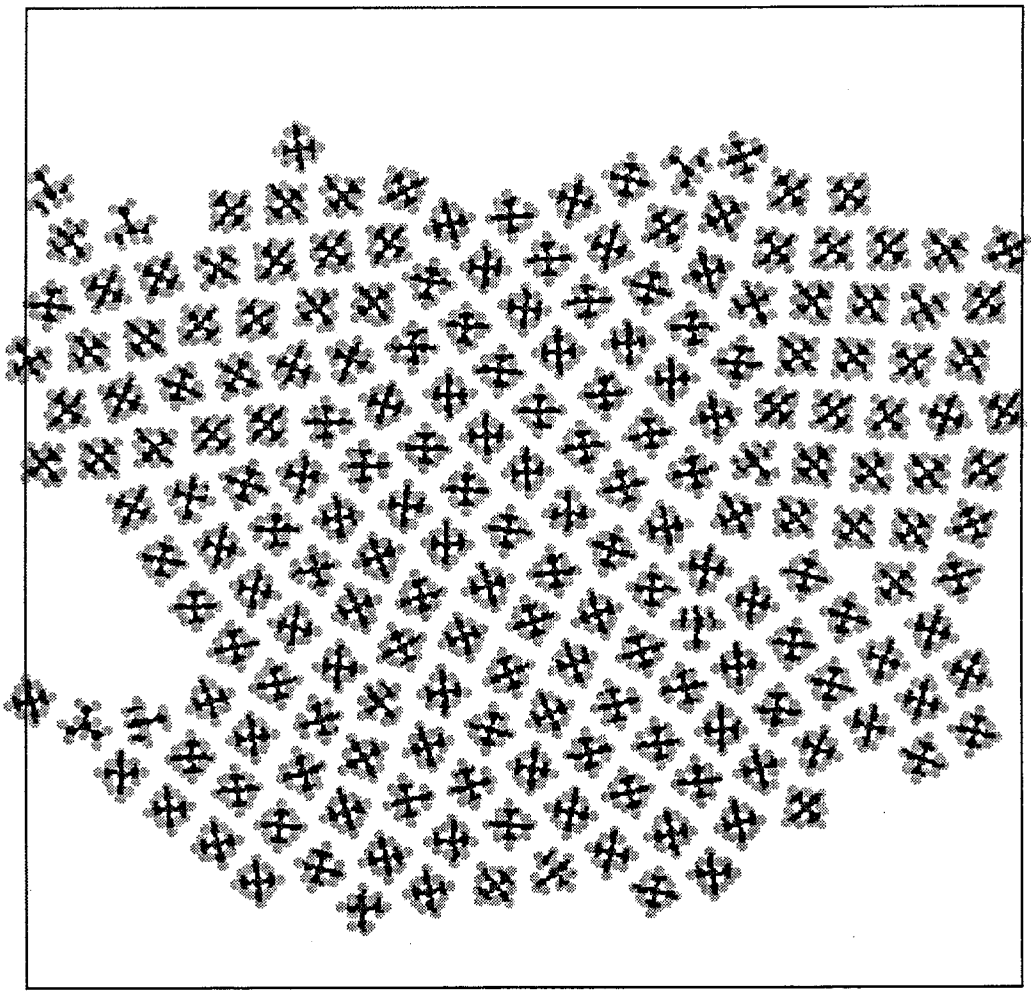

Fig. 3.14: A snapshot of the orientationally ordered monolayer of TMS on graphite obtained from the MD simulation at 40 K at $\theta = 0.724$.

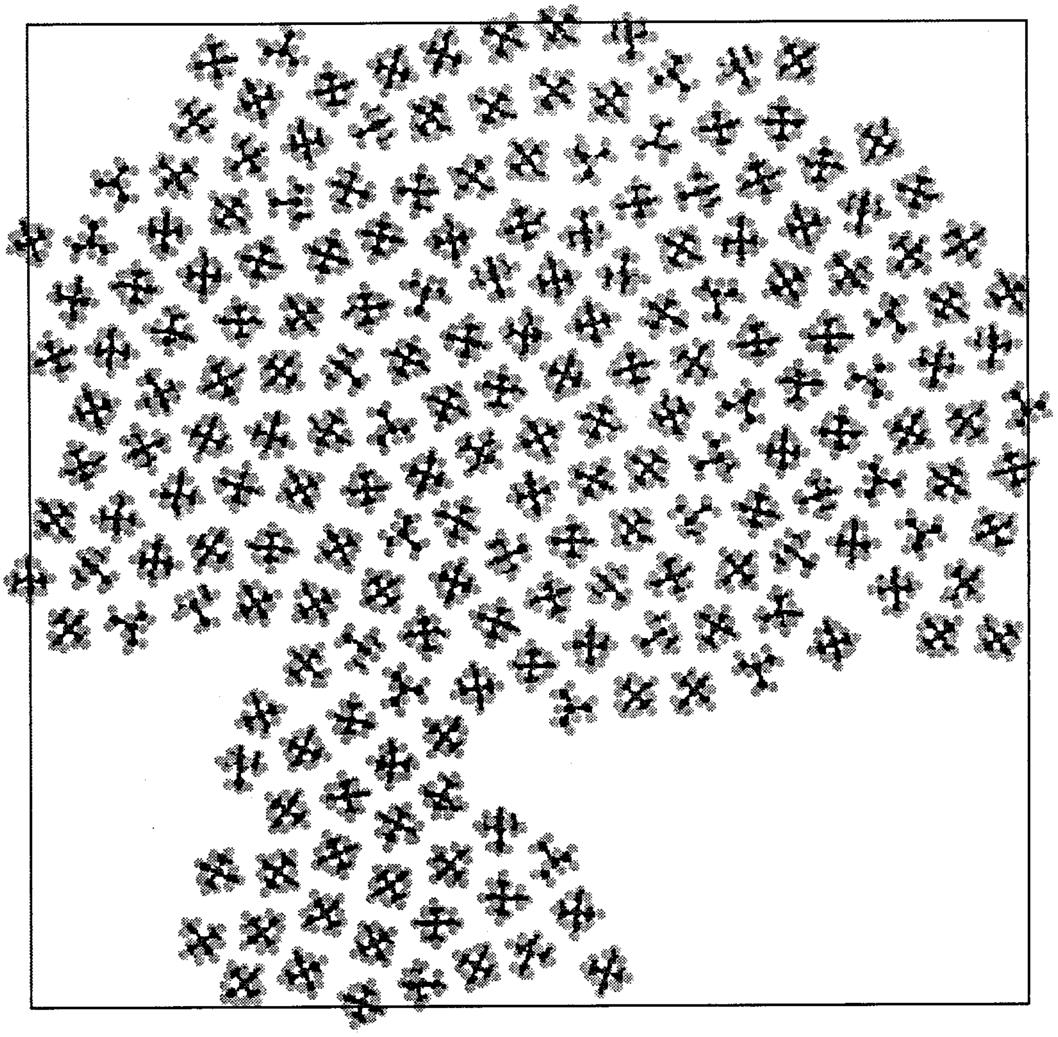

Fig. 3.15: A snapshot of the orientationally disordered monolayer of TMS on graphite obtained from the MD simulation at 140 K at $\theta = 0.724$.

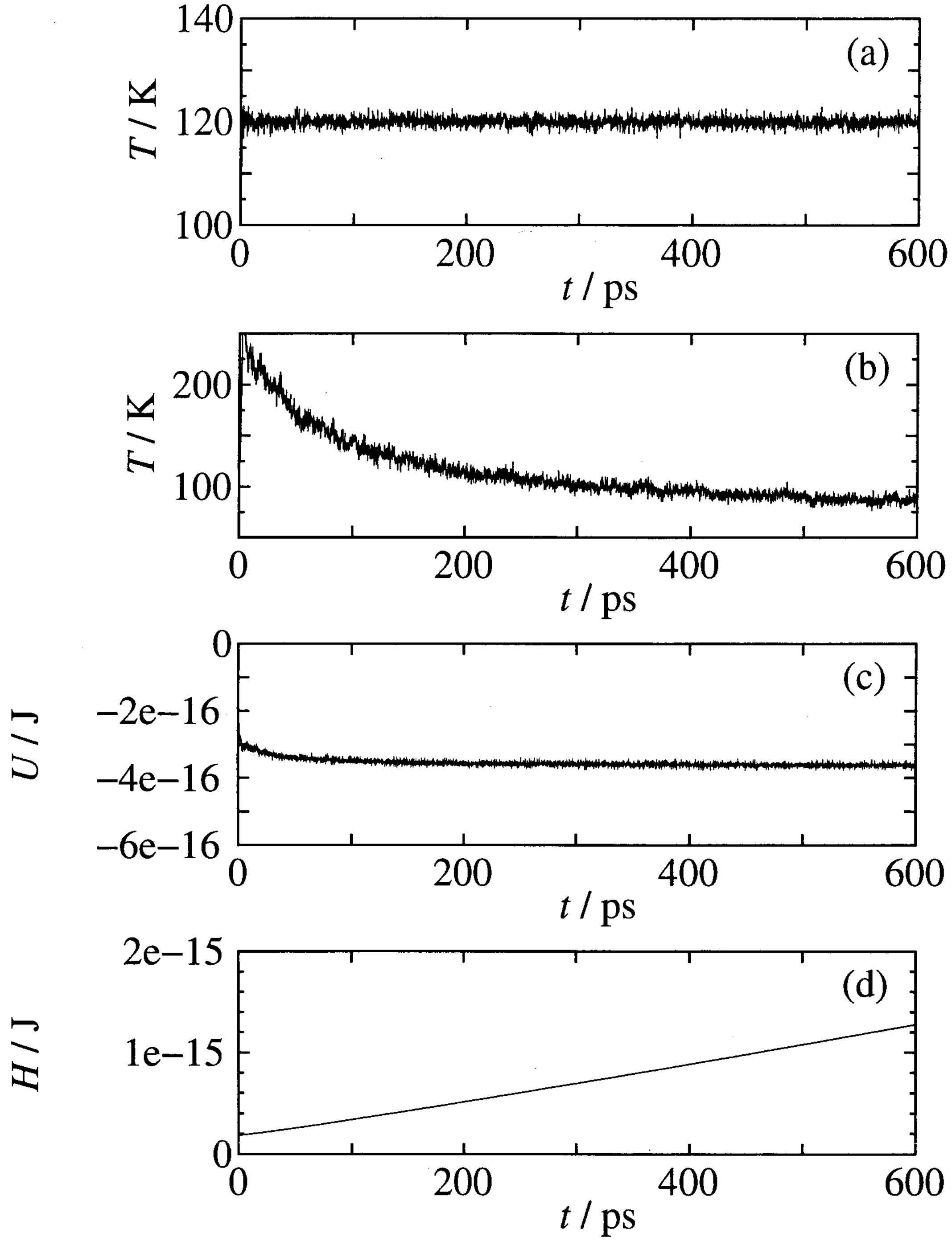

Fig. 3.16: Time evolution of the instantaneous temperature (a), the instantaneous temperature of the admolecules calculated from their center-of-mass velocities (b), the internal energy (c) and hamiltonian (d) obtained from the MD simulation of TMS/graphite at $\theta = 1.40$ at the simulating temperature 120 K.

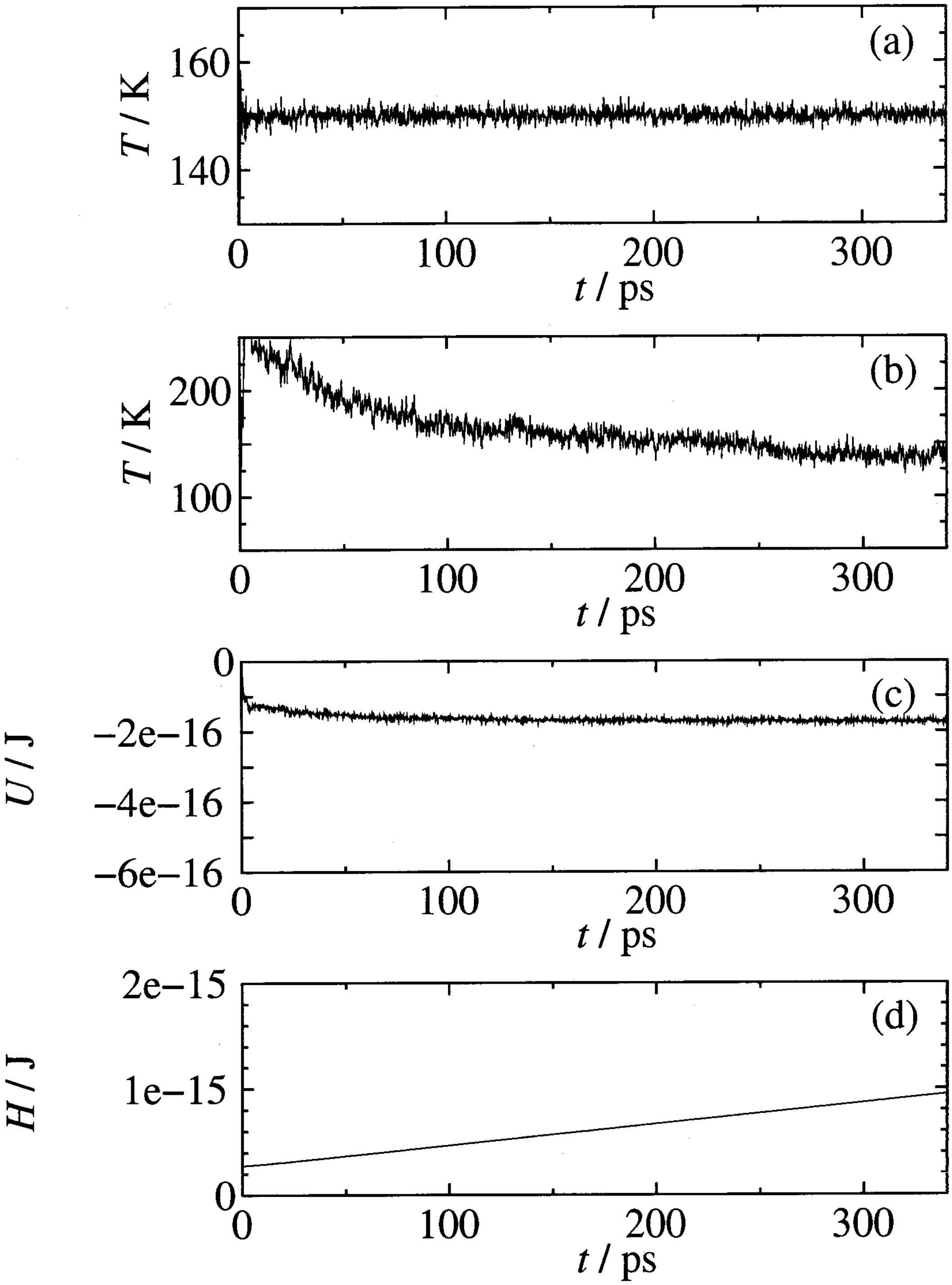

Fig. 3.17: Time evolution of the instantaneous temperature (a), the instantaneous temperature of the admolecules calculated from their center-of-mass velocities (b), the internal energy (c) and hamiltonian (d) obtained from the MD simulation of TMS/graphite at $\theta = 1.40$ at the simulating temperature 150 K.

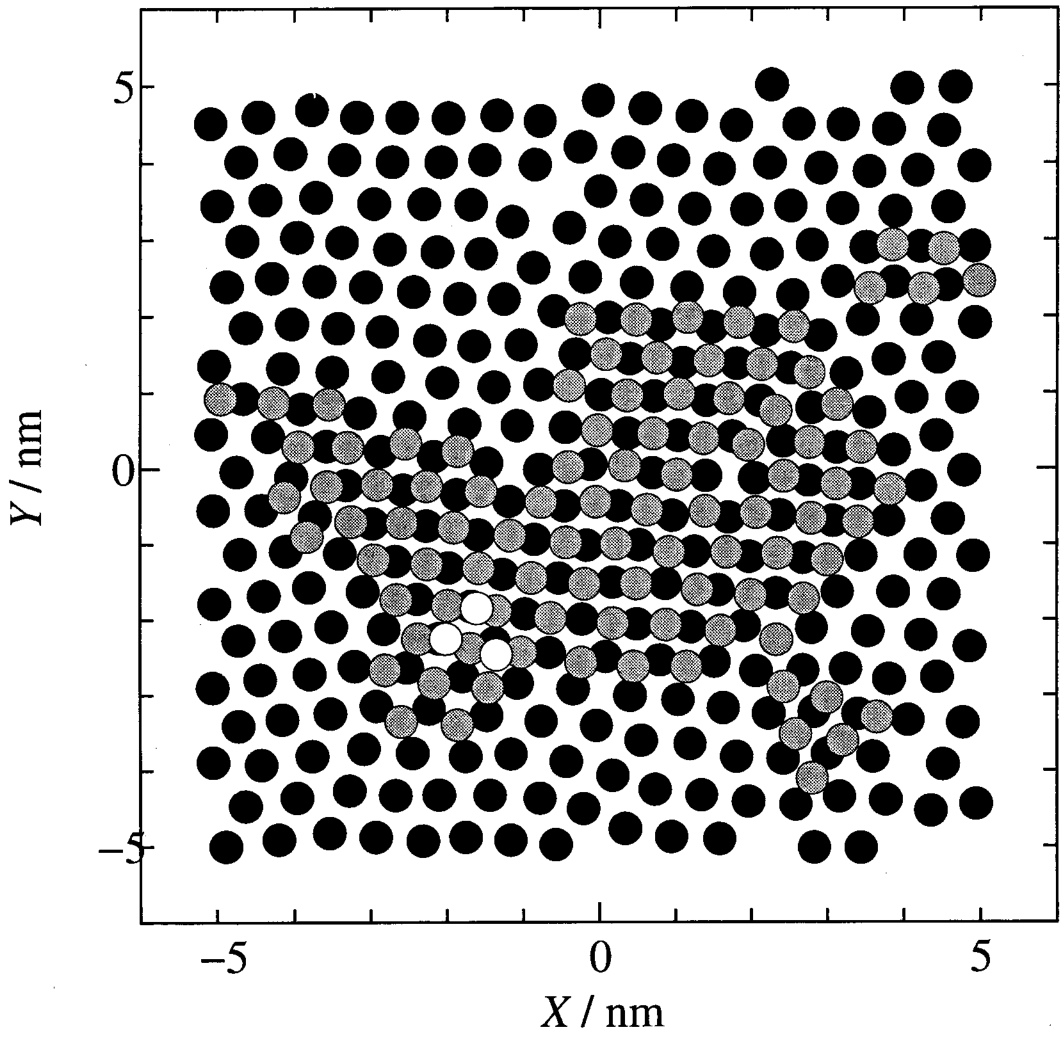

Fig. 3.18: Schematic illustration of the instantaneous molecular configurations obtained from the MD simulation at 120 K at θ = 1.40. Filled circles represents the molecules in the first layer, shaded circles in the second layer, and open circles in the third layer.

3.2 TMS/graphite at the coverage $\theta > 2$

3.2.1 Heat capacity

Heat capacity measurements were made for the multilayer at five different coverages θ ranging from 2.99 to 40.3. The amount of TMS and graphite are summarized in Table 3.4. The contribution of the heat capacity from the adsorbate was larger than that for the monolayer. For example, at $\theta = 2,99$, it was 6% of the total heat capacity at 15 K, 2% at 40 K, and 1.5% at higher temperatures except at the transition temperatures. This improved the accuracy of the heat capacity measurement for the multilayer, being estimated to be $\approx$ 2% or better over the whole temperature range.

Table 3.4: Amounts of adsorbent and adsorbate for each sample at $\theta > 2$.

Coverage	Papyex / g	TMS / mmol
2.99	9.207 (D)	1.908
4.96	9.207 (D)	3.164
9.99	9.207 (D)	6.368
20.0	9.207 (D)	12.73
40.3	9.207 (D)	25.69

Fig. 3.19 illustrates the molar heat capacity obtained for TMS on graphite at $\theta = 9.99$. 6 anomalies each of which was different from that at $\theta < 2$ were observed at this coverage, at T =150 K, 160 K, 165 K, 170 K, 173 K and around 185 K. Among these anomalies, each of them from 165 K to 173 K corresponds to that for the melting point of each solid phase (α, β and γ-phase) of the bulk, indicating that these three solid phase are formed simultaneously at this coverage. Although, as illustrated in Fig. 3.20, the heights of anomalies due to the bulk melting were different at each measurement series, these were always observed irrespective of the experimental conditions such as the cooling rate, annealing, etc. Furthermore the system seemed to be in equilibrium at least in our experimental time scale. It was also found that both of the β and γ-phases were easily supercooled while the α-phase was not. It has been pointed out that the γ-phase undergoes the phase transition to form the α-phase under high pressure [20].

However the phase transition of ordering the α-phase has not been found. We consider that the prominent anomaly at 160 K is due to the phase transition of the α-phase to form a ordered solid at low temperature.

Fig. 3.21 illustrates the molar heat capacity obtained for TMS on graphite at $\theta = 40.3$. The amount of γ-phase increased according to the increase of the amount of adsorbate, while the anomalies at 150 K and around 185 K were suppressed in the molar heat capacity, indicating that they did not originate in the bulk phase formed at the multilayer. Thus we consider that the anomaly around 185 K is due to the melting of the solid monolayer formed at the liquid–graphite interface, and hence the one at 150 K is due to the solid-solid phase transition of the monolayer. Such solid monolayers have been investigate for alkanes [59–65] and monocarboxylic acids [59, 66,67] adsorbed on graphite, and it has been found that the melting point of the monolayers are about 10% higher than that of the bulk solid.

Fig. 3.22 illustrate the molar heat capacity obtained for TMS on graphite at $\theta = 2.99$. The bulk β and γ-phases were no longer formed, while the α-phase was formed. The prominent anomaly at 139 K is due to the phase transition observed for the monolayer at $1 < \theta < 2$, i.e. the monolayer formed at the gas–graphite interface, indicating that the bulk phase wets only a part of the surface. The anomaly around 155 K is due to the melting of the monolayer formed at the gas–graphite interface.

The phases formed in the multilayer are summarized in Table 3.5, indicating that the α and β-phases which are metastable in the isolated bulk solid are preferentially formed near the surface of graphite.

We have estimated the baselines according to the following basis. The step in the heat capacity should be assigned to the anomalies of the bulk phases, i.e., the phase transition of the α-phase at 160 K, the melting of the β-phase at 170 K and the melting of the γ-phase at 173 K. The ratio of each step height should reflect the ratio of each bulk phase formed, being calculated based on the entropy values reported for the bulk solid [9]. The step height at the phase transition of the α-phase should be comparable to the sum of the transition and the melting entropy of the α-phase. Furthermore, these values converted to the quantities per unit mol of the α-phase should be comparable to the melting entropy of either the β-phase or the γ-phase, i.e., 30 ~ 40 $\mathrm{JK^{-1}mol^{-1}}$. This strategy requires the knowledge of the quantity of each bulk phase, and hence must be iterated for several times to converge the results. The converted

Table 3.5: Summary of the phases formed in the multilayer of TMS adsorbed on graphite. Note that G/S and L/S stand for the gas–graphite interface and the liquid–graphite interface, respectively.

Coverage	Monolayer		Bulk		
θ	at G/S	at L/S	α-phase	β-phase	γ-phase
2.99	Yes	Yes	Yes	—	—
4.96	Yes	Yes	Yes	Yes	—
9.99	—	Yes	Yes	Yes	Yes
20.0	—	Yes	Yes	Yes	Yes
40.3	—	Yes	Yes	Yes	Yes

values of the step height at 160 K and the sum of the transition and melting entropy of the α-phase are summarized in table 3.6 only for the representative results, showing that both values are reasonably close to each other. Since the peak height of the α-phase melting observed at the lower two coverage (θ = 2.99 and 4.96) is small, the inaccuracy of their values should be relatively large.

Table 3.6: Sum of the transition and the melting entropy of the α-phase (center column) and the step height at 160 K in the baselines (right column). These values are converted to the quantity per unit mol of the α-phase.

θ	$\Delta_{\mathrm{trs+fus}}S$ / JK^{-1}mol^{-1}	ΔC / JK^{-1}mol^{-1}
2.99	61.9	58.3
4.96	51.8	48.6
9.99	28.6	30.3
20.0	35.7	33.4
40.3	37.7	44.3

The entropies associated with the transition and the melting of both the monolayers and the bulk phases formed in the multilayer are summarized in table 3.7. Summarized here are only representative results. It should be mentioned that the anomaly due to the melting of the monolayer formed at the gas–graphite interface was too small to calculate the associated entropy.

Table 3.7: Transition and melting entropies of both the monolayers and the bulk phases formed at $\theta > 2$. The values associated with the monolayers are listed in the center column. Note that 139 K, 150 K and 185 K stand for the transition of the monolayer at the gas–graphite interface, the transition of the monolayer at the liquid–graphite interface and the melting of the monolayer at the liquid–graphite interface, respectively. The values associated with the bulk phases are listed in the right column. Note that 160 K, 165 K, 170 K and 173 K stand for the transition of the α-phase, the melting of the α-phase, the melting of the β-phase and the melting of the γ-phase, respectively.

	ΔS / JK^{-1}mol^{-1}						
Coverage	Monolayer			Bulk			
θ	139 K	150 K	185 K	160 K	165 K	170 K	173 K
2.99	4.3	0.6	1.2	12.1	0.9	—	—
4.96	0.5	3.6	0.7	15.7	1.4	—	—
9.99	—	1.9	0.6	12.2	2.1	8.7	1.7
20.0	—	0.9	0.2	13.2	1.8	13.5	2.8
40.3	—	0.2	0.1	10.4	1.3	9.3	14.9

Fig. 3.23 illustrates the low-temperature heat capacities of TMS on graphite at $\theta > 2$. A glass transition was observed around 60 K. The height of the heat-capacity step at the glass transition depended on the coverage. Fig. 3.24 illustrates the spontaneous temperature drift observed at $\theta = 40.3$. It is evident that the exotherm drift below the glass transition point is almost equal to zero. The glass had never crystallized in our experiments.

3.2.2 Neutron scattering

Neutron scattering experiments were performed for TMS/graphite at $\theta = 3.07$ with LAM–80ET spectrometer. The amount of TMS was 5.818 mmol for 26.83 g of graphite (A). A greater part of the elastic scattering intensity decreased at the temperatures between 120 K and 160 K, where the phase transitions of three solid phases, the monolayer at the gas–graphite interface, the one at the liquid–graphite interface and the bulk α-phase, were observed for this coverage. The elastic intensity did not change dramatically at the melting point of the monolayer at liquid–graphite interface (around 185 K).

3.2.3 MD simulation

The calculating conditions (ensemble, potential functions, integration algorithm and time step) were same as for the monolayer. The simulation system was similar to that employed for the monolayer except the following two points. One was the system size, which was smaller than that for the monolayer, as mentioned in the previous chapter. The other was using an united-atom molecular model in which each methyl group was represented by one pseudoatom of mass 15.035 amu.

Layers of TMS molecules arranged in a hexagonal lattice with a_c = 0.7 nm were stacked up along the vertical axis with layer-layer spacing of 1.1 nm. 1300 of TMS molecules were then stacked with the surface of graphite to form 10 layers. Corresponding coverage was 7.28. Each of TMS molecule was placed in each layer with dipod-down orientation. All the bond length and bond angles were allowed to vary. Three temperatures were simulated, 140 K, 180 K and 220 K. The simulating time was either 500 ps at 140 K or 600 ps at 180 K and 200 K. The simulation conditions are summarized in Table 3.8.

Table 3.8: Simulation conditions for the TMS multilayer on graphite. Note that N_m, N_a, T and t stand for the number of molecules, the total number of atoms in the simulation system, the simulating temperature and the total simulating time, respectively.

θ	N_m	Surface area (nm^2)	N_a	Ensemble	T / K	t/ ps
7.28	1300	8.0826×8.1048	14024	*NVT*	140	500
7.28	1300	8.0826×8.1048	14024	*NVT*	180	600
7.28	1300	8.0826×8.1048	14024	*NVT*	200	600

The physical quantities of the simulation system evolved with time more desirably than that for the monolayer simulation. The results, for example, obtained from the simulation at 180 K are illustrated in Fig. 3.25. The energy drift of the hamiltonian was 0.002%/ps, showing good conservation. The discrepancy between the system temperature and the temperature of the admolecules converged after c. a. 400 ps and hence the total simulation system reached equilibrium at the simulating temperature.

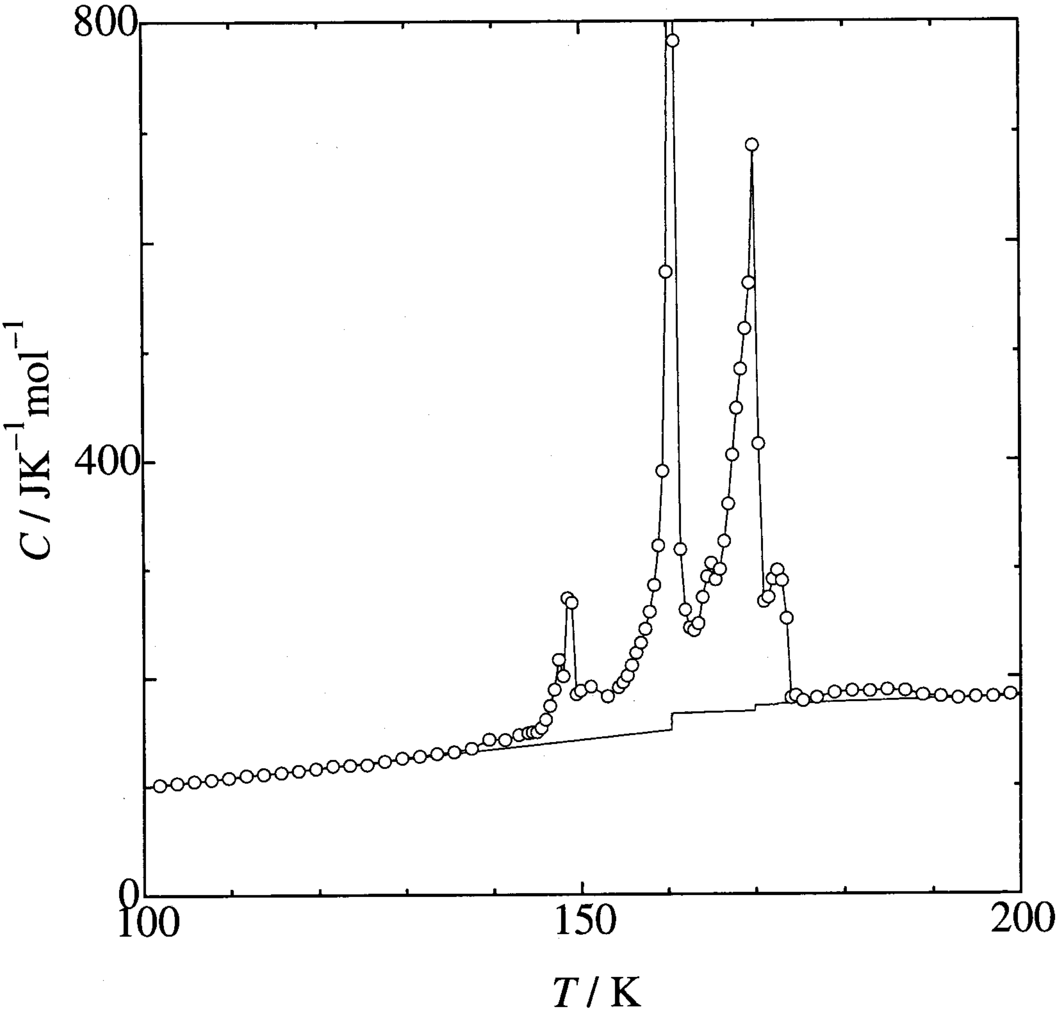

Fig. 3.19: Molar heat capacity of TMS on graphite determined at coverage θ = 9.99. The estimated baselines are also indicated.

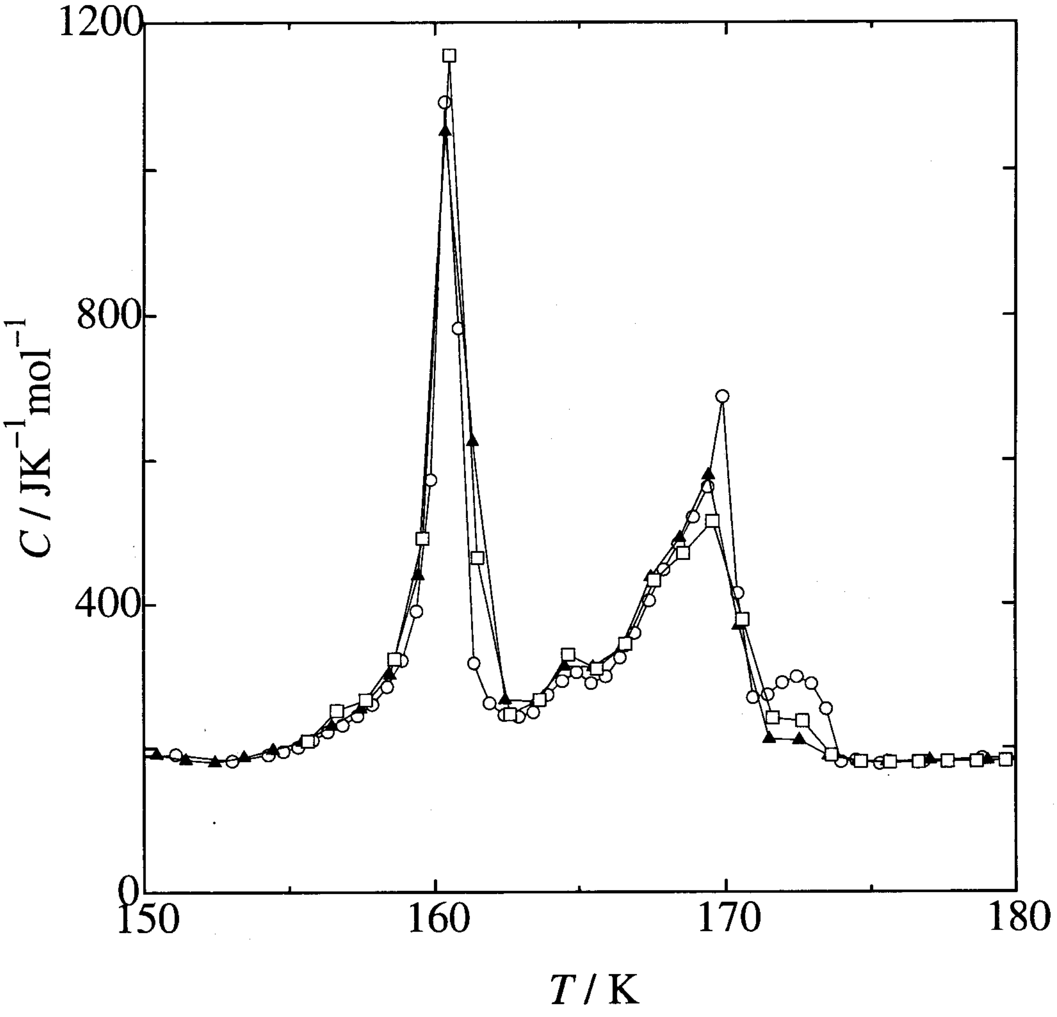

Fig. 3.20: Enlarged illustration of the molar heat capacities of TMS on graphite at $\theta = 9.99$ at the temperature range between 150 and 180 K. Note that each symbol describes each measurement series.

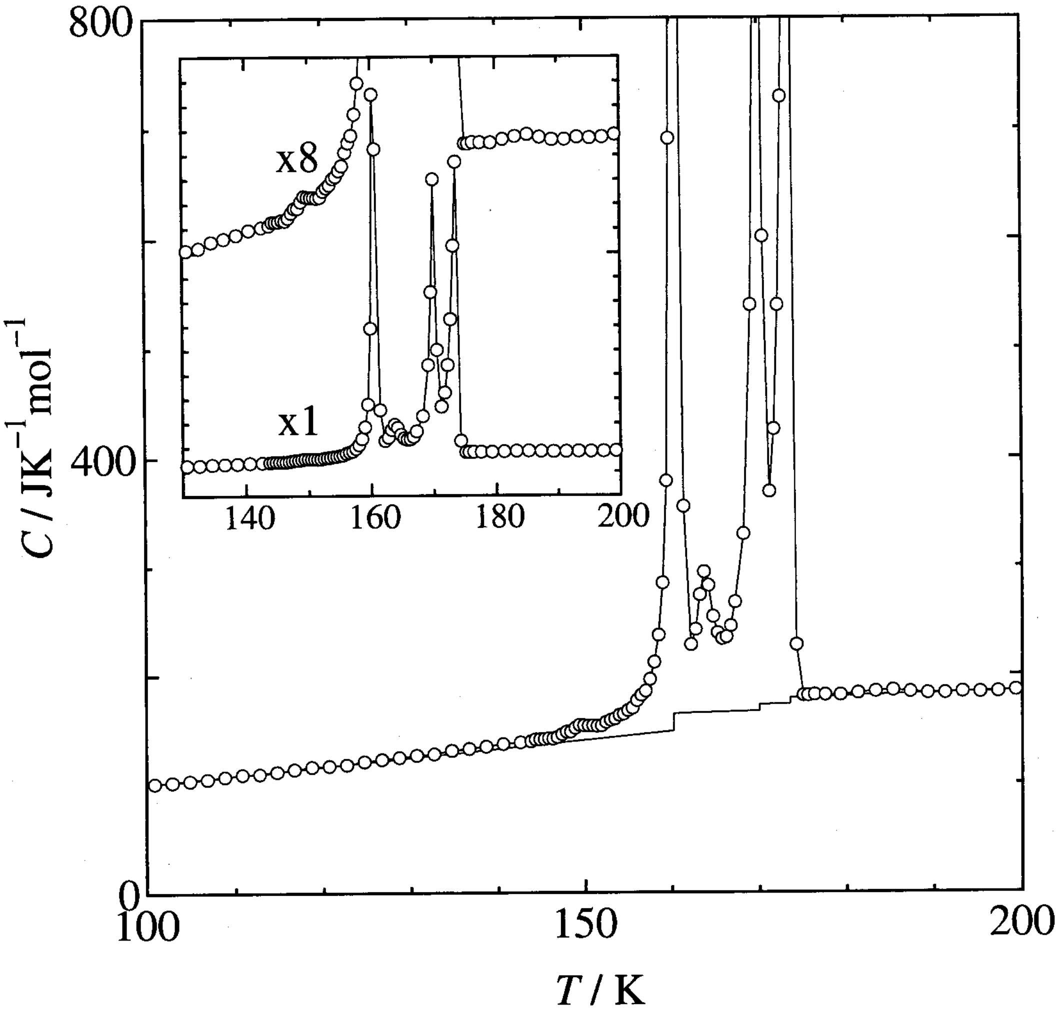

Fig. 3.21: Molar heat capacity of TMS on graphite determined at coverage θ = 40.3. The estimated baselines are also indicated. The inset illustrates the heat capacity multiplied by 8 to emphasize the anomalies at 150 K and around 185 K.

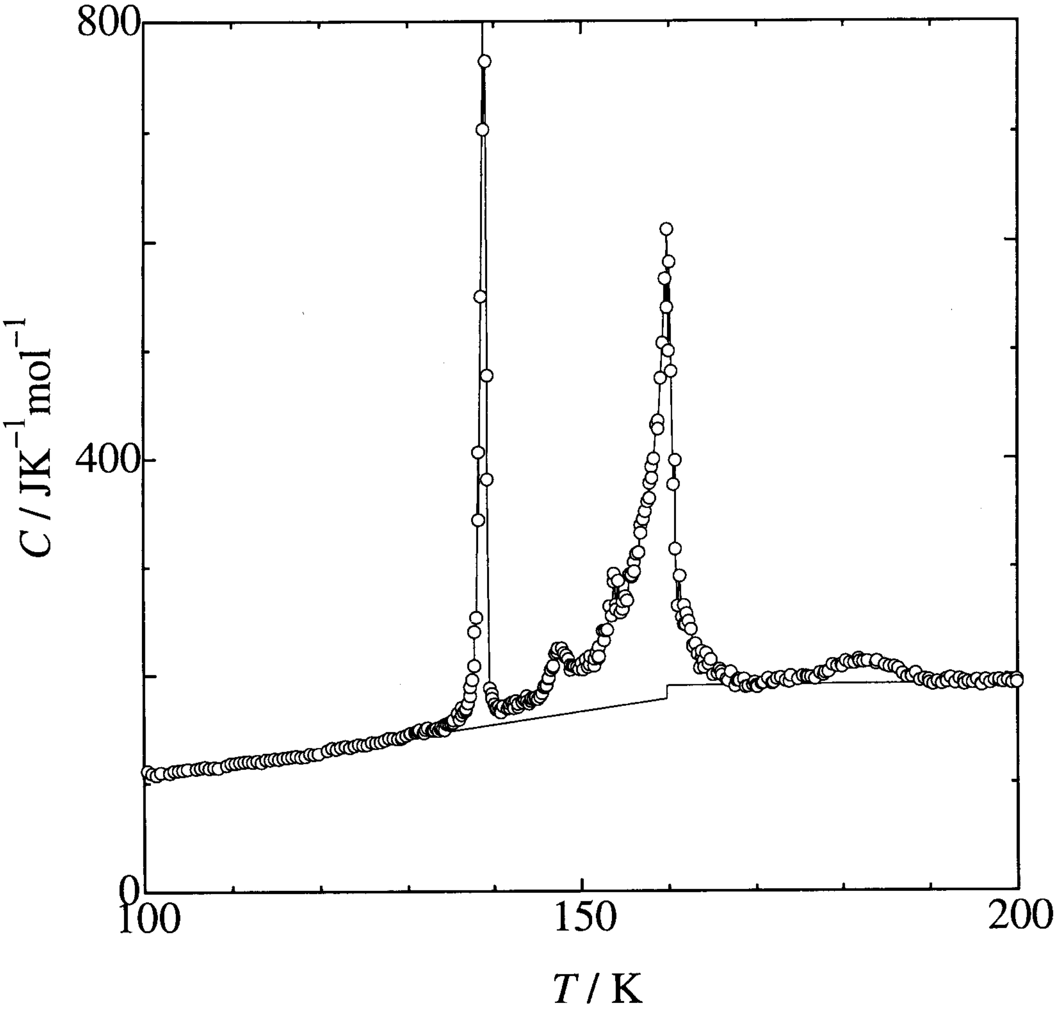

Fig. 3.22: Molar heat capacity of TMS on graphite determined at coverage θ = 2.99. The estimated baselines are also indicated.

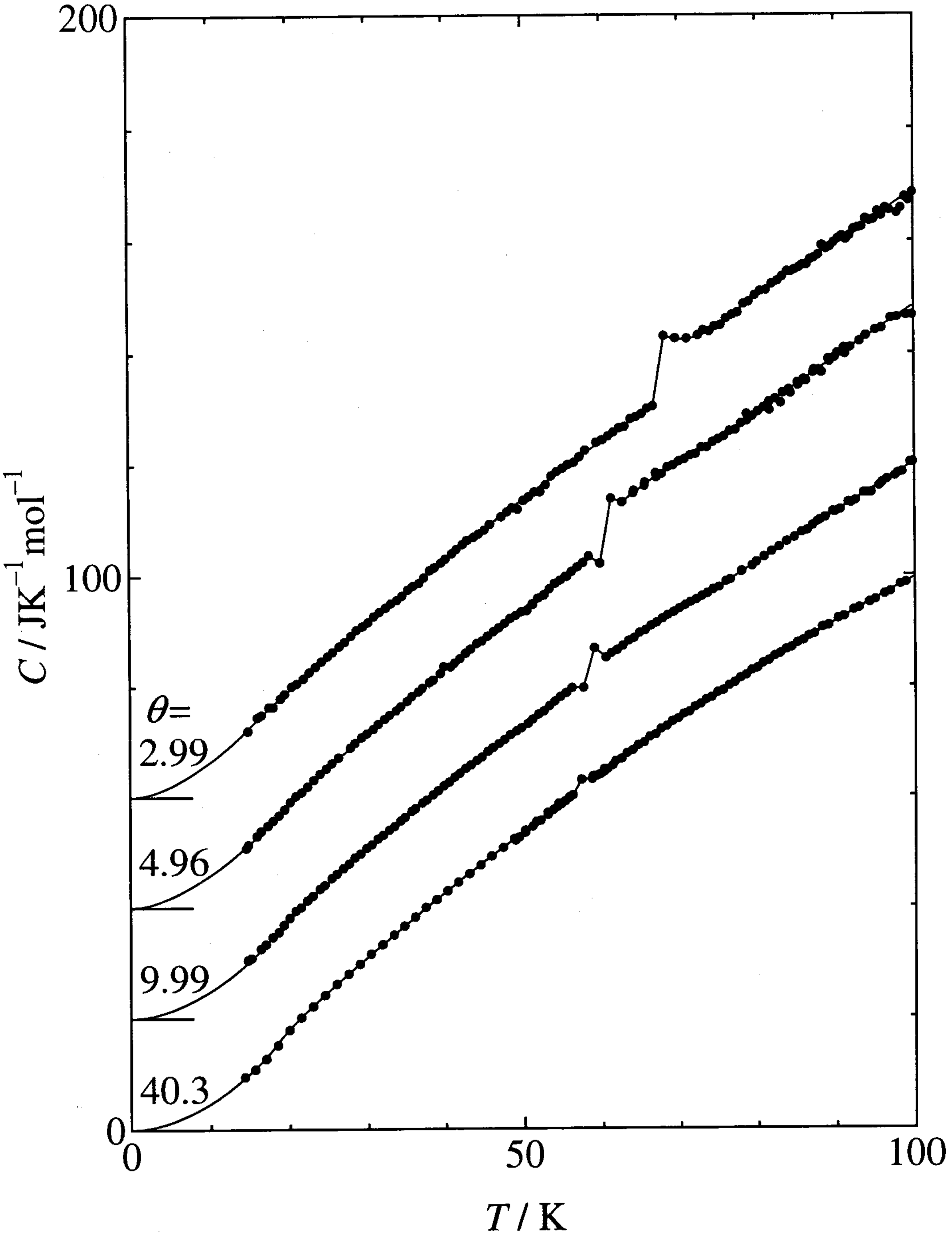

Fig. 3.23: Low temperature heat capacities for TMS on graphite at $\theta > 2$. Lines are drawn for guide of eyes. Note that the vertical scale of each curve is shifted from the next by 200 JK^{-1}mol^{-1}

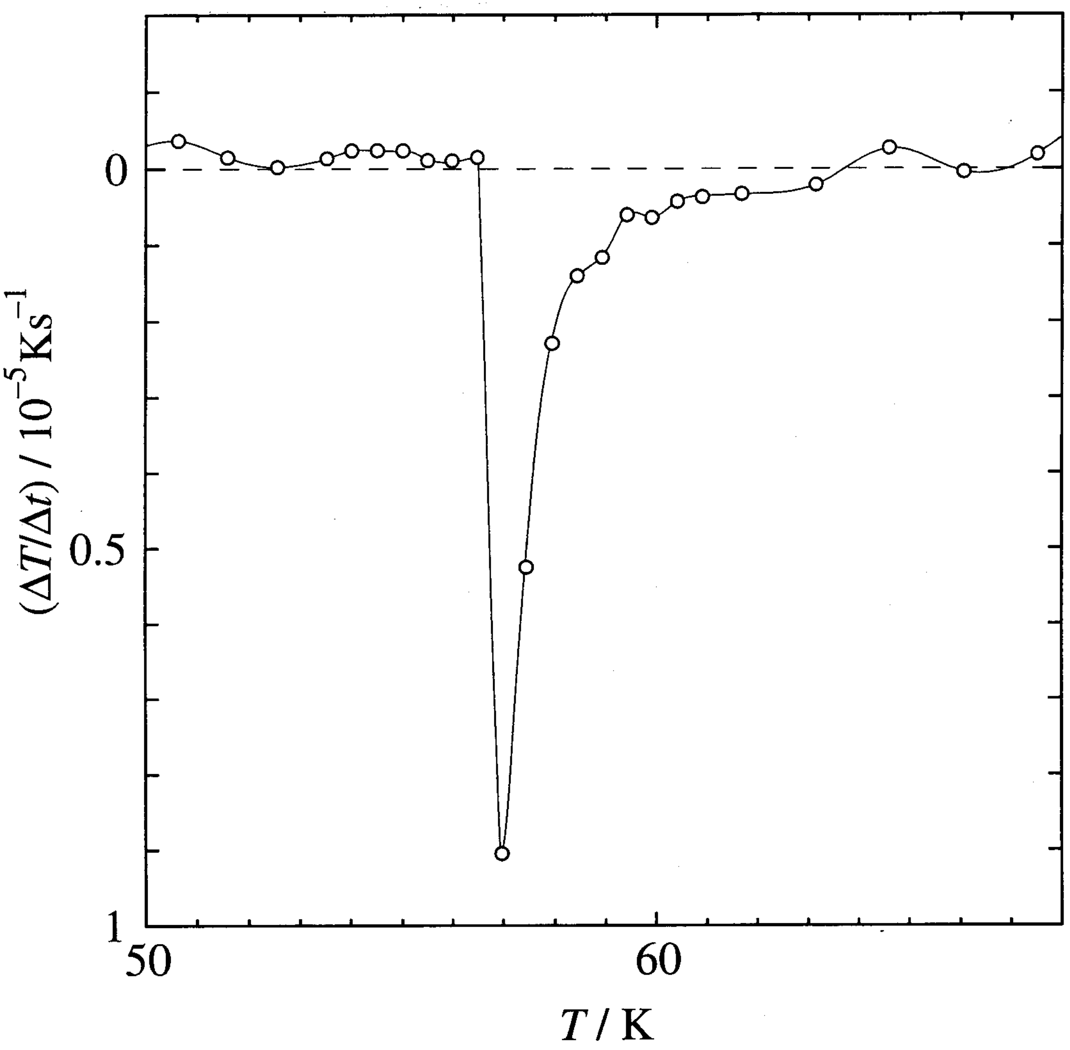

Fig. 3.24: Spontaneous temperature drift as a function of temperature observed for TMS on graphite at θ = 40.3.

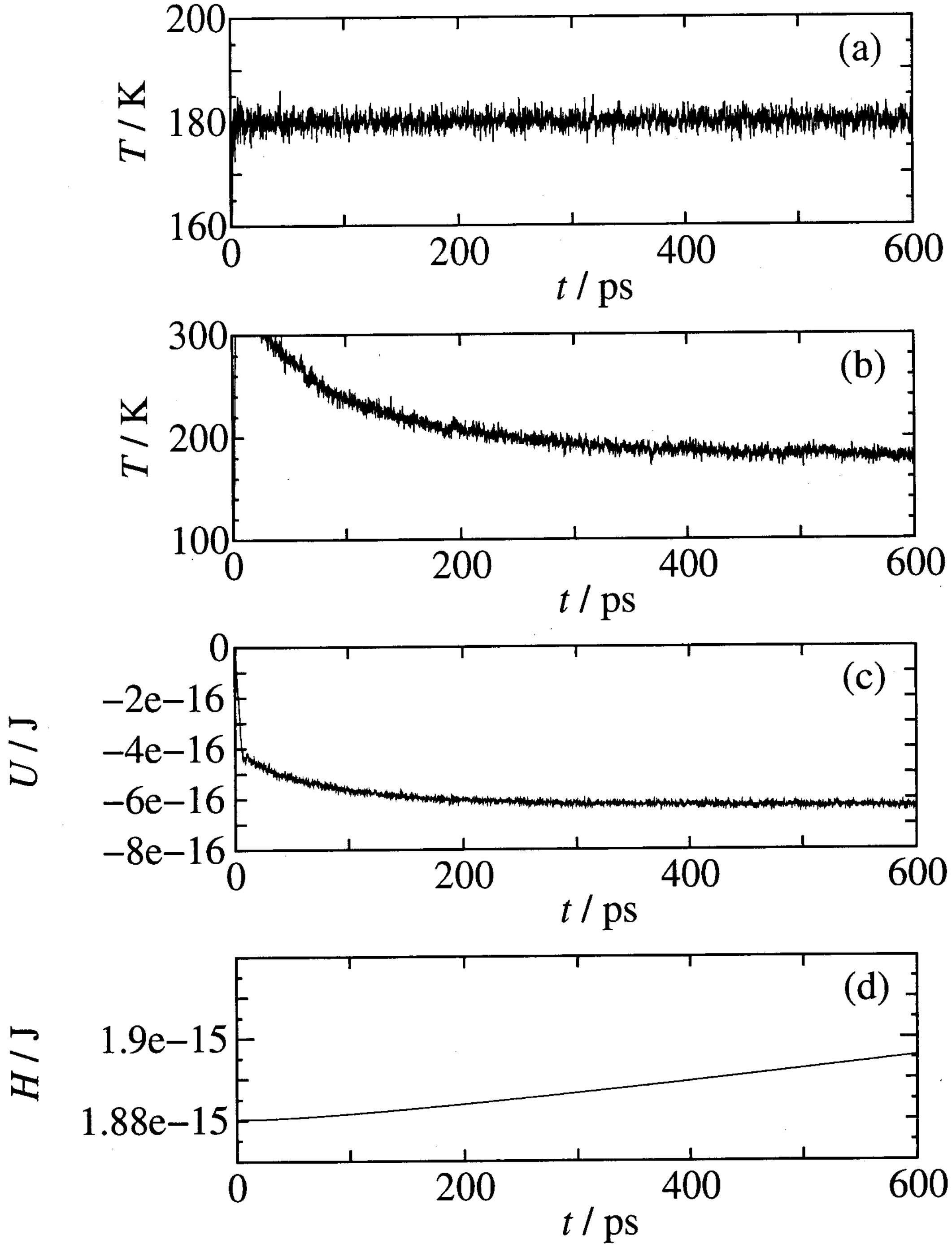

Fig. 3.25: Time evolution of the instantaneous temperature (a), the instantaneous temperature of the admolecules calculated from their center-of-mass velocities (b), the internal energy (c) and hamiltonian (d) obtained from the MD simulation of TMS/graphite at $\theta = 7.28$ at the simulating temperature 180 K.

3.3 TMS/MgO

3.3.1 Heat capacity

Heat capacity measurements were made for TMS on MgO at one coverage $\theta = 0.657$. The amount of TMS was 0.504 mmol for 14.87 g of MgO (11.4 m^2g^{-1}, a weighted average of the specimen E and F). Although the measurements were made in the temperature range between 4 and 200 K, it was found that the time required to achieve thermal equilibrium became longer with increasing temperature. At 50 K, for example, thermal equilibrium was reached within a minute after heating off for TMS/graphite, whereas 7 minutes were required for TMS/MgO, which lead to considerable inaccuracy of the heat capacities measured. This might be due to worse thermal contact either between the pellets or between the pellet and the calorimeter vessel. Therefore, heat capacities were obtained with acceptable accuracy only below 35 K, where the contribution of the heat capacity from the adsorbate is relatively large. It was approximately 3% below 12 K and 1% at 30 K, which are slightly larger than those for TMS/graphite. The molar heat capacity obtained for TMS/MgO is illustrated in Fig. 3.26, where that obtained for TMS/graphite at $\theta = 0.609$ and that reported for the bulk γ-phase [9] are also plotted for comparison. It is evident that the molar heat capacity of TMS/MgO is still larger than that of the bulk solid.

3.3.2 Neutron scattering

Neutron scattering experiments were performed for TMS on MgO at $\theta = 0.661$ with LAM–80ET spectrometer. The amount of TMS was 0.400 mmmol for 12.49 g of MgO (E). The spectra obtained at $Q = 12.1$ nm^{-1} are illustrated in Fig. 3.27. Although the spectra contain a large experimental error due to small amount of TMS (about one-fifth of that for TMS/graphite), it is evident that the elastic scattering intensity substantially decrease across c. a. 100 K and the remaining contribution dies out across c. a. 150 K, as is seen for TMS/graphite at $\theta = 1.04$.

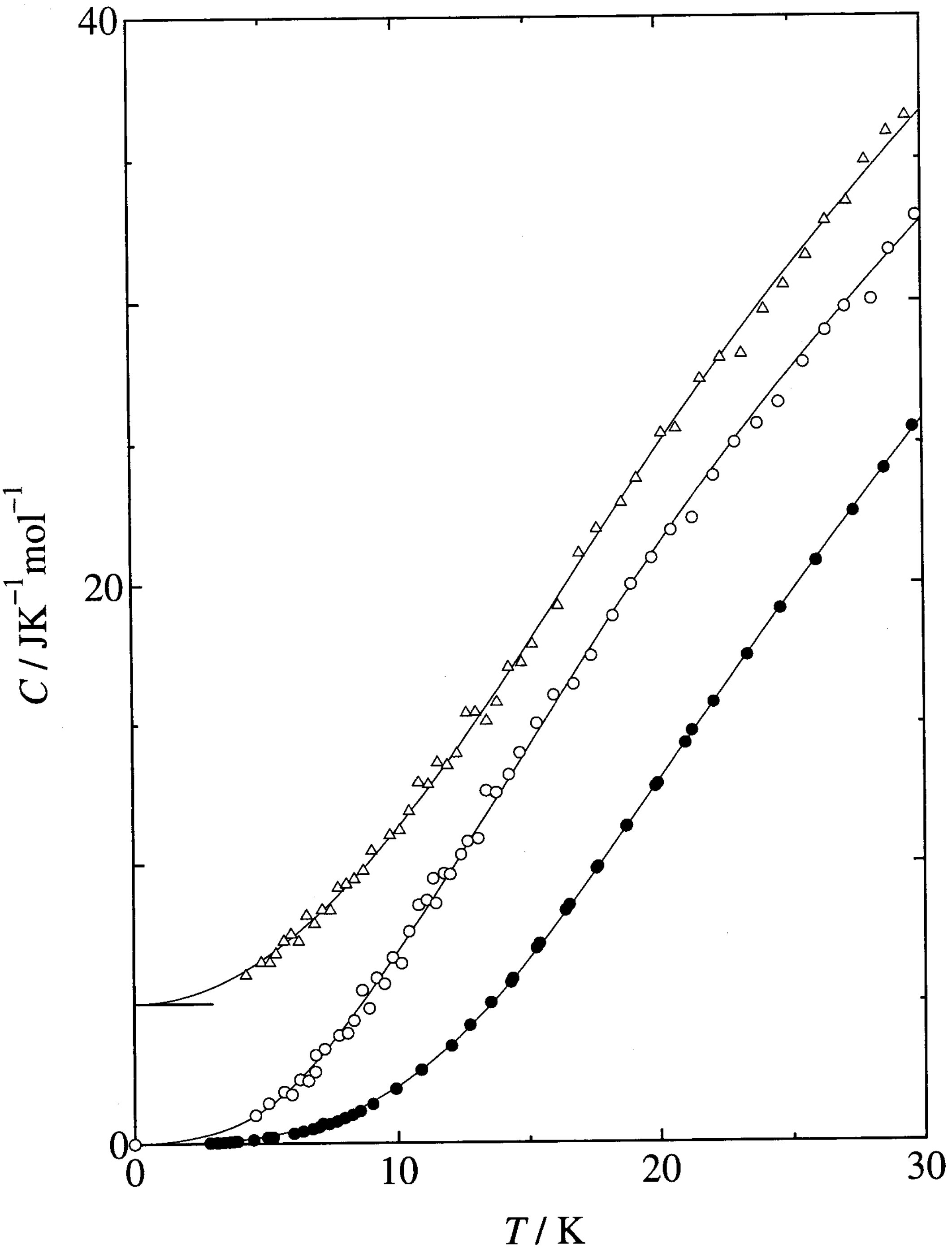

Fig. 3.26: Low-temperature heat capacity of TMS on MgO. Those obtained for TMS on graphite at $\theta = 0.609$ (triangles) and reported for the bulk γ-phase [9] (filled circles) are also plotted for comparison. Note that the vertical scale for TMS on graphite is shifted from the next by 5 JK^{-1}mol^{-1}

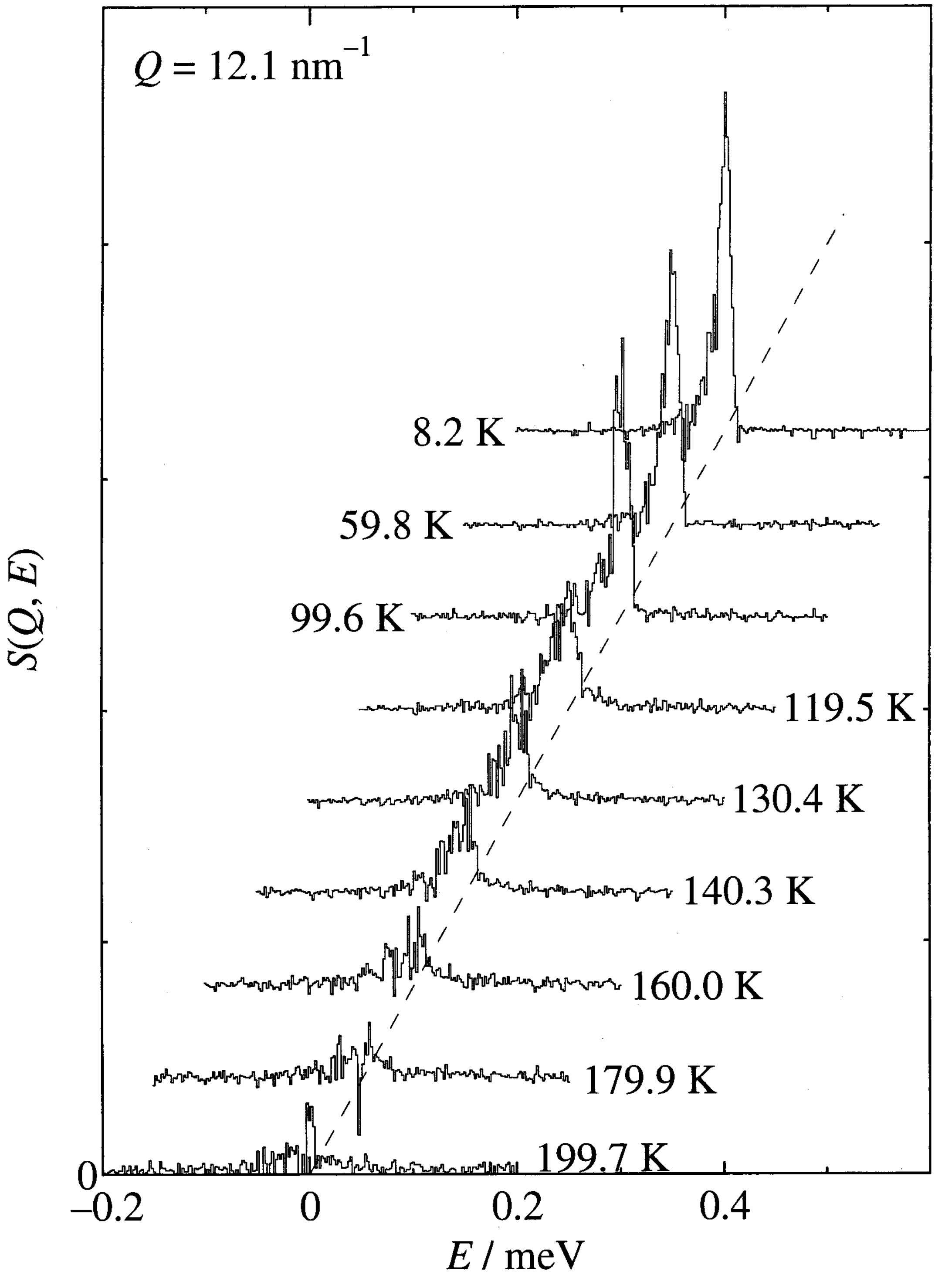

Fig. 3.27: Neutron scattering spectra obtained on LAM–80ET for TMS/MgO at $\theta = 0,661$ at $Q = 12.1\ \mathrm{nm}^{-1}$ with instrumental resolution $\Delta E = 15\ \mu\mathrm{eV}$. The background contribution has already been subtracted.

Chapter 4

Discussion

4.1 Monolayers at the gas–solid interface ($\theta < 2$)

4.1.1 Phase behavior

TMS/graphite

For an adsorbed monolayer system, it is considered that 2-D islands of the dense 2-D solid or liquid coexist with the dilute 2-D gas, except near the coverage corresponding to the complete monolayer. Thus, a transition point in the 2-D solid is actually a triple point. To describe the coverage dependence of the stability of various phases, a diagram shown in Fig. 4.1 has been constructed, and it has been referred to as the phase diagram conventionally (see references in Section 1.3), although one could not refer to it as a "phase diagram" in the strict sense of the word. Here we refer to the diagram in Fig. 4.1 as the phase diagram of TMS on graphite conventionally. The diagram is obtained from plotting the temperatures of the peak in the heat capacity along with the full-width-at-half-maximum. Although the transition temperature changes discontinuously at $\theta = 1$, the diagram indicates layer-by-layer adsorption taking place for $\theta < 2$. For higher coverage ($\theta > 2$), as shown in Chapter 3, the bulk phases appear to become stable. Thus TMS molecules wet the graphite surface only as a monolayer or a bilayer. When TMS is available in a quantity exceeding the bilayer capacity, it forms the bulk phase. Similar wetting behavior was reported for other systems [78].

Fig. 4.2 summarizes the experimental value of the entropy change and compares them with theoretical predictions. The theoretical predictions represent the entropy of ideal random occupation of the adsorption sites by the molecules available. It will be discussed later. As shown the open marks, the 2-D solid-phase transitions are accompanied by large entropy changes, $R \ln 8$ (17.3 $\mathrm{JK^{-1}mol^{-1}}$)–$R \ln 3$ (9.1 $\mathrm{JK^{-1}mol^{-1}}$), depending on the coverage. The coverage dependence can be understood by assuming that a part of the full value ($R \ln 8$) may be included in the entropy of melting for $\theta > 1$, since the transition and melting take place close to each other at high coverages. The large transition entropy is related to the disorder of molecular orientation in the high-temperature phase. If we assume a hexagonal structure (a likely structure for an effectively spherical molecule), the largest possible number of equivalent orientations would be 12. The entropy of such orientational disorder is $R \ln 12$ (20.7 $\mathrm{JK^{-1}mol^{-1}}$). However, the high symmetry of a TMS molecule (which decreases the number of distinct orientations) has to be taken into consideration along with the symmetry of the site [79]. If we further assume that the molecules sit on the surface with dipod-down orientation and they are disordered around the axis perpendicular to the surface, such disorder being actually found by neutron scattering to be discussed later, the number of equivalent orientations should be reduced to 6. This assumption gives us the transition entropy of $R \ln 6 = 14.9\ \mathrm{JK^{-1}mol^{-1}}$, being reasonably consistent with the experimental values.

It is interesting to note that the minimum value of the melting entropy was 0.7 $\mathrm{JK^{-1}mol^{-1}}$ at $\theta = 1.05$ (see Table 3.2), which is extremely small compared to the one obtained for the bulk α-phase (4.24 $\mathrm{JK^{-1}mol^{-1}}$) [9]. This may be attributed to the situation given for the 2-D melting at constant area of the monolayer capacity.

Fig. 4.3 displays the elastic intensity obtained from the neutron scattering at a momentum transfer $Q = 12.1\ \mathrm{nm^{-1}}$, where background has already been subtracted. As mentioned in Chapter 2, the spectrum consisted of an elastic component and quasielastic one. With increasing temperature, an increasing number of quasielastic events occur outside the elastic window. At a temperature where the correlation time τ of the molecular motion becomes comparable to the time equivalent to the energy width δE of resolution (i.e., $\tau/\hbar \sim 1/\delta E$), the elastic intensity starts to decrease. The energy resolution at $Q = 12.1\ \mathrm{nm^{-1}}$, $\delta E = 15\ \mu\mathrm{eV}$, corresponds to $\tau = 8.8 \times 10^{-11}$ s. A large decrease in intensity shown in Fig. 4.3 suggests motional disordering in the high-temperature phase of the TMS monolayer. Detailed discussion will be given in the later section.

As illustrated in Fig. 4.1, the phase boundary between the 2-D liquid and the 2-D fluid lies on a straight line at 202 K throughout the coverage $0 < \theta < 2$. This suggests that the 2-D fluid may be formed as a bilayer: the adsorbed molecules can easily be accommodated within the bilayer capacity. Coverage dependence of the entropy change associated with the transition from the 2-D liquid to the 2-D fluid (filled marks in Fig. 4.2) supports this idea. According to our simple picture, where the 2-D liquid forms islands on the surface whereas the 2-D fluid (or gas) is homogeneous, the configurational entropy [80] should tend to zero at $\theta = 1$ (dashed curve in Fig. 4.2). However, the experimental entropies actually vanish at $\theta = 2$, suggesting that there is a bilayer unit in the 2-D fluid. The smaller entropy than expected (dot-dashed curve in Fig. 4.2) can be explained either by the translational order remaining in the 2-D fluid or by the translational disorder already existing in the 2-D liquid. The latter would be probable.

TMS/MgO

Fig. 4.4 illustrates the incoherent elastic scattering intensity obtained on LAM–80ET. The large decrease in intensity around 100 K clearly demonstrates the existence of a 2-D solid-solid phase transition. The feature is exactly the same as observed for TMS/graphite discussed above.

4.1.2 Vibrational properties

The molar heat capacities of the TMS monolayer on graphite at $\theta = 0.609$ can be converted to the apparent characteristic temperatures in the framework of the 2-D Debye model, which is illustrated in Fig. 4.5. Here, we assume $2N$ degrees of freedom for the system. Also plotted in the figure are the 3-D Debye temperatures calculated from the experimental heat capacities for the bulk γ-phase [9], where we assume $3N$ degrees of freedom. It should be noted here that the ratio $\Theta_D(\text{2-D})/\Theta_D(\text{3-D})$ is approximately 0.6 at low temperatures. This can simply be understood from the dimensionality. According to the Debye theory [81], the cut-off frequency ω_D is represented by $\omega_D^3(\text{3-D})=6\pi^2 v^3 n(\text{3-D})$, where v is the sound velocity and $n(\text{3-D})$ is the volume density. Likewise, with the 2-D Debye model for the same media we obtain the relation $\omega_D^2(\text{2-D})=2\pi v^2 n(\text{2-D})$. Here we assume that the sound velocity is always constant without any polarization and the densities obtained from the $n(\text{2-D})$ and $n(\text{3-D})$ are the same. The ratio $\Theta_D(\text{2-D})/\Theta_D(\text{3-D}) = \omega_D(\text{2-D})/\omega_D(\text{3D})$ would therefore be $\sqrt{2\pi}/\sqrt[3]{6\pi^2}$, which is 0.64. The fact that it works pretty well with the TMS monolayer on graphite suggests that this monolayer is an ideal 2-D molecular solid in a sense that the medium is isotropic. The values of $\Theta_D(\text{2-D})$

obtained below 7 K for three different monolayers (TMS/graphite at θ = 0.609 and 1.81, and TMS/MgO at θ = 0.657) are summarized in Table 4.1. As discussed below, other contributions become significant at higher temperatures and the apparent Debye temperatures fall rapidly as illustrated in Fig. 4.5.

Table 4.1: Characteristic temperatures obtained from the low-temperature heat capacity of the monolayers for TMS/graphite and TMS/MgO. Those obtained for the bulk solid [9] are also listed for comparison. The $\Theta_{\mathrm{D}}^{\mathrm{lattice}}$ stands for the Debye characteristic temperature for lattice vibrations. The $\Theta_{\mathrm{E}}^{\mathrm{perp}}$ and $\Theta_{\mathrm{E}}^{\mathrm{lib}}$ stand for the Einstein temperature for vibrations perpendicular to the surface and librations, respectively.

System	$\Theta_{\mathrm{D}}^{\mathrm{lattice}}$ / K	$\Theta_{\mathrm{E}}^{\mathrm{perp}}$ / K	$\Theta_{\mathrm{E}}^{\mathrm{lib}}$ / K
TMS/graphite (θ = 0.609)	61	71	96
TMS/graphite (θ = 1.81)	59	58	105
TMS/MgO (θ = 0.657)	68	45	96
bulk TMS (γ-phase)	~ 100		105

There are two other modes that start to be excited before the contribution from the intramolecular vibrations become significant above 25 K; vibrations of the whole molecule perpendicular to the surface and rotational vibrations (librations). All the intramolecular vibrational modes are already assigned from a normal coordinate analysis as well as spectroscopic investigations [82]. Having subtracted this contribution with Einstein functions as well as the lattice contribution mentioned above, we fitted the rest of the heat capacities (below 30 K) with two functions, one being an Einstein function with $\Theta_{\mathrm{E}}(N)$ to describe the vibrations perpendicular to the surface and another Einstein function with $\Theta_{\mathrm{E}}(3N)$ to describe the librations. The former has N degrees of freedom and the latter $3N$. Here we ignore any possible anisotropic nature of the rotational vibrations. The fitted results are summarized in Table 4.1 and a typical result is illustrated in Fig. 4.6. It should be pointed out that the values of Θ_{E} obtained for the librational mode (96 K at θ = 0.609 and 105 K at θ = 1.81 for TMS/graphite and 96 K for TMS/MgO) are similar to that obtained for the bulk γ-phase, 105 K.

Fig. 4.7 illustrates the vibrational density of states obtained from the incoherent neutron scattering for TMS/graphite at θ = 1.02. The upper scale in Fig. 4.7(a) shows the corresponding temperature. It should be noted here that we investigate the system through the protons because proton has enormous cross section in the incoherent neutron scattering. Therefore, it is not straightforward to obtain the intrinsic density of states directly related to the heat capacity. Moreover, the polarization was not quite in the measurements and the orientation of the sample either. Different modes may contribute to the density of states with different weights. Nevertheless, the results clearly indicate the presence of two-dimensional lattice vibrations (below 5 meV), vibrations perpendicular to the surface (at 6 meV), and librations (at 9.5 meV). Some of the intramolecular vibrations, the torsional modes (ν_4 and ν_{44}) and the C-Si-C deformation vibrational modes (ν_{11} and ν_{43}), were also obtained at higher energies as illustrated in Fig. 4.7(b).

Vibrational properties of the monolayer were also obtained from the MD simulation. The velocity autocorrelation function was calculated from time evolution of the velocity of the molecular center-of-mass. The time-domain data were converted to the frequency-domain data by using Wiener-Khinchin relation, through the fast Fourier transformation. The spectra obtained along each axis are displayed in Fig. 4.8 (a), (b) and (c), respectively. The spectra of the in-plane motions broaden over below 10 meV. Although they show no apparent relation between E and $G(E)$, the existence of the distribution in $G(E)$ could be related to a dispersion in the 2-D lattice vibrations. On the other hand, the spectra along the Z-axis shows several peaks. We consider that one of them, presumably the one around 7 meV, is due to the molecular motions perpendicular to the surface, and the others might be attributed to the effect of vibrational motions of the graphite substrate to the molecular vibrations. In fact, it has been demonstrated that the spectrum of a single peak centered at 8 meV with a weak dispersion is obtained from TMS/graphite simulation when whole part of the graphite substrate is fixed in the position [83]. The effect of substrate motions to the out-of-plane vibrations of the admolecules has been pointed out in the early work on Ar/graphite system [22], where it has been demonstrated that the effect appears as a resonant coupling of monolayer film to out-of-plane collective motions of the graphite substrate. For our results obtained here (Fig. 4.8(c)), it is hard to see whether such resonance occurred or not. Furthermore, the fact that plural peaks have been obtained can not be explained at this stage. To discuss this subject in detail, further improvement for MD simulation is required.

4.1.3 Motional disordering

As described in the previous chapter, the neutron scattering spectra obtained at higher temperatures for the TMS monolayers on graphite ($\theta < 2$) show quasielastic scattering which consists of at least two components. To analyze such data quantitatively, we assume that the broad quasielastic component observed on LAM–40 is created by rotational motion of the admolecules and the narrow one observed on LAM–80ET created by the translationally diffusional motion of the admolecules. While several scattering laws for the particular molecular motions have been developed [76], we apply a Lorentzian function to describe each of the quasielastic components. We thus describe the scattering law for diffusive motion as

$$S(Q,\omega)_{\mathrm{tr}} = \frac{1}{\pi}\frac{\Gamma_{\mathrm{tr}}}{\Gamma_{\mathrm{tr}}^2 + \omega^2} \tag{4.1}$$

where Γ_{tr} is the half width at half maximum (hwhm) of the narrow component. We also describe the scattering laws for rotational motion as

$$S(Q,\omega)_{\mathrm{rot}} = F(Q)\delta(\omega) + \frac{1}{\pi}\frac{\Gamma_{\mathrm{rot}}}{\Gamma_{\mathrm{rot}}^2 + \omega^2} \tag{4.2}$$

where Γ_{rot} is the hwhm of the broad component and $F(Q)$ is the elastic incoherent structure factor (EISF). Assuming that these two modes are independent to each other, the total scattering law of this system can then be written as

$$S(Q,\omega)_{\mathrm{total}} = (1 - f_{\mathrm{m}})S(Q,\omega)_{\mathrm{rot}} + f_{\mathrm{m}}S(Q,\omega)_{\mathrm{rot}} \otimes S(Q,\omega)_{\mathrm{tr}} \tag{4.3}$$

where f_{m} is the fraction of the molecules that undergo translational diffusion, and the symbol $\otimes$ denotes a convolution product. With a high resolution spectrometer, such as LAM–80ET, the second term of the equation (4.2) is too broad to be observed because of the narrow energy window. We therefore ignore such term in (4.3) to have

$$S(Q,\omega) = (1 - f_{\mathrm{m}})F(Q)\delta(\omega) + f_{\mathrm{m}}\frac{F(Q)}{\pi}\frac{\Gamma_{\mathrm{tr}}}{\Gamma_{\mathrm{tr}}^2 + \omega^2} \tag{4.4}$$

To fit the data obtained on LAM–40, on the other hand, all the terms of (4.3) should be taken into account. As illustrated in Fig. 4.9–Fig. 4.14, the experimental data are well reproduced. Some of the results are represented in an Arrhenius plot, as illustrated in Fig. 4.15 for TMS/graphite at 1.0ML and in Fig. 4.16 for TMS/graphite at 1.5ML The correlation time that corresponds to Γ is also indicated in the right ordinate. The activation energies thus obtained for the translational

(E_a^{trans}) and rotational motions (E_a^{rot}) are summarized in Table 4.2. Those obtained from an NMR work [18] for the bulk plastic α-phase are also listed for comparison. It is interesting to note that the values at both coverages are significantly smaller than those for the bulk α-phase. It was argued that less stability of the orientationally-disordered phase of bulk TMS might be related to smaller value of the ratio E_a^{trans}/E_a^{rot} (3.7). The ratios obtained here (2.8 for 1.0ML and 2.3 for 1.5ML) are, however, even smaller. As shown previously, the orientationally-disordered phase of TMS/graphite is stable, which may be rationalized by the low-dimensionality of this system.

Table 4.2: Activation energies obtained from analyses of the neutron scattering spectra for TMS/graphite. Those obtained for the bulk plastic α-phase [18] are also listed for comparison. E_a^{trans} and E_a^{rot} stand for the activation energies of the translational motion and the rotational motion, respectively.

	1.0ML	1.5ML	bulk α-phase
E_a^{trans} / kJmol^{-1}	2.8	4.2	20.4
E_a^{rot} / kJmol^{-1}	1.0	1.8	5.5

When a broad quasielastic component broadens over the energy window of the spectrometer, as is the case for our spectra obtained on LAM–80ET, total scattering intensity of the spectrum obtained on the spectrometer is no longer conserved. This makes it hard to determine the EISF, i.e., $F(Q)$ in the equations, straightforwardly from the analyses described above. Furthermore, an existence of Debye-Waller factor complicate estimation of the EISF. For the low-temperature region phase, we found that the Debye-Waller factor could be represented as $\exp(-Q^2 \times 10^{-5} \times T)$, where Q is a momentum transfer (nm^{-1}). Here we assumed that $< u^2 >$ term in the Debye-Waller factor was proportional to the temperature, and the proportionality constant (10^{-5}) was estimated from the temperature dependence of the elastic intensity below 60 K. For the high-temperature phase, we could not deduce the factor by the same manner as for the low-temperature phase. Therefore, we applied the factor obtained for the low-temperature phase to the high temperature phase, although it should lead to an underestimate. This enables us to estimate the Q dependence of the EISF, which gives us geometric feature of the rotational motion. Fig. 4.17 presents the EISF obtained from the LAM–80ET data at T = 110.7, 120.7

and 140.5 K at $\theta = 1.04$. Some of the theoretical curves [76] are also presented; (1) isotropic rotation model (solid curve) with a gyration radius $r = 0.248$ nm, (2) uniaxial rotation model (dotted curve) averaged over preferred orientation of the substrate [54], (3) jump rotation model among 4 equivalent sites (dashed curve), and (4) jump rotation model among 8 site (dot-dashed curve). For the latter three models, we assumed that the TMS molecules sit on the surface with dipod-down orientation and they rotate around their two-fold axis that is perpendicular to the surface. According to Caliebe *et al.* [36], tetramethylgermane molecules actually form the solid monolayer on graphite with the dipod-down orientation in the low-temperature phase. As illustrated in Fig. 4.17, we can rule out the isotropic rotation model. However, it is not easy to distinguish other three models. The situation is the same for the monolayer at $\theta = 1.55$, as presented in Fig. 4.18. It should be noted here that estimated values of f_m are different between two coverages. At $\theta = 1.04$, f_m is 0.63 being constant while at $\theta = 1.55$ it changes from 0.35 (at 140.3 K) to 0.43 (at 149.6 K).

For the diffusional motion, we could not find any simple Q dependence like DQ^2 law both at $\theta = 1.04$ and at $\theta = 1.55$. The fact may suggest some jump diffusional motion among the lattice sites. If that is the case, a simple model enables us to estimate the mean residence time τ by assuming a one-dimensional periodic potential [84] with $d = 0.651$ nm for the $\sqrt{7} \times \sqrt{7}R19°$ lattice. The values thus obtained are 2×10^{-11} s at 120.7 K and 9×10^{-12} s at 160.1 K which are not far from those obtained in Fig. 4.15.

As described above, we attributed the narrow quasielastic component to the translational diffusion and the broad one to the rotational motion. Validity of the assignment was examined from the MD simulation. Fig. 4.19 displays the mean-square displacement of the TMS molecules on graphite calculated from the MD simulation at $\theta = 0.724$ at $T = 140$ K. According to the Einstein relation, the self-diffusion coefficient can be calculated by

$$D = \frac{1}{4N} \lim_{t \to \infty} \frac{\mathrm{d}}{\mathrm{d}t} \left\langle \sum_{i}^{N} [\mathbf{r}_i(t) - \mathbf{r}_i(0)]^2 \right\rangle \tag{4.5}$$

where N is the number of molecules. Because only the displacement parallel to the surface was took into account, a factor 4 is substituted in the denominator for the usual value of 6. The value thus obtained are $D = 5 \times 10^{-10}$ m^{2}s^{-1} for the monolayer at $\theta = 0.724$ and $D = 3 \times 10^{-10}$ m^{2}s^{-1} for the one at $\theta = 1.40$. This calculation is based on Fick's law and hence obtained values can be related to DQ^2 law in the manner of quasielastic neutron scattering. Corresponding τ are therefore obtained using $Q = 11$ nm^{-1}, which are listed in Table 4.1.3. Also listed in Table 4.1.3

are the correlation times obtained from neutron scattering at $Q = 11\ \mathrm{nm}^{-1}$ at $T = 140.5$ K for 1ML and $T = 149.6$ K for 1.5ML. It clearly indicates that these values are comparable to each other at each coverage. In general, correlation time for self diffusion in the bulk plastic phase is

θ	τ/s	
	MD	Neutron
1ML	2.1×10^{-11}	2.0×10^{-11}
1.5ML	1.9×10^{-11}	3.0×10^{-11}

$\sim 10^{-7}$ s just below the melting point, and jumps to $\sim 10^{-11}$ s just above the melting point [2]. The correlation times for the monolayers obtained here demonstrate that the mobility in the monolayers is as high as the bulk liquid.

The results obtained for TMS/MgO are illustrated in an Arrhenius plot (Fig. 4.20). Although quite similar feature was found as to the temperature variation of the elastic intensity, the correlation time obtained from the narrow quasielastic component is 1.4×10^{-10} s (at 120 K and $Q = 12.1\ \mathrm{nm}^{-1}$), which is an order of magnitude slower than that obtained for TMS/graphite at $\theta = 1.04$ (1.7×10^{-11} s). Moreover, the activation energy obtained at $Q = 12.1\ \mathrm{nm}^{-1}$ (5.6 kJmol^{-1}) is twice as large as that for TMS/graphite at $\theta = 1.04$ (2.8 kJmol^{-1}). It is evident that the TMS molecules are less mobile on MgO than on the graphite surface.

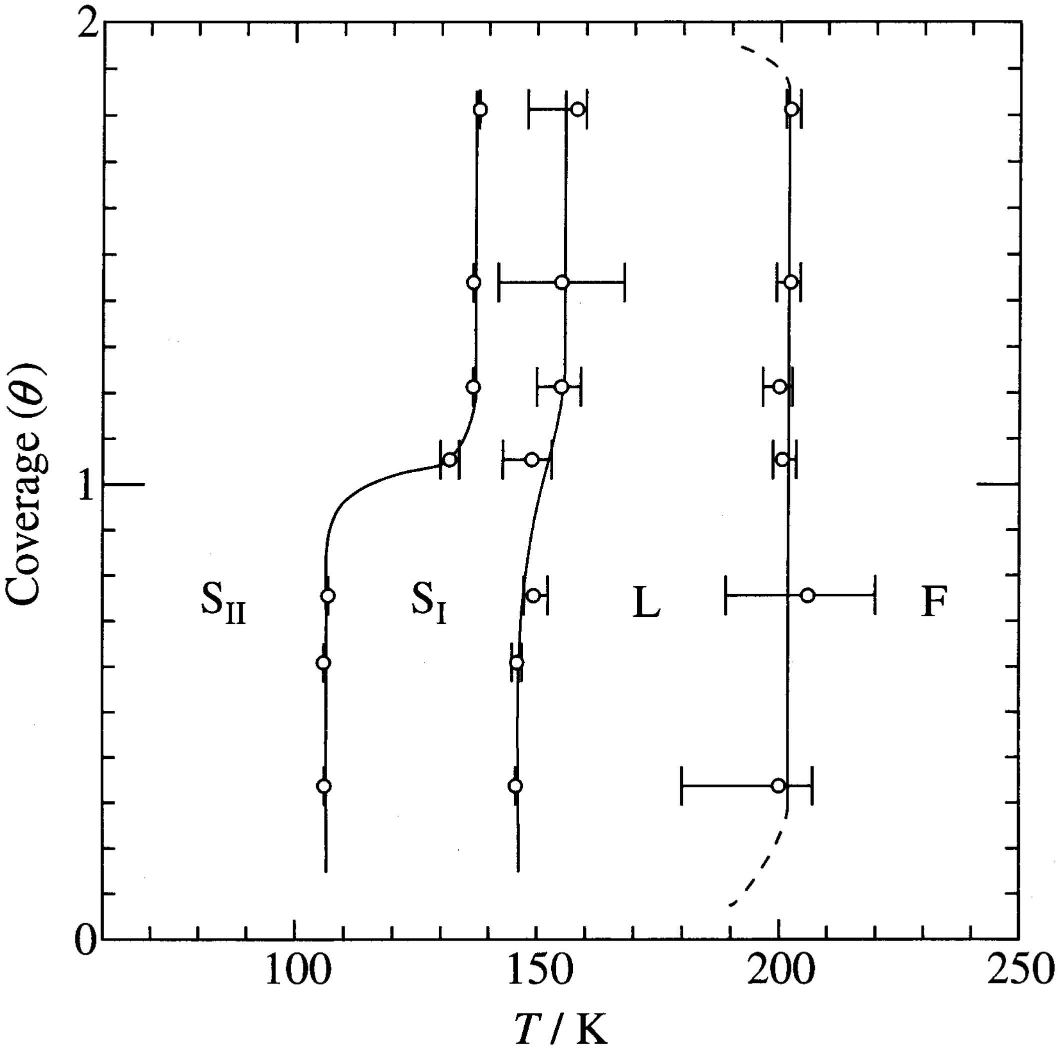

Fig. 4.1: Phase diagram of TMS on graphite at $\theta < 2$. The temperatures of the peak in heat capacity are plotted. The full-width-at-half-maximum of each anomaly is also presented. S_I, S_{II}, L and F stand for the 2-D solid I, the 2-D solid II, the 2-D liquid and the 2-D fluid, respectively.

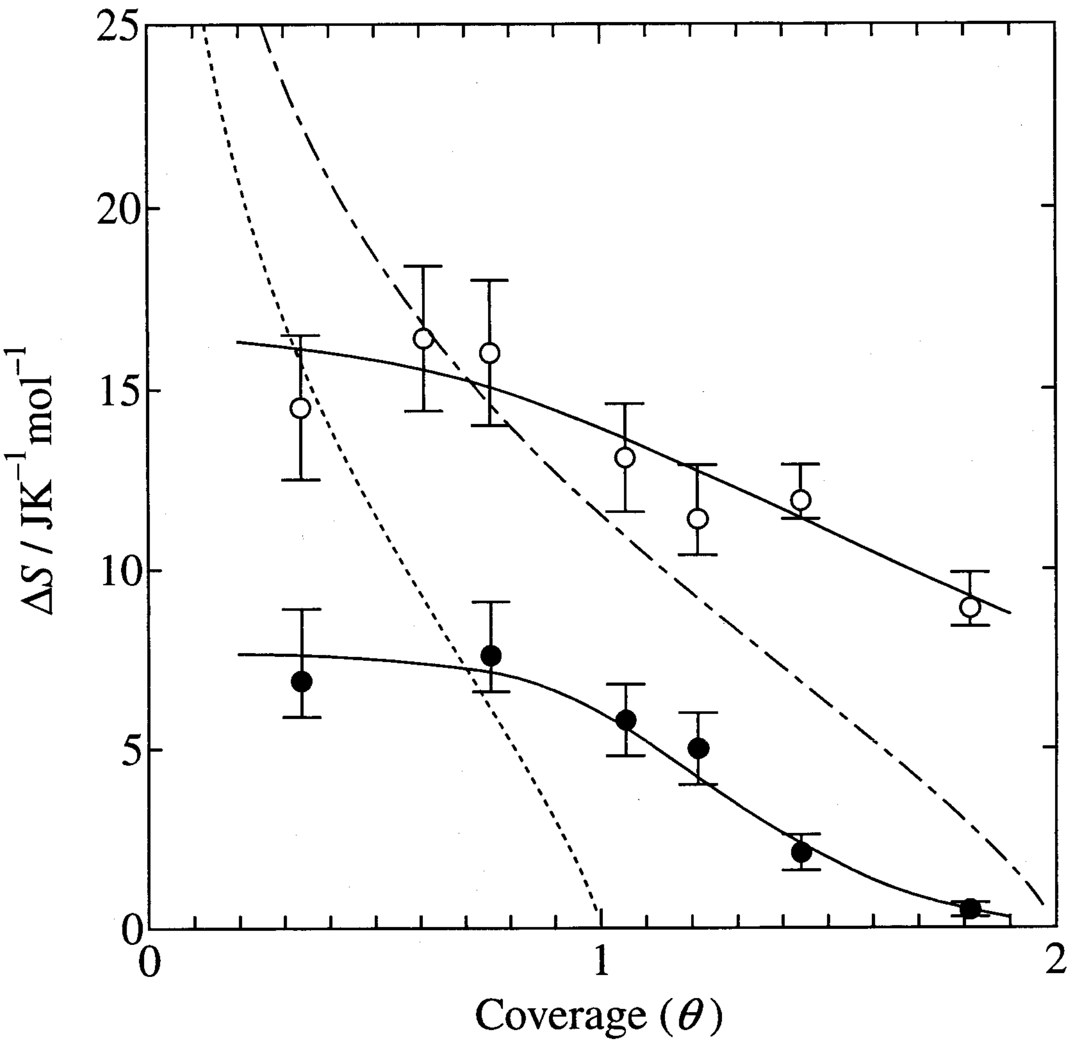

Fig. 4.2: Experimental and theoretical entropies; the entropy change associated with the 2-D solid transition from the measurement (open marks), the entropy change associated with the transition from the 2-D liquid to the 2-D fluid from the measurement (filled marks), the configurational entropy calculated from the monolayer capacity (broken curve), and the configurational entropy calculated from the bilayer capacity (dot-dashed curve). An estimated accuracy is given by the vertical bars.

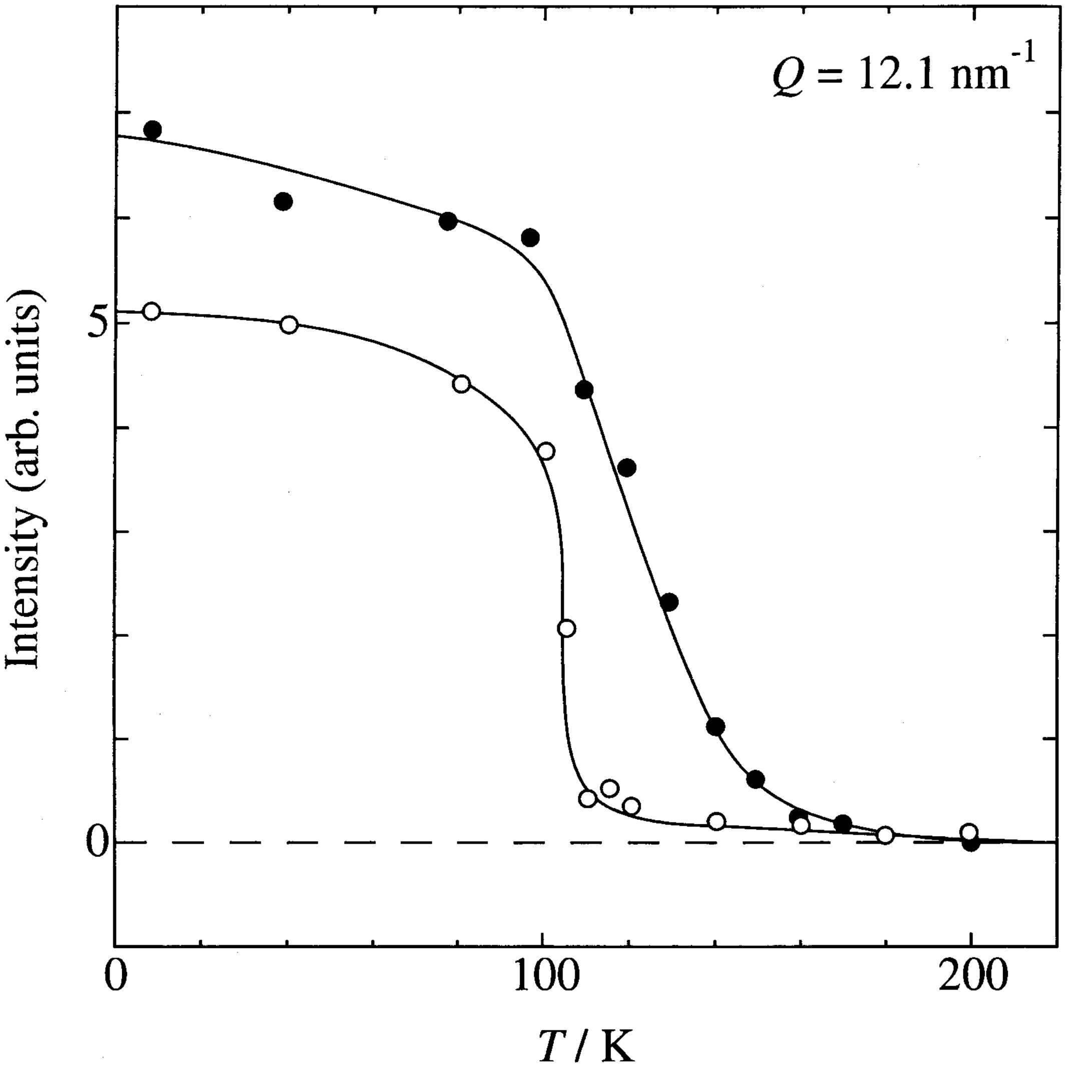

Fig. 4.3: Incoherent elastic neutron scattering intensity as a function of temperature for TMS on graphite obtained on LAM–80ET; θ = 1.04 (open circles), θ = 1.55 (filled circles). The background has already been subtracted.

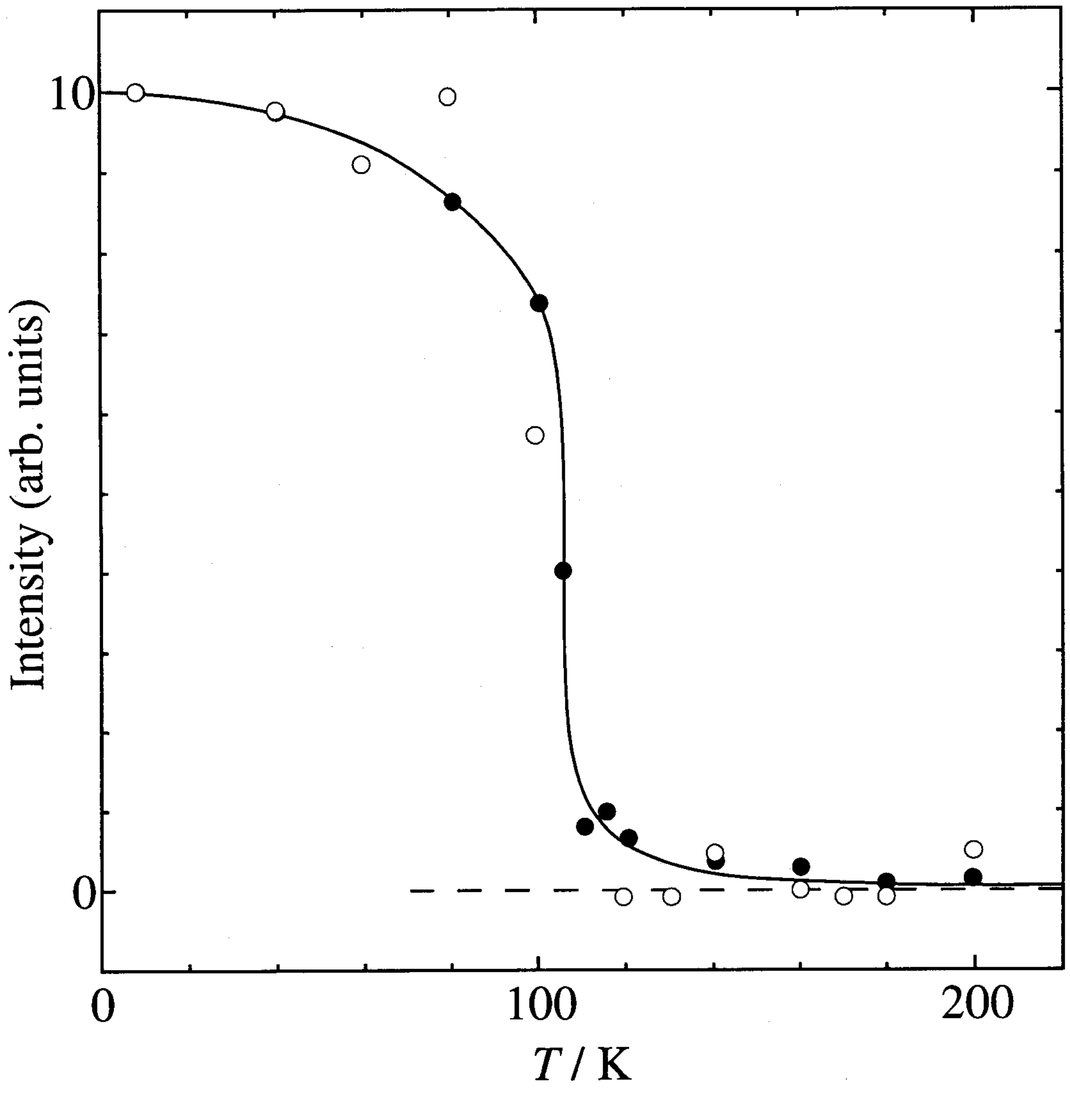

Fig. 4.4: Incoherent elastic neutron scattering intensity as a function of temperature obtained on LAM–80ET at Q = 12.1 nm^{-1} for TMS/MgO (open circles). The results obtained for TMS/graphite are also plotted (filled circles).

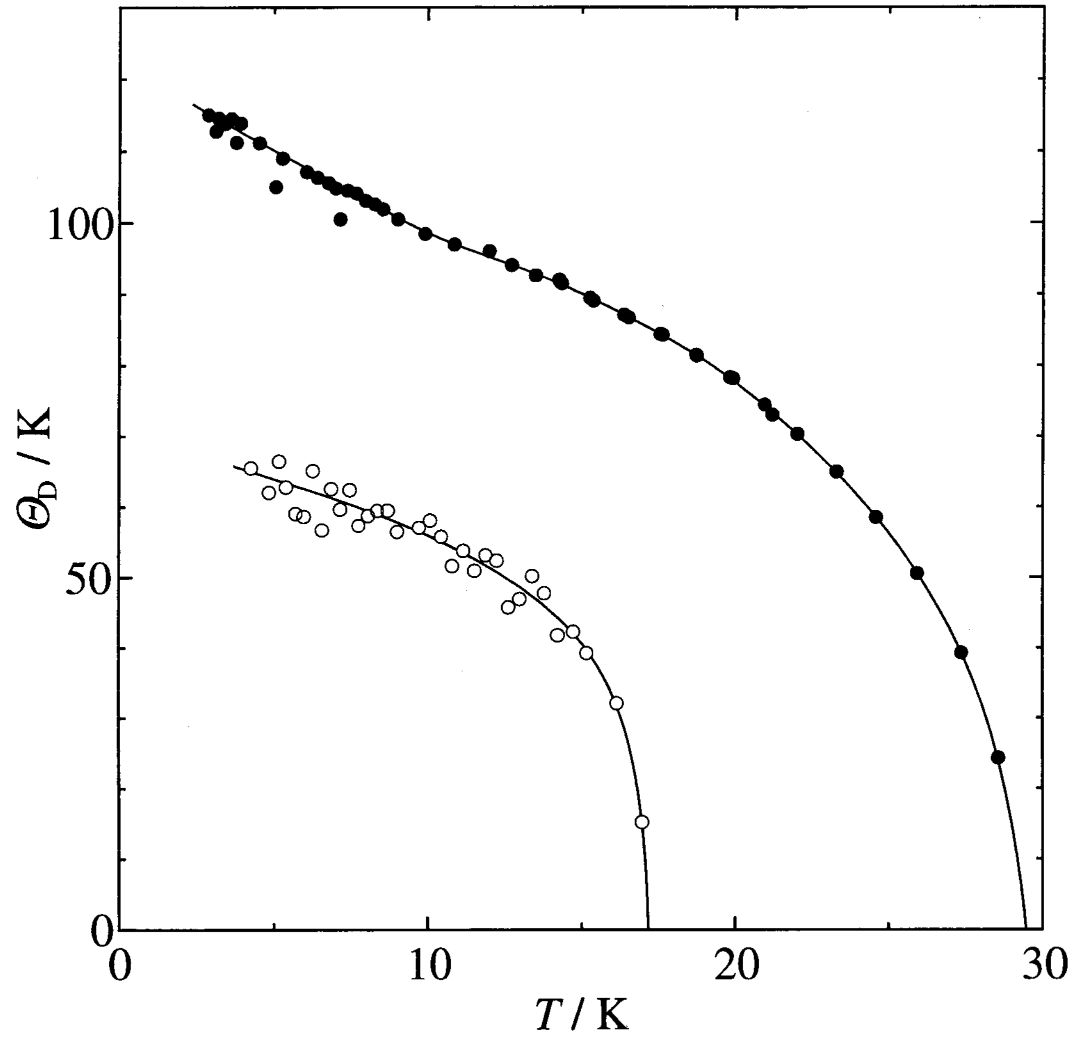

Fig. 4.5: Apparent Debye temperatures obtained from the experimental heat capacities for the TMS monolayer on graphite at θ = 0.609 (open circles) and for the bulk solid (filled circles). Here, the 2-D and 3-D Debye models are applied respectively to obtain the characteristic temperatures.

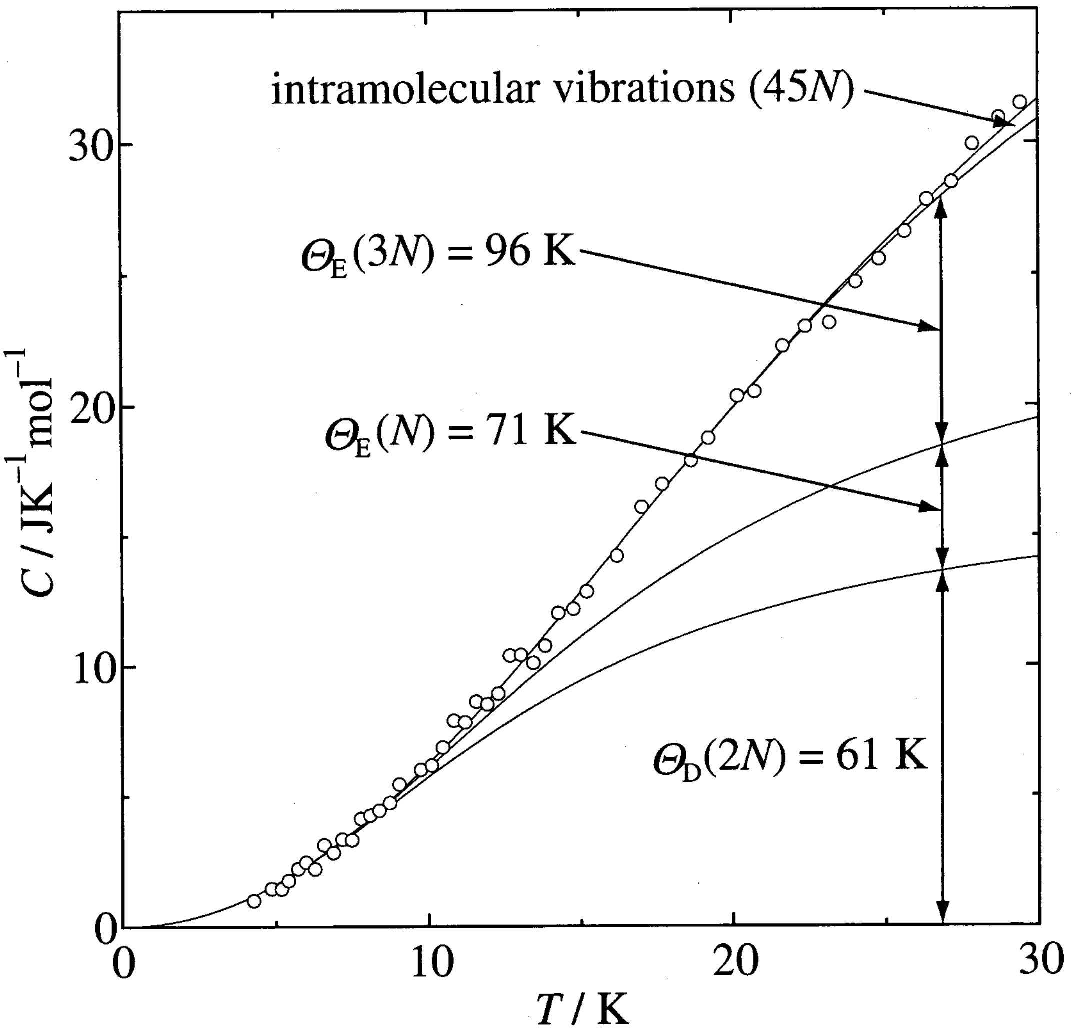

Fig. 4.6: Breakdown of the experimental heat capacities obtained for the TMS monolayer on graphite. See the details in the text.

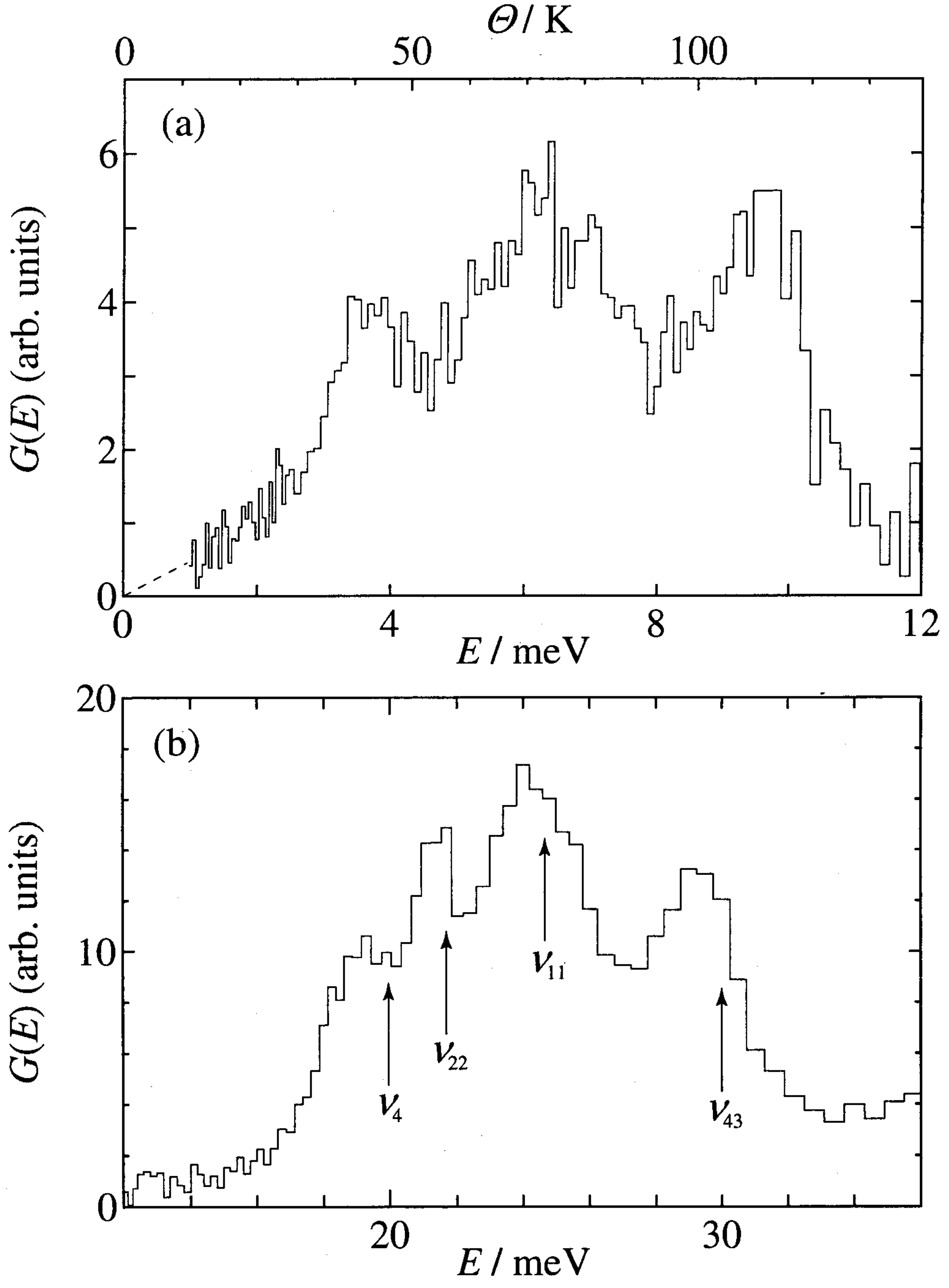

Fig. 4.7: Vibrational density of states obtained by neutron scattering for TMS/graphite at θ = 1.02. (a) Lattice vibrational modes appeared in the low-energy region. The corresponding temperature is given in the upper scale. (b) Some of the intramolecular vibrations appeared in the higher energy region. The ν_4 and ν_{22} are the torsional modes, whereas the modes ν_{11} and ν_{43} are due to the C-Si-C deformation vibrations [82]. See the details in the text.

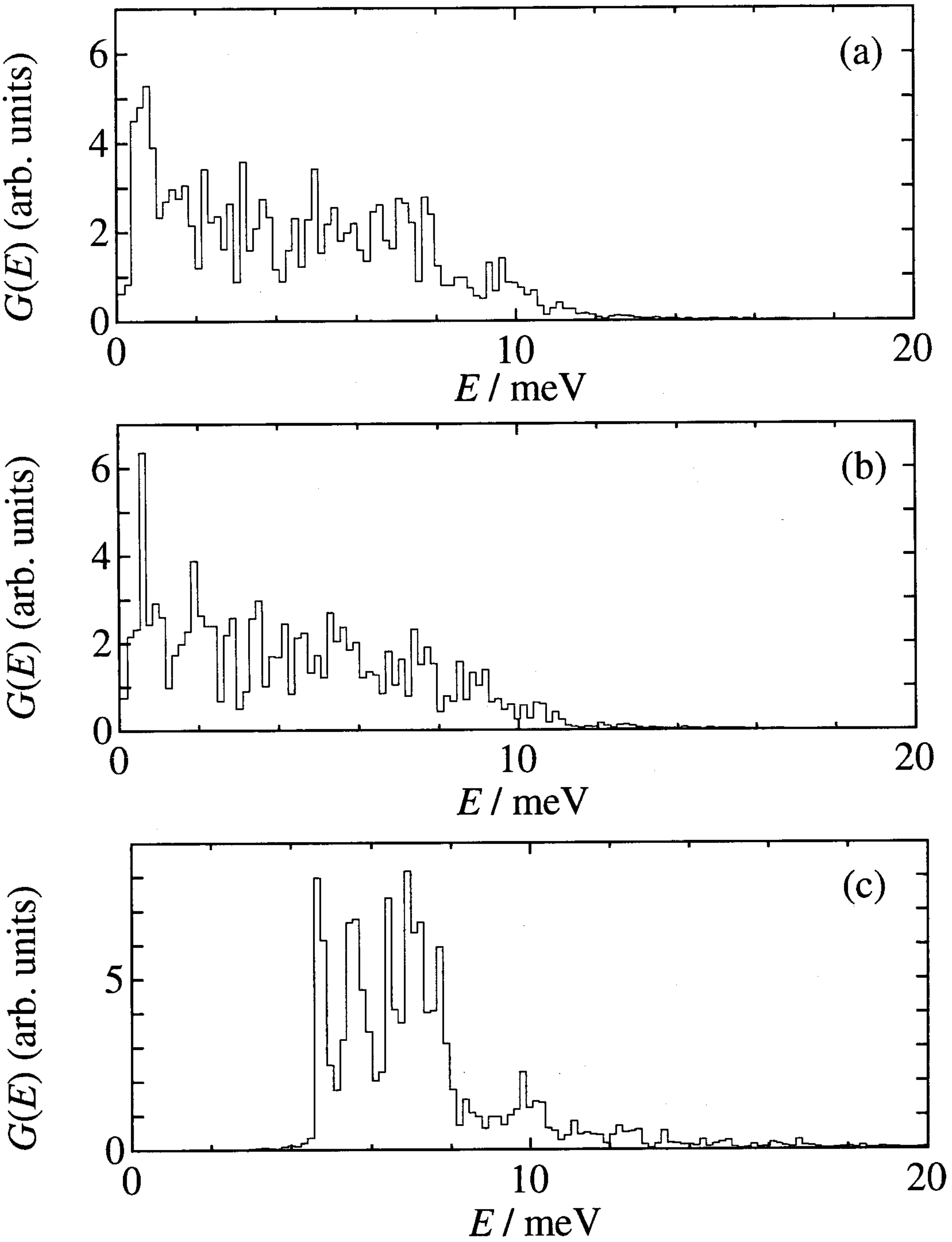

Fig. 4.8: Vibrational spectra obtained by an MD simulation for TMS/graphite at $\theta = 0.724$. The vibrational density of states obtained along the in-plane X-axis (a), the Y-axis (b) and the axis perpendicular to the graphite surface (c).

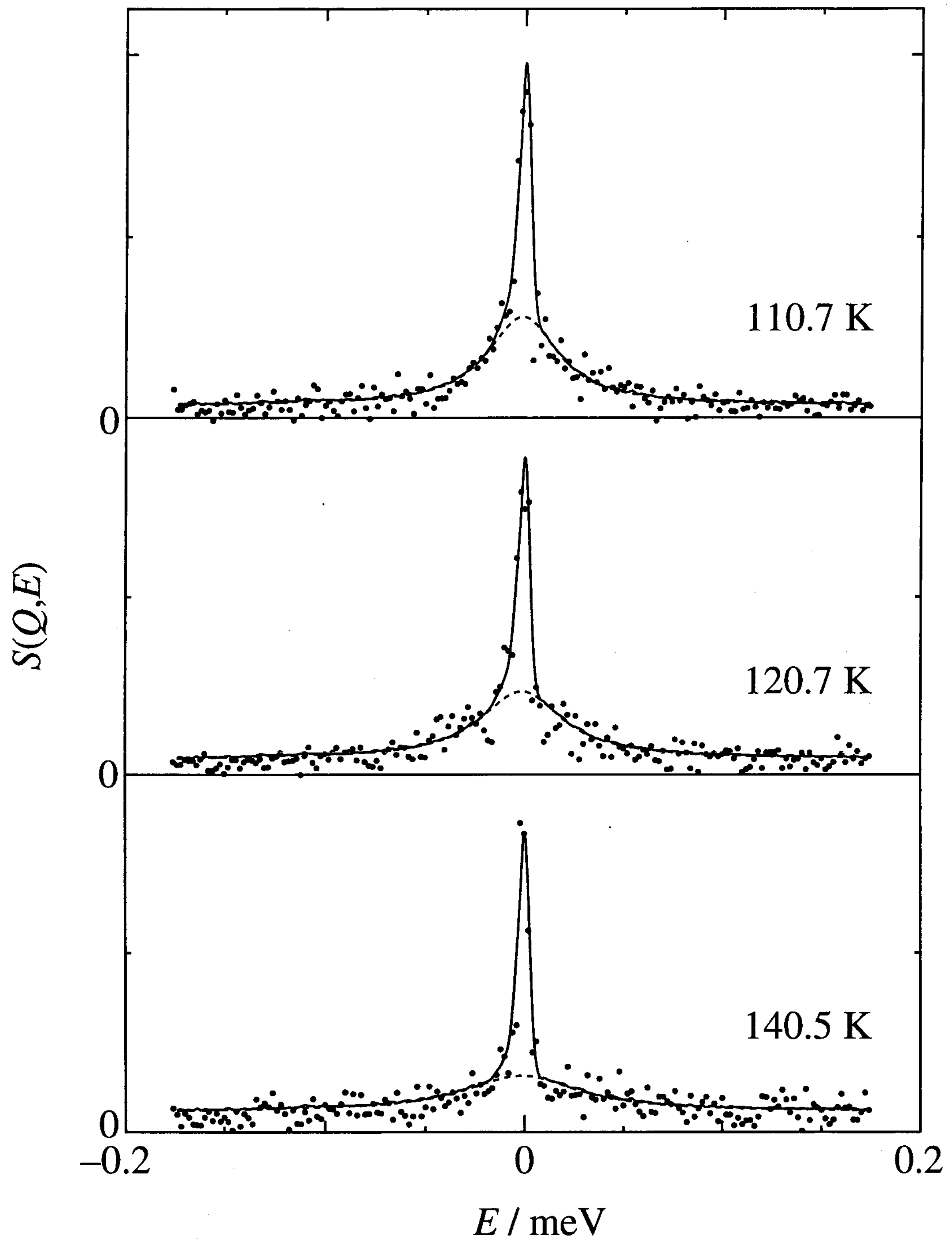

Fig. 4.9: Spectra obtained on LAM–80ET at Q = 8.1 nm^{-1} for TMS/graphite at θ = 1.04. The solid curves show the best fit and the dashed curves show the Lorentzian components convoluted with the resolution function.

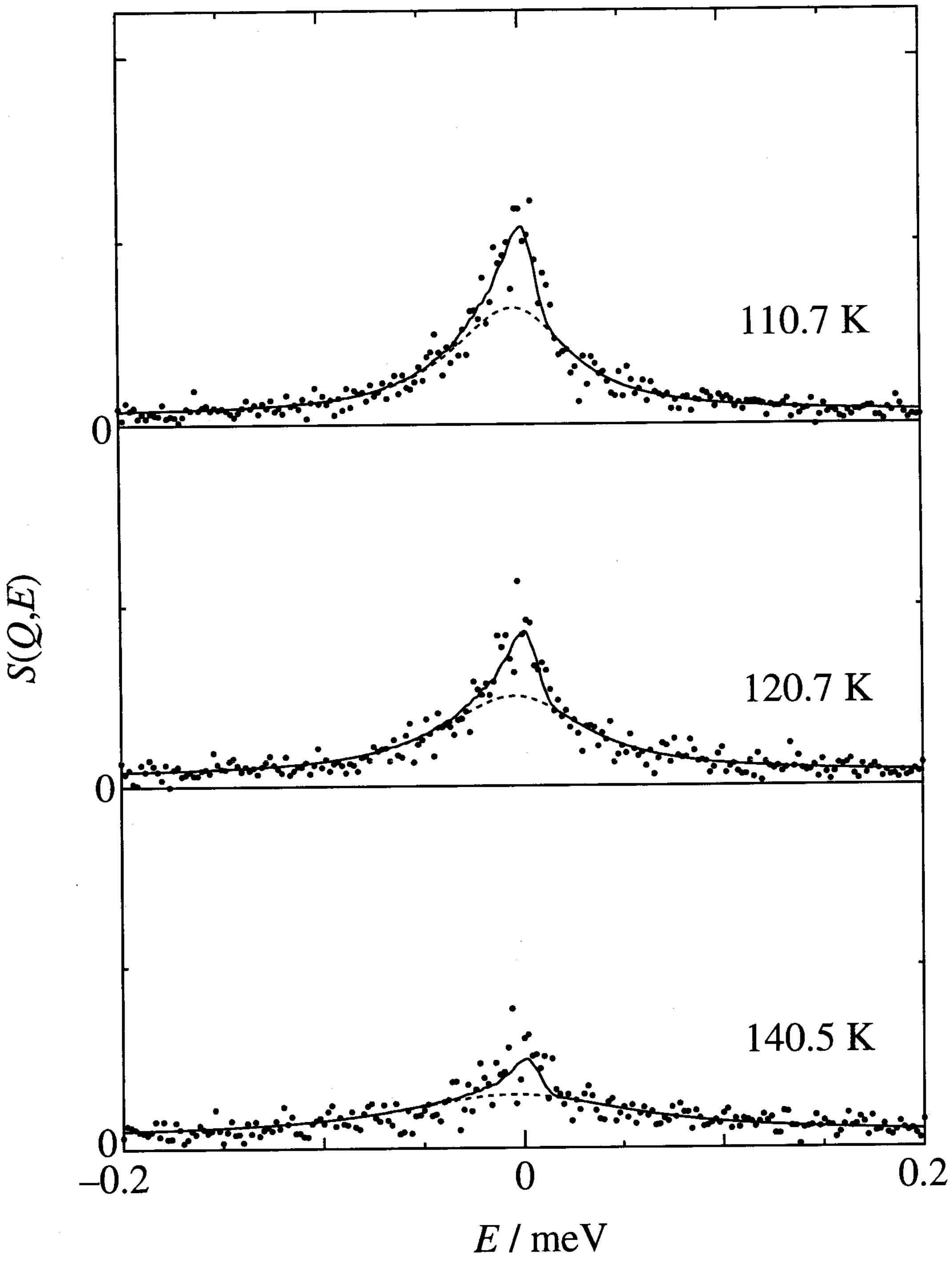

Fig. 4.10: Spectra obtained on LAM–80ET at Q = 12.1 nm^{-1} for TMS/graphite at θ = 1.04. The solid curves show the best fit and the dashed curves show the Lorentzian components convoluted with the resolution function.

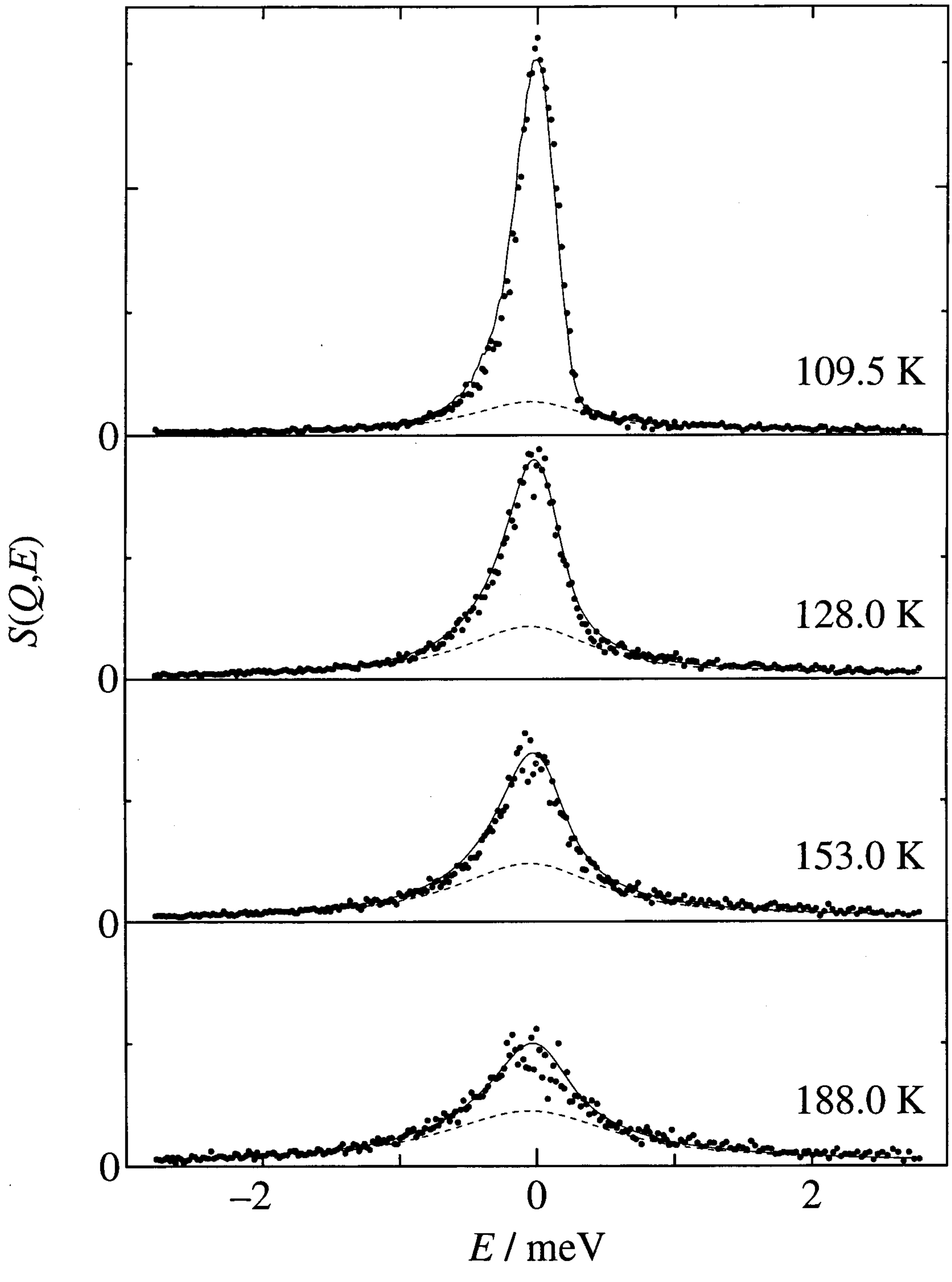

Fig. 4.11: Spectra obtained on LAM–40 at Q = 14.0 nm^{-1} for TMS/graphite at θ = 1.02. The solid curves show the best fit and the dashed curves show the convoluted contribution from the broad component of quasielastic scattering.

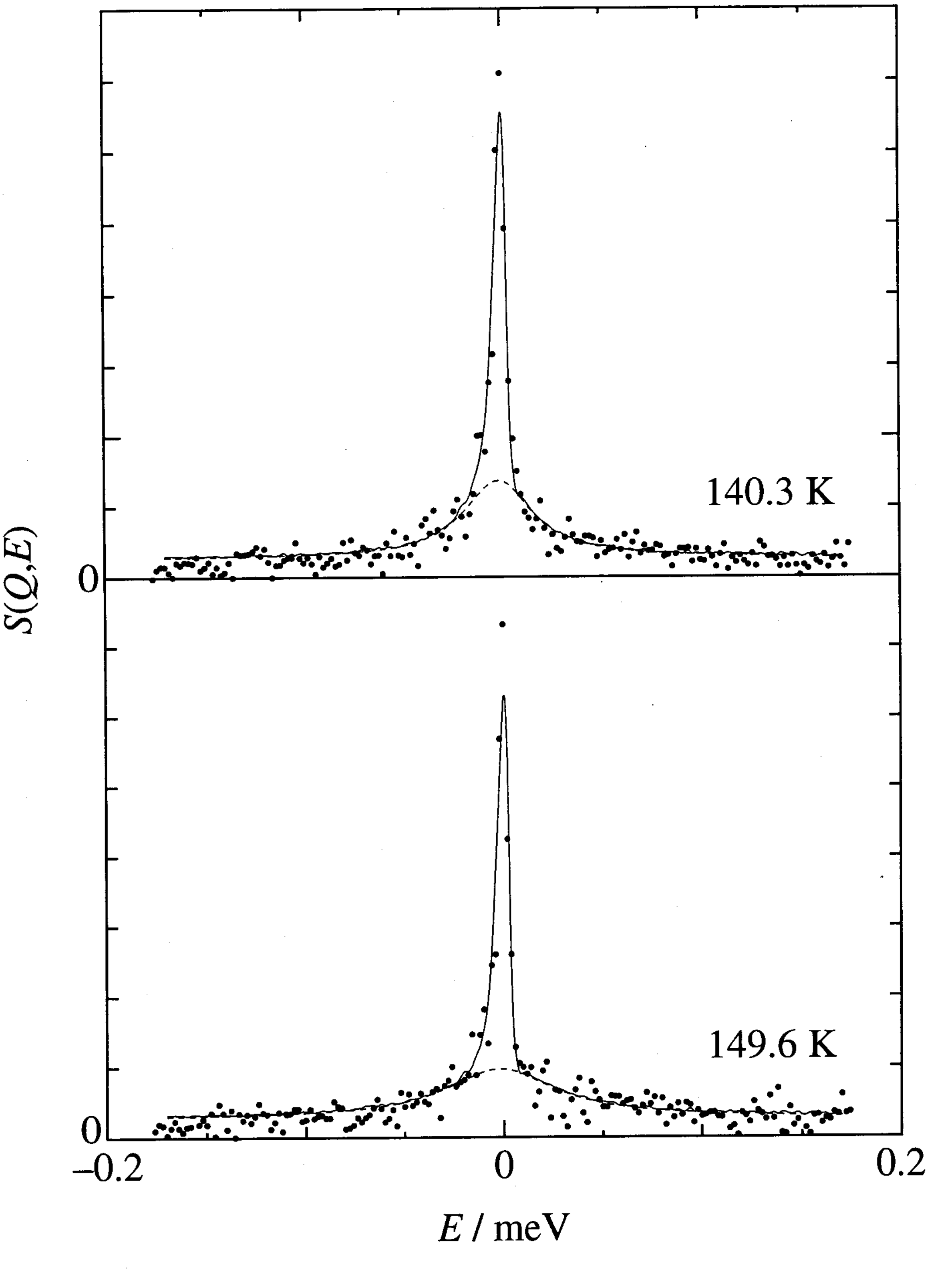

Fig. 4.12: Spectra obtained on LAM–80ET at Q = 8.1 nm^{-1} for TMS/graphite at θ = 1.55. The solid curves show the best fit and the dashed curves show the Lorentzian components convoluted with the resolution function.

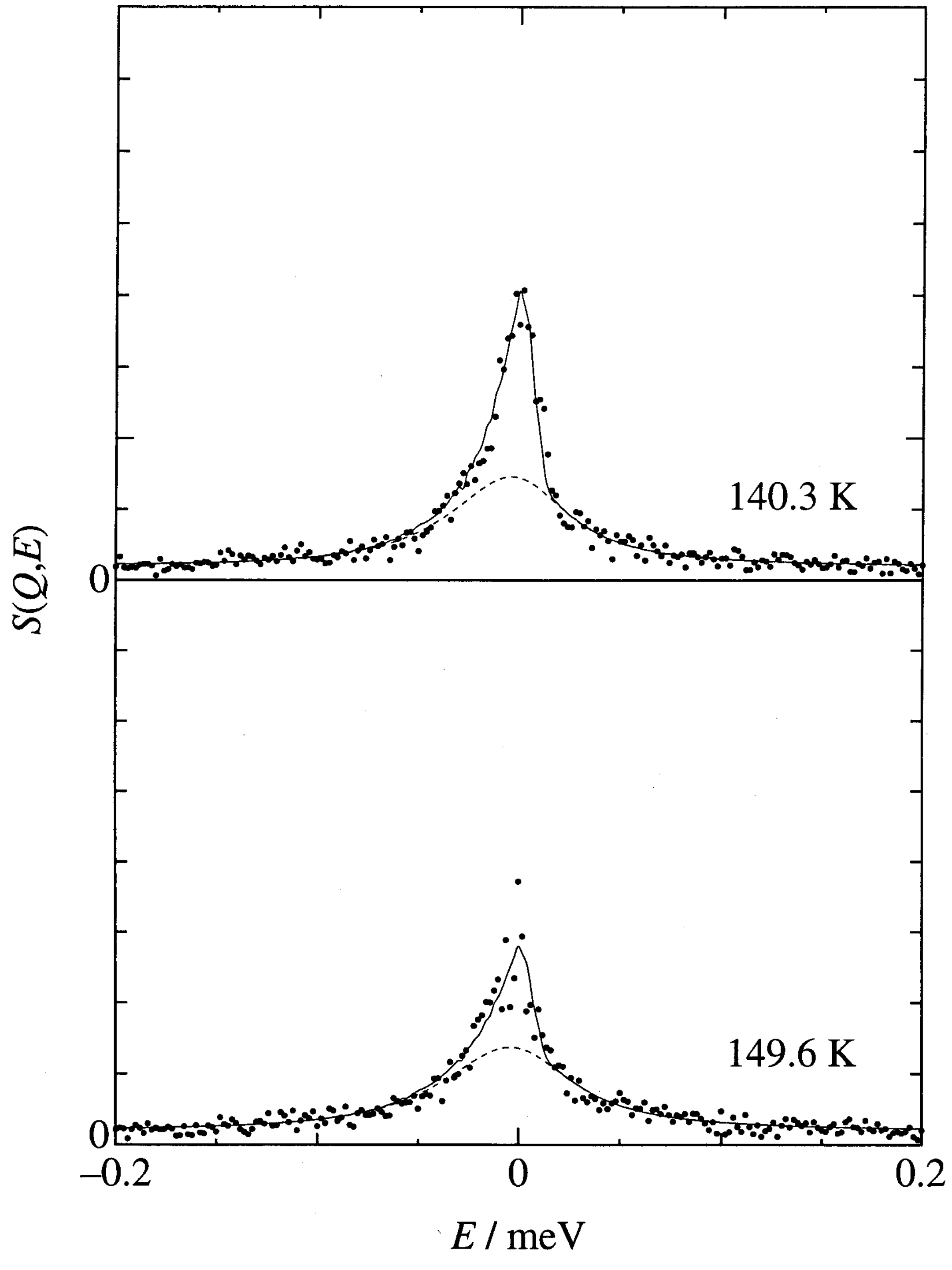

Fig. 4.13: Spectra obtained on LAM–80ET at $Q = 12.1\ \mathrm{nm}^{-1}$ for TMS/graphite at $\theta = 1.55$. The solid curves show the best fit and the dashed curves show the Lorentzian components convoluted with the resolution function.

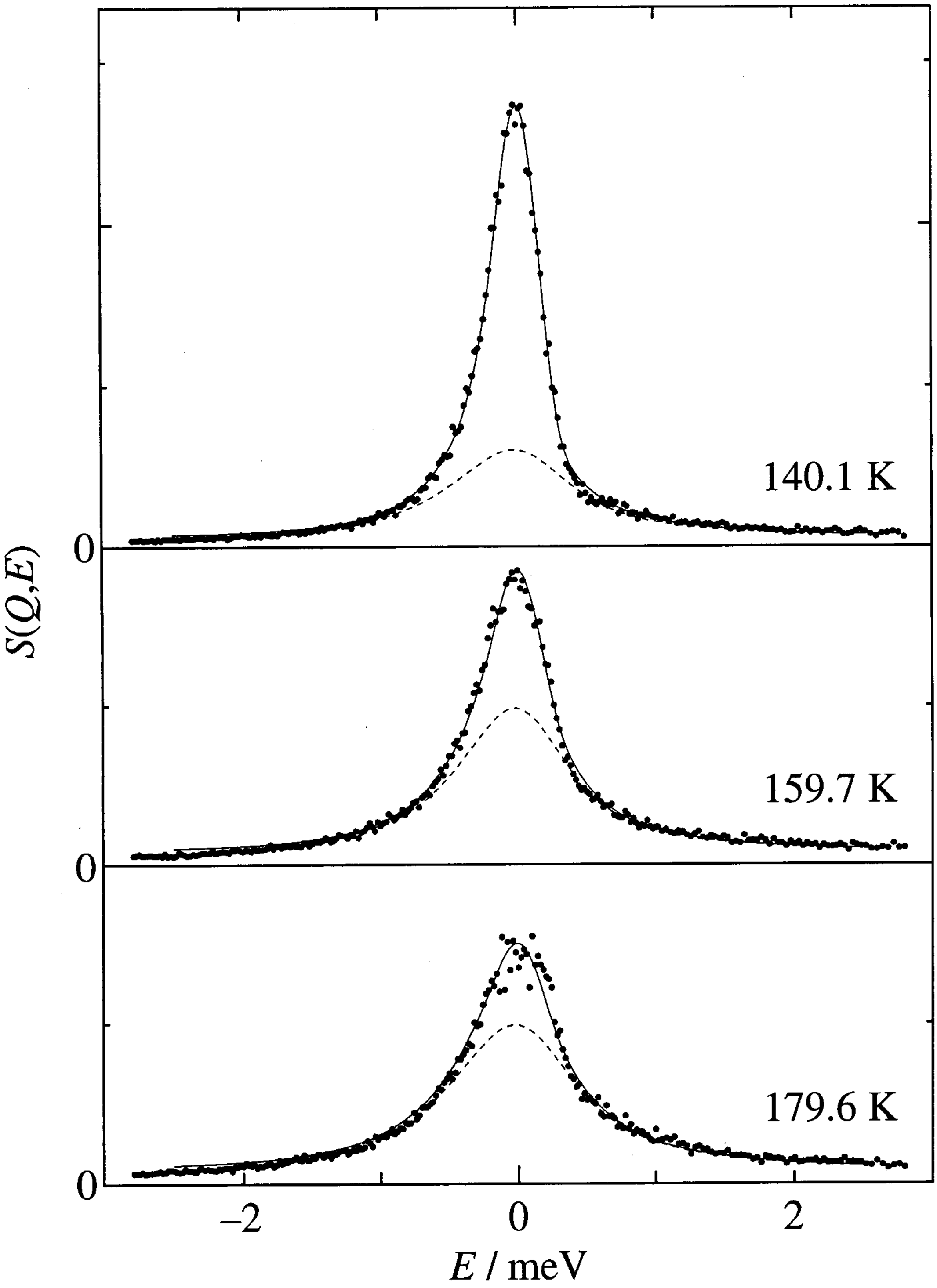

Fig. 4.14: Spectra obtained on LAM–40 at Q = 14.0 nm^{-1} for TMS/graphite at θ = 1.54. The solid curves show the best fit and the dashed curves show the convoluted contribution from the broad component of quasielastic scattering.

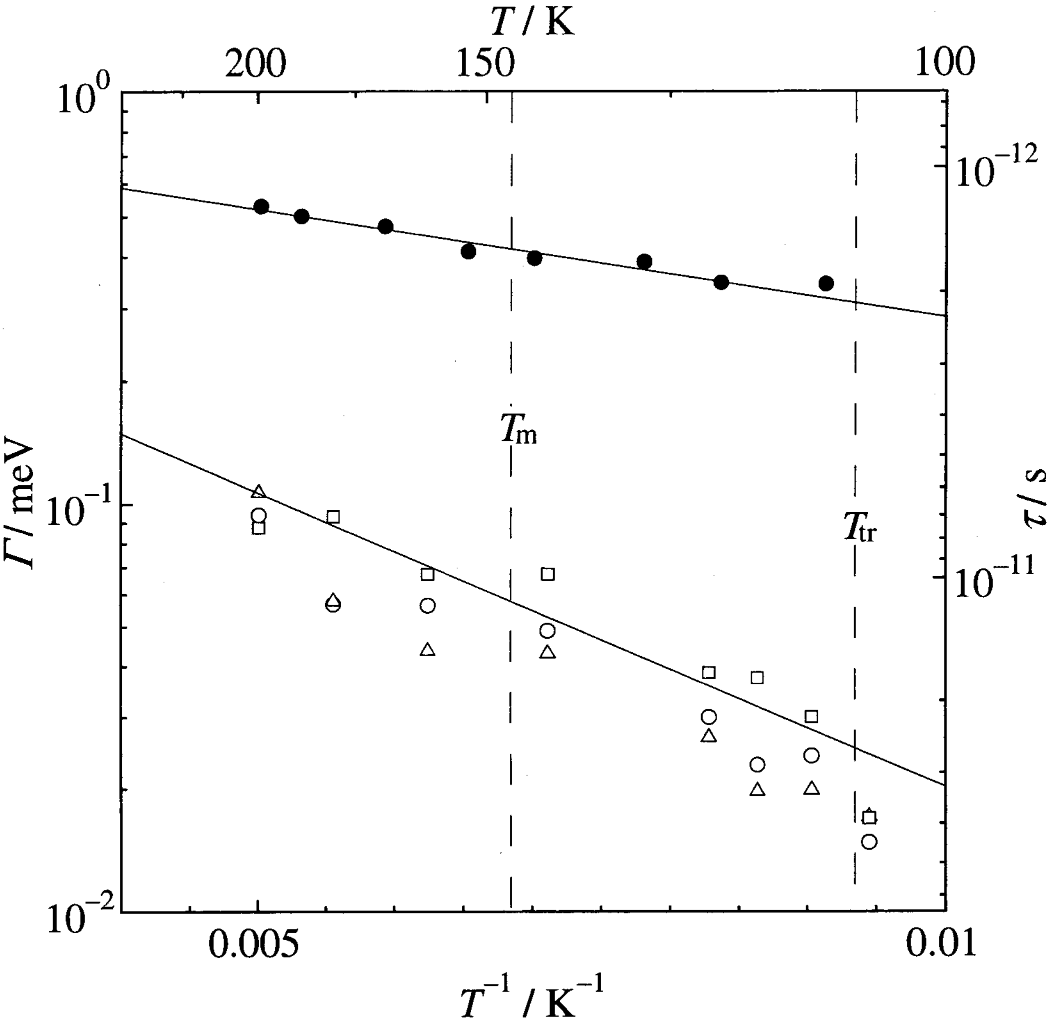

Fig. 4.15: An Arrhenius plot obtained for TMS/graphite at $\theta = 1.04$ from the hwhm of the Lorentzian component. The corresponding correlation time is also indicated. The narrow component (open marks) was extracted from the LAM–80ET data at $Q = 8.1\ \mathrm{nm}^{-1}$ (open circles), $11.0\ \mathrm{nm}^{-1}$ (triangles) and $12.1\ \mathrm{nm}^{-1}$ (squares). Having such analyses, the broad component was extracted from the LAM–40 data at $Q = 14.0\ \mathrm{nm}^{-1}$ (filled circles).

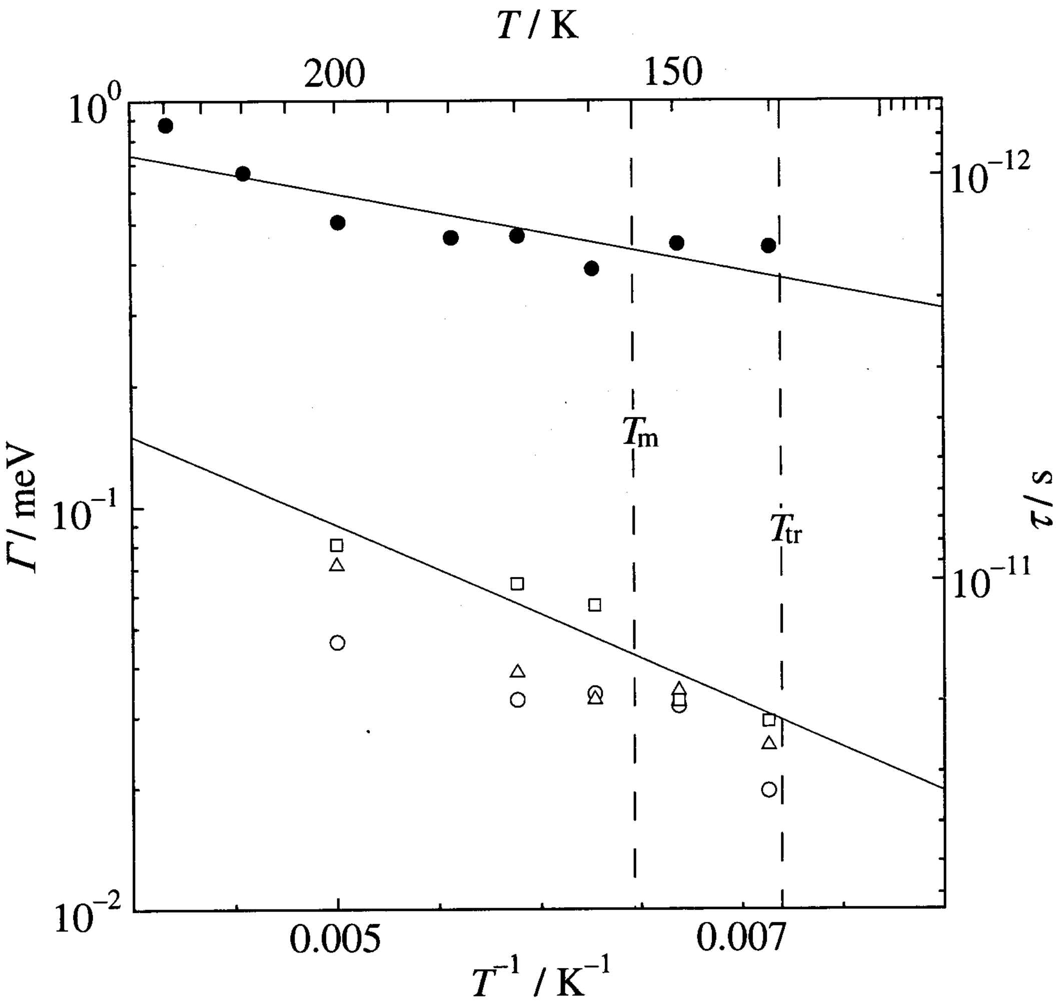

Fig. 4.16: An Arrhenius plot obtained for TMS/graphite at θ = 1.55 from the hwhm of the Lorentzian component. The corresponding correlation time is also indicated. The narrow component (open marks) was extracted from the LAM–80ET data at Q = 8.1 nm^{-1} (open circles), 11.0 nm^{-1} (triangles) and 12.1 nm^{-1} (squares). Having such analyses, the broad component was extracted from the LAM–40 data at Q = 14.0 nm^{-1} (filled circles).

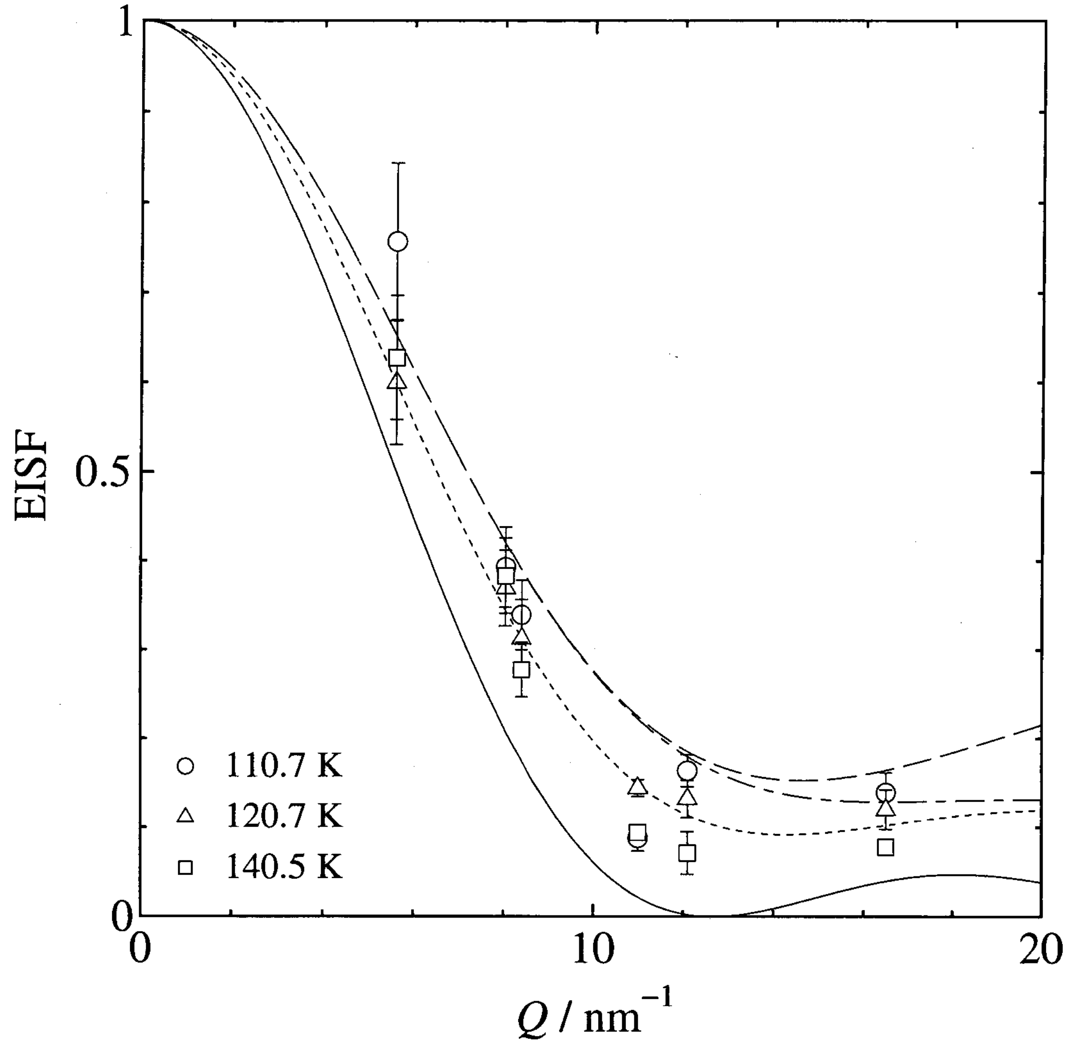

Fig. 4.17: EISF obtained at three temperatures in the orientationally-disordered 2-D solid phase for TMS/graphite at θ = 1.04. The theoretical curves are also indicated; isotropic rotation model (solid curve), uniaxial rotation model (dotted curve), 4-sites jump rotation model (dashed curve), and 8-sites jump rotation model (dot-dashed curve).

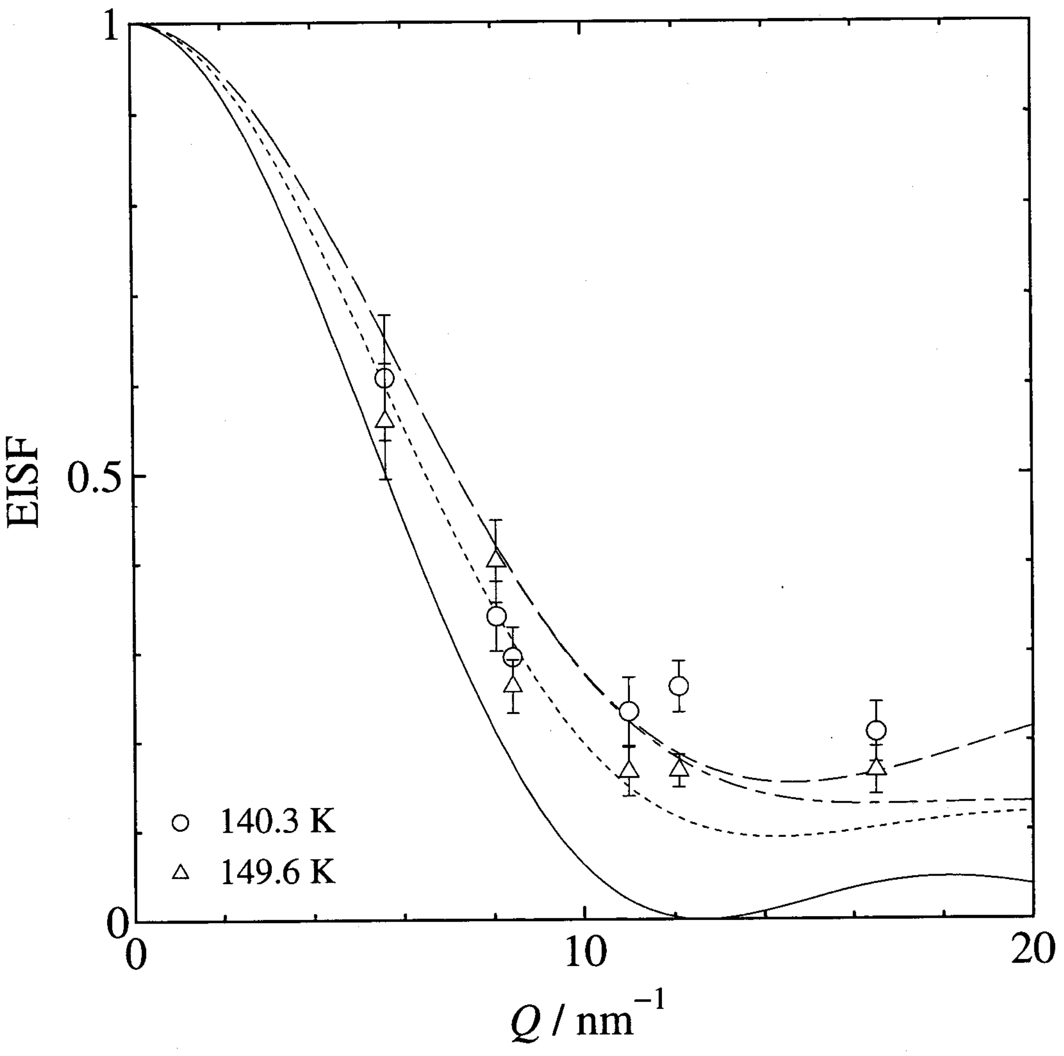

Fig. 4.18: EISF obtained at three temperatures in the orientationally-disordered 2-D solid phase for TMS/graphite at θ = 1.55. The theoretical curves are the same as in Fig 4.17.

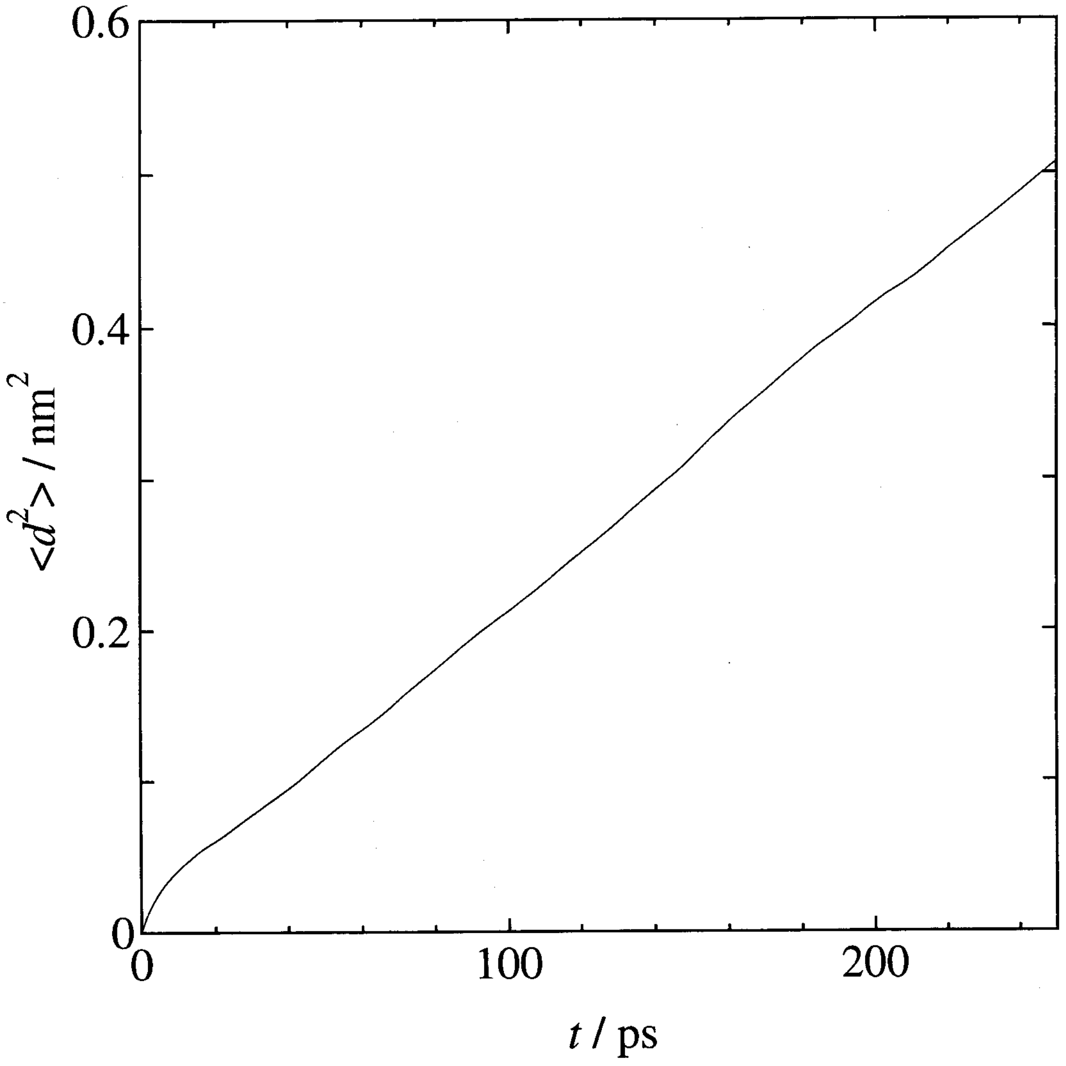

Fig. 4.19: In-plane mean-square displacement of the TMS molecules on graphite obtained from MD simulation at $\theta = 0.724$ at $T = 140$ K.

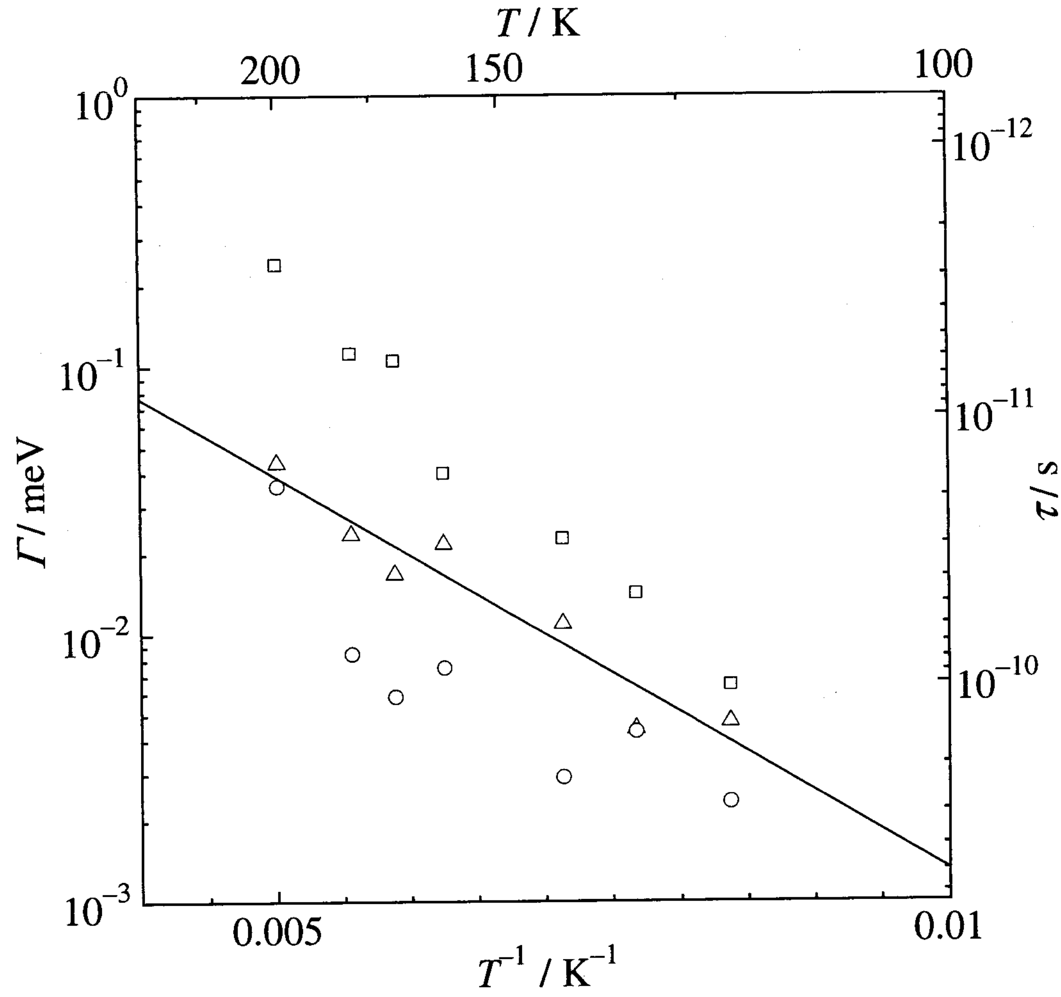

Fig. 4.20: An Arrhenius plot obtained for TMS/MgO from the hwhm of the Lorentzian component. The corresponding correlation time is also indicated. The results were obtained from the LAM–80ET data at Q = 8.4 nm^{-1} (circles), 12.1 nm^{-1} (triangles) and 16.5 nm^{-1} (squares).

4.2 Bulk phases and the monolayer at the solid–liquid interface ($\theta > 2$)

4.2.1 Phase behavior

As described in previous chapter, the heat-capacity anomalies were observed at the temperatures corresponding to each of the melting points for the bulk solid phases (α, βand γ-phase), although the anomalies were broad. We also pointed out in the previous chapter that the system appeared to be in the stable equilibrium. We thus consider that the bulk solid phases formed on graphite coexist at equilibrium and each of them melts at the same temperature as the *ordinary* bulk solid. Accordingly, the magnitude of the entropy changes associated with each anomaly directly reflect the amount of each solid phase. The amount ratio of each solid phase to the total adsorbate was calculated either from the entropy values associated with the melting of each bulk phase or from the entropy associated with the phase transition of the monolayer formed at the gas–solid interface (at $\theta < 5$). Here, the melting entropy of each bulk phase was based on the reported values for the *ordinary* bulk solid [9], and the transition entropy of the monolayer at the gas-solid interface was based on the value for the monolayer at $\theta = 1.81$ (8.9 $\mathrm{JK^{-1}mol^{-1}}$). The ratios calculated are summarized in Table 4.3 for representative results listed in Table 3.7. It should be noted here that the sum of the ratios for the bulk phase is nearly equal to the value that should be, i.e., $(\theta - 2)/\theta$ where 2 is attributed to the monolayer formed at either the gas–graphite or the graphite–liquid interface. This fact also suggests that all of the system is at equilibrium at all times.

Fig. 4.21 displays the elastic intensity for TMS on graphite at $\theta = 3.04$ obtained on LAM–80ET at a momentum transfer $Q = 11.0\ \mathrm{nm^{-1}}$. At this coverage, three solid phases are dominant; the monolayer formed at the gas–graphite interface, the one formed at the liquid-graphite interface and the bulk α-phase. Fig. 4.21 clearly demonstrates that the elastic intensity substantially decreases at the temperature range between 120 K and 160 K. Since c.a. 50% of the adsorbate is supposed to form the monolayer at the gas–graphite interface (see Table 4.3) and it undergoes an order-disorder transition at 138 K, the decrease in intensity up to 138 K should be mainly attributed to its transition. The following large decrease in intensity from 138 K to 160 K indicates that both of the phase transitions (at 150 K and at 160 K) are also accompanied by excitation of molecular motions, suggesting that both of the phase transitions involve

Table 4.3: The amount ratio of each solid phase formed on graphite to the total adsorbate at $\theta > 2$. Note that G/S and S/L stand for the gas–solid interface and the solid–liquid interface, respectively. Only representative results obtained from the entropy values in Table 3.7 are listed below.

	Ratio				
θ	Monolayer		Bulk		
	at G/S	at S/L	α-phase	β-phase	γ-phase
2.99	0.48	0.31	0.21	0	0
4.96	0.06	0.59	0.33	0.02	0
9.99	0	0.21	0.50	0.25	0.04
20.0	0	0.12	0.42	0.39	0.07
40.3	0	0.04	0.31	0.27	0.38

orientational disorder of the molecules. This supports our idea that the transition at 160 K is due to ordering of the plastic α-phase at low temperature, described in Chapter 3. It should be noted here that the elastic intensity did not change dramatically at the melting point of the monolayer formed at the liquid–graphite interface (around 185 K). Furthermore, the magnitude of the residual elastic contribution around 175 K, where an only solid in the system is the monolayer at the liquid-graphite interface, did not reflect the amount of the solid phase, expected to be c.a. 20% of the total adsorbate (see Table 4.3). This may be rationalized by the high mobility of the TMS molecules in the orientationally-disordered phase of the monolayer discussed in the previous section.

As shown in Fig. 3.23, a glass transition was observed at the temperature between 57 K and 68 K, depending on the coverage. The glass did not crystallize in our experiments. However, it is evident that the step height of the heat capacities at the glass transition decreases with increasing the coverage, indicating that the transition could be attributed not to the bulk phases formed on graphite but to the monolayer. Since no glass transition has been found for the TMS monolayer on graphite at $\theta < 2$, i.e., the monolayer formed at the gas–graphite interface, the glass transition is possibly attributed to the monolayer formed at the liquid–graphite interface. As discussed above, the transition of the monolayer at 150 K appears to involve orientational disorder of the molecules. The melting point of the monolayer (around 185 K) is far from the phase transition temperature. Therefore, a likely picture for the glass transition is the freezing of the orientational degrees of freedom of the molecules in the monolayer. Table. 4.4 summarizes the observed entropy changes associated with the solid-solid phase transition of the monolayer. They are converted values per unit mol of the monolayer using the ratios in Table. 4.3. Although the full value of the transition entropy can not be estimated, the value might be comparable to the transition entropy obtained for the monolayer at $\theta < 1$ ($\sim R \ln 6$). If that is the case, there would be some residual entropy associated with the orientational degrees of freedom in the glass state. Possible interpretations for the glass transition might be (i) the monolayer undergoes the glass transition with freezing of the some of the orientational degrees of freedom, or (ii) a part of the monolayer undergoes the glass transition. The former seems to be relatively acceptable from the view point of the homogeneous *phase*. It should be noted here that the considerably small transition entropy obtained for the monolayer at $\theta = 2.99$ is possibly due to the relatively large inaccuracy in the amount ratios estimated at this coverage. This inaccuracy is mainly due to the inaccuracy in the entropy change associated with the melting of the α-phase, as is described in the previous chapter.

Table 4.4: Observed transition entropy of the monolayer formed at the liquid–graphite interface. Note that the values are converted to the quantities per unit mol of the monolayer.

Coverage	$\Delta_{\mathrm{trs}}S$ / JK^{-1}mol^{-1}
2.99	1.9
4.96	6.1
9.99	9.0
20.0	7.5
40.3	5.0

The amount of each solid phase formed for TMS/graphite at $\theta > 2$ can be estimated from the amount ratio listed in Table. 4.3, which is plotted as a function of the coverage in Fig. 4.22. Since the amount of each bulk phase was slightly different from each other depending of the measurement series, the differences are represented by the vertical bars. With increasing the coverage, the bulk phases are formed in the reverse order of the stability of each phase in the *ordinary* bulk solid, as is described in previous chapter (see Table. 3.5). Thus the bulk phases formed near the graphite surface are supposed to be stacked up in the order illustrated in Fig. 4.22. According to our experimental results, all of the system including the bulk phases stacked up on the graphite surface seems to be at equilibrium. Thus, each of the bulk phases is supposed to be a stable phase at its distance from the surface.

The Gibbs energies of the bulk phases formed near the graphite surface are lowered by the potential energies provided by all of the underlying materials, i.e., substrate and admolecules. Fig. 4.23 illustrates the calculated potential curve between a TMS molecule and the graphite surface. The potential function proposed by Steele [77] was used to calculate the adsorbate–graphite potential. In this function, the potential energy is expressed as a Fourier series in the position variables in the lattice plane parallel to the exposed surface plane. For the potential parameters, those adopted in the DREIDING force filed [75] were used. Here, we assumed that the molecule sit on the surface with dipod-down orientation and the center of mass of the molecule is located on the center of a graphite hexagon. For physical adsorption, the adsorption energy is generally in the vicinity of twice as much as the sublimation enthalpy. Since the enthalpy of vaporization of the bulk TMS is 24.2 $\mathrm{kJmol^{-1}}$, the calculated value for the potential well depth, 59.6 $\mathrm{kJmol^{-1}}$, is considered to be the appropriate value. This potential function represents only the interaction between one molecule and the surface. For the actual potential energy by which a molecule locating a certain distance from the surface would be affected, the admolecule–admolecule potential should be taken into account. Thus the actual potential would be larger. In any case, the potential energy provided by all of the underlying materials is so large that it might change the situation of the bulk phases formed near the surface. However, the potential energy can be interpreted as a function of the distance from the graphite surface. Therefore, for any bulk phase of TMS located at the same distance from the surface, the effects of potential energy would be close to each other, and they would not yield the inversion of the stability among the bulk solid phases of TMS.

The fact that the α-phase is initially formed could be understood by the existence of the underlying monolayer. Although no structural information has not been obtained for the monolayer, most likely structure for an orientationally-disordered monolayer of an effectively spherical molecule is a hexagonal structure. Thus, the monolayer at the liquid–graphite interface is supposed to form a hexagonal structure in the high-temperature phase (150 ~ 185 K). Any of the structure of the bulk solid phase also has not been known yet. The most likely structure for the α-phase is supposed to be a certain one with an in-plane close-packed arrangement, such as f.c.c. or h.c.p., because the α-phase is a plastic phase of an effectively spherical molecule. On the other hand, both of the structures of the orientationally-ordered β and γ-phase are perhaps different from the structure of the monolayer. Therefore, because of the structural incommensurablity, neither β nor γ-phase could nucleate on top of the monolayer, and only the α-phase could do. In other words, the βand γ-phase would be unstabilized by the structural incommensurability. This situation is schematically illustrated in Fig. 4.24 by the Gibbs energy diagram. The solid lines drawn at the upper part represent the Gibbs energies of the *ordinary* bulk phases. The Gibbs energies of the α and the liquid phases near the surface would be lowered by the potential energy, which are drawn by the solid lines at the lower part. Since their relative relation on the energy would be not changed, the melting point of the α phase would be also not changed. On the other hand, the β and γ-phase would be unstabilized by the structural incommensurability, and they might become the metastable phase near the surface. Here they are designated by β' and γ', and their Gibbs energies are drawn by the dashed lines at the lower part.

It is the complicated matter why the β-phase becomes most stable than the other solid phases at the certain position from the surface. Although no structural information is available yet, some structural factor might unstabilize the solid phases other than the β-phase. This situation is schematically illustrated in Fig. 4.25. The unstabilized α and γ-phase phases are designated by α' and γ', and their Gibbs energies are drawn by the dashed lines at the lower part.

Since the γ-phase is the stable solid at the *ordinary* bulk phase, the energy relation between the bulk phases would not be changed at the position far from the surface, where no structural factor might be provided by the environment. Thus, γ-phase should be the most stable at this position. This situation is schematically illustrated in Fig. 4.26.

As discussed above, the phase stability among the bulk phases of TMS seems to depend on each structure. Structural study will make the discussion clear.

4.2.2 Dynamical properties

Fig. 4.27 and Fig. 4.28 illustrate the distribution of the average distance of each molecule from the graphite surface, (the left abscissa), and the slope of the mean-square displacement of each molecule (the right abscissa), calculated from MD simulation of TMS/graphite at $\theta = 7.28$. The slope of the mean-square displacement is directly related to the diffusion coefficient. In-plane displacement (Fig. 4.27) and out-of-plane displacement (Fig. 4.28) were calculated separately. At 140 K all the molecules undergo only small translational diffusion along the in-plane directions. The strong peaks at 140 K in Fig. 4.28 suggest that at least two layers are formed. At 180 K the molecules farthest from the surface start to diffuse fairly along the in-plane directions. At 220 K almost all the molecules diffuse fairly, showing that all of the system turn to be a liquid. However, the sharp peak at 220 K in Fig. 4.28 indicates that the molecules in the first layer still form a layer and diffuse along the in-plane directions, suggesting that the behavior of the layer at the liquid–graphite interface is close to a 2-D liquid rather than a 3-D one. Furthermore, the distribution of the slope D becomes broad with increasing the distance d_z, which may reflects the decrease in the potential energy from the underlying materials depending on the distance from the surface.

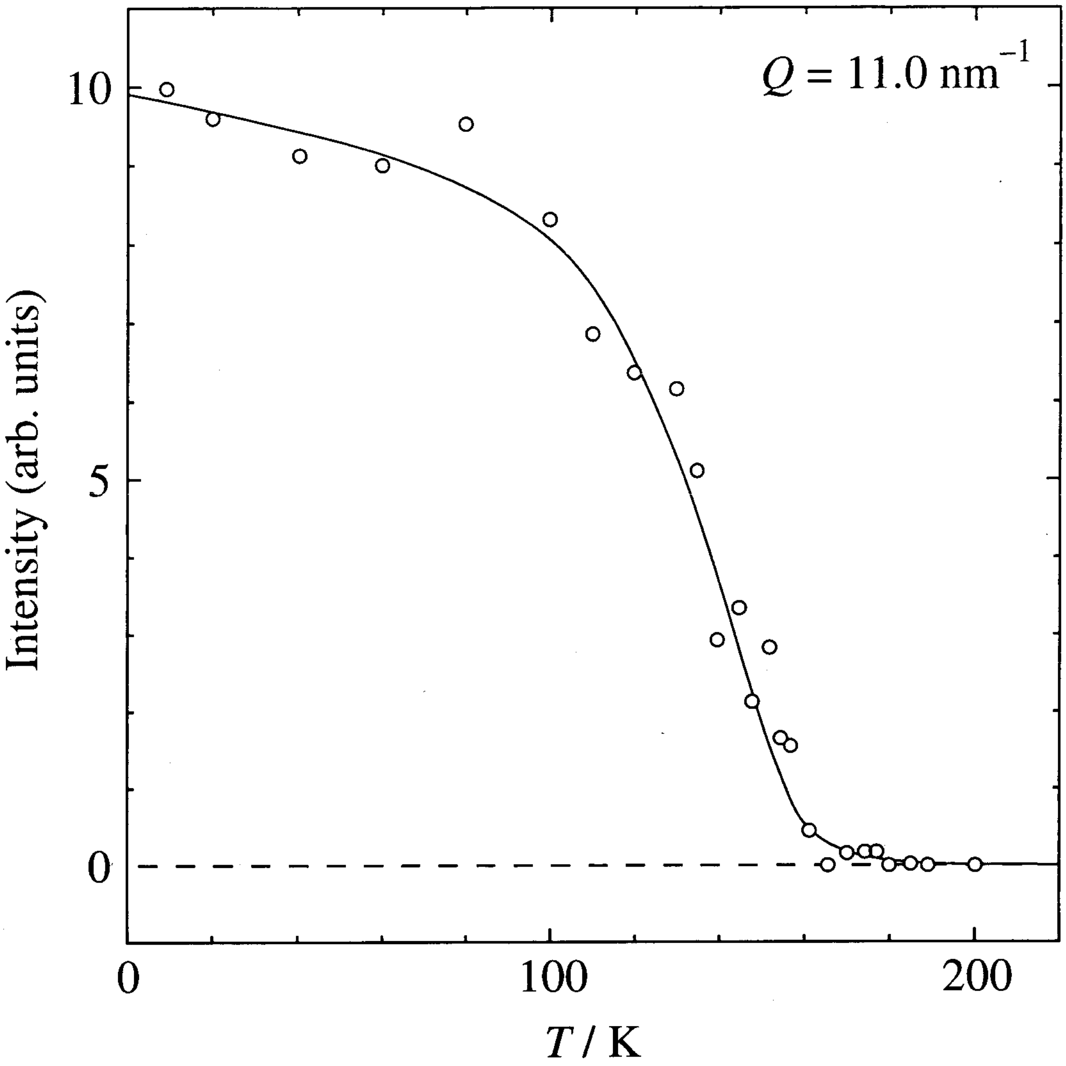

Fig. 4.21: Incoherent elastic scattering intensity for TMS on graphite at θ = 3.04 as a function of temperature obtained on LAM–80ET. The energy resolution was 5.6 μeV at a momentum transfer $Q = 11.0\ \mathrm{nm}^{-1}$.

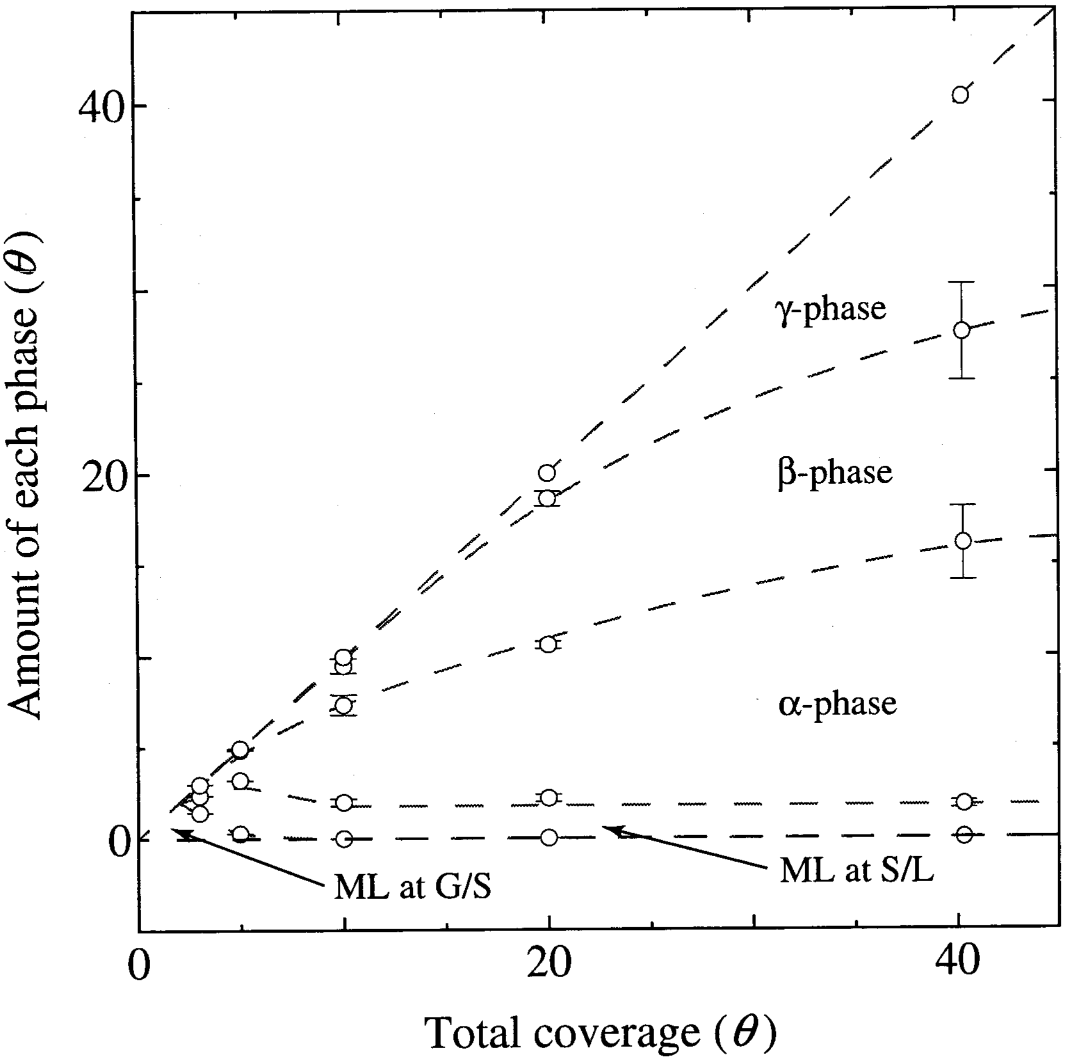

Fig. 4.22: The amount of each solid phase formed in the TMS multilayer on graphite as a function of the total coverage. The vertical bars represents the differences in the amount of each solid phase dependent on the measurement series. Note that G/S and S/L stand for the gas-solid interface and the solid-liquid interface, respectively.

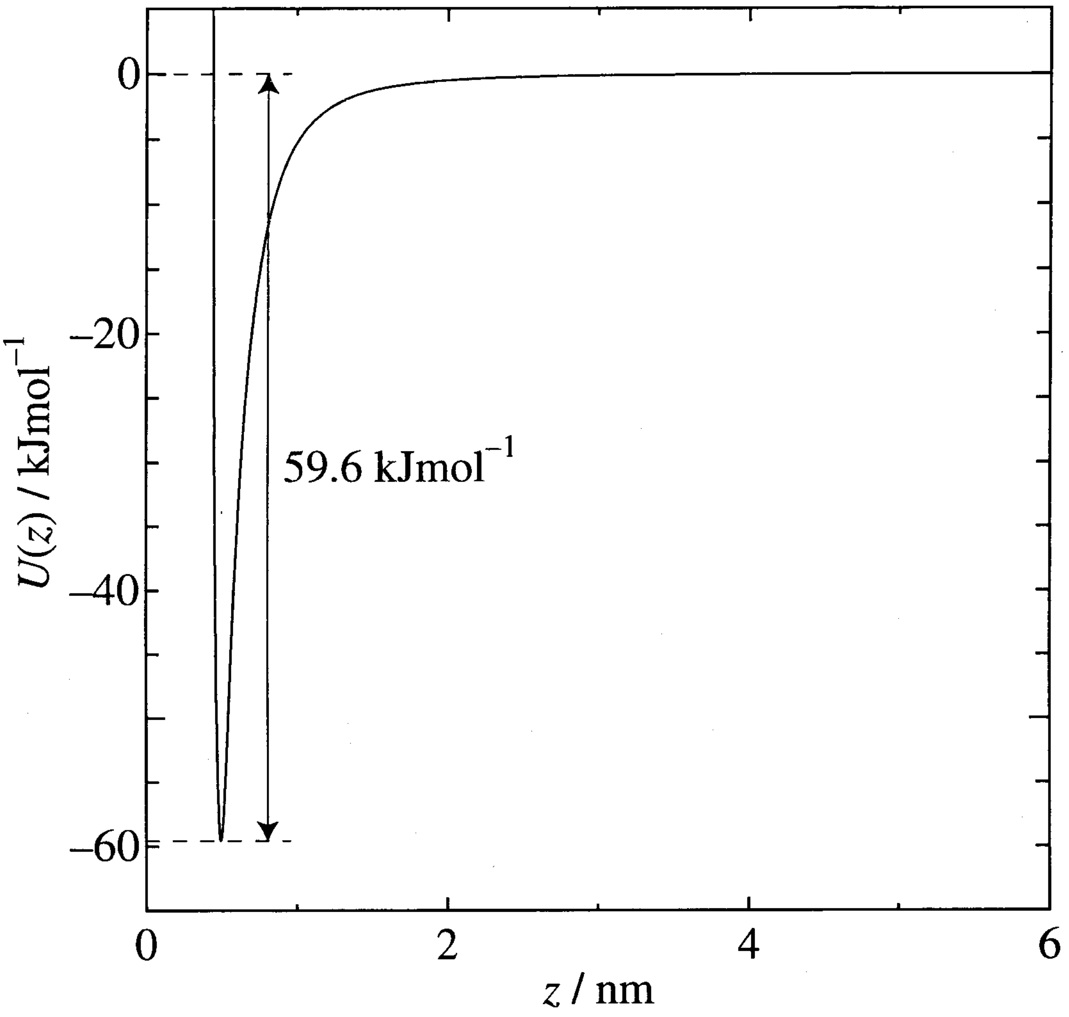

Fig. 4.23: TMS molecule-graphite surface potential curve calculated using the potential function proposed by Steele [77]. The broken line indicates the position of the 6th layer. The inset shows the whole picture of the potential curve.

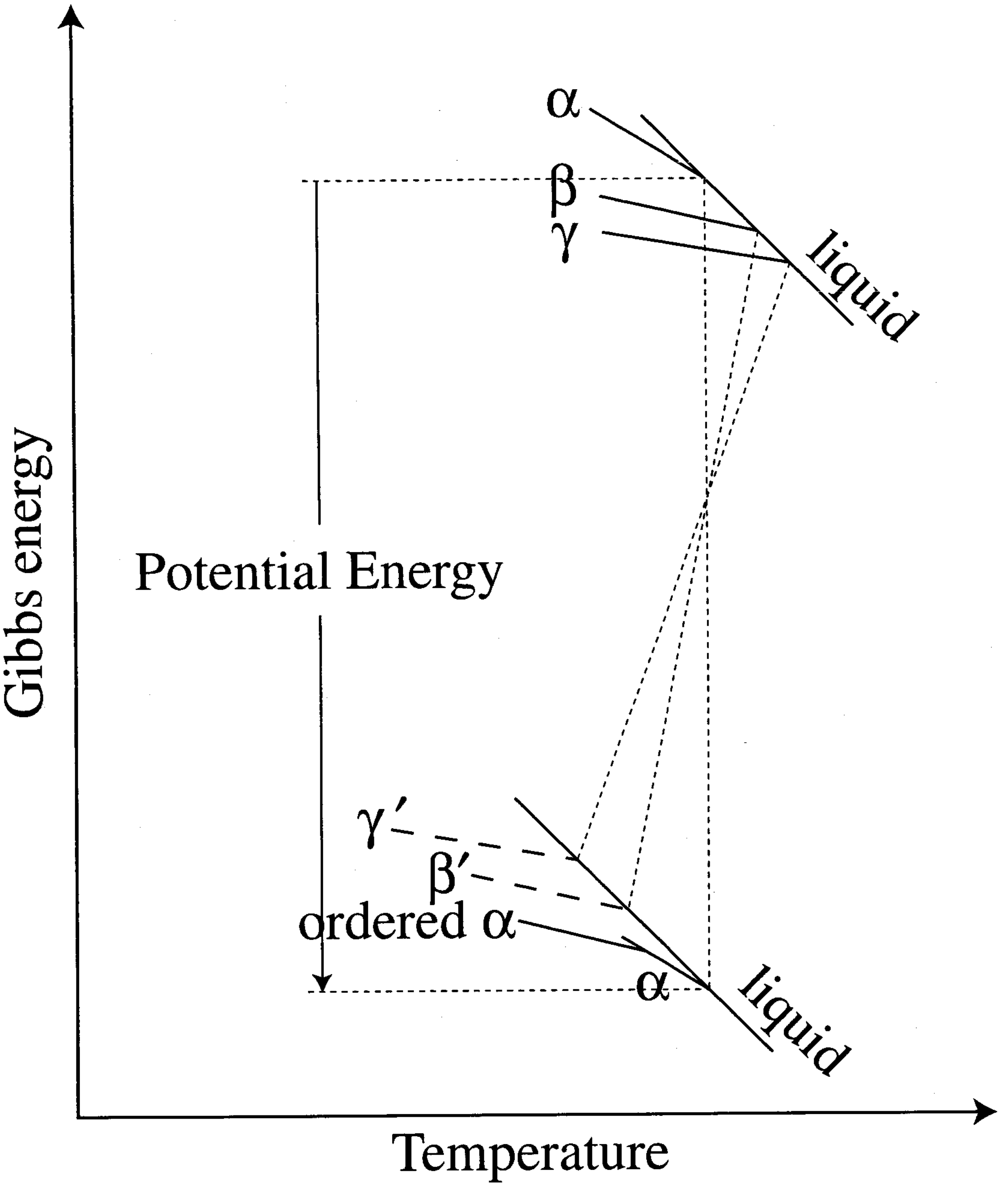

Fig. 4.24: Schematic illustration of the Gibbs energies of the bulk phases formed at the position where the α-phase is most stable. See the details in the text.

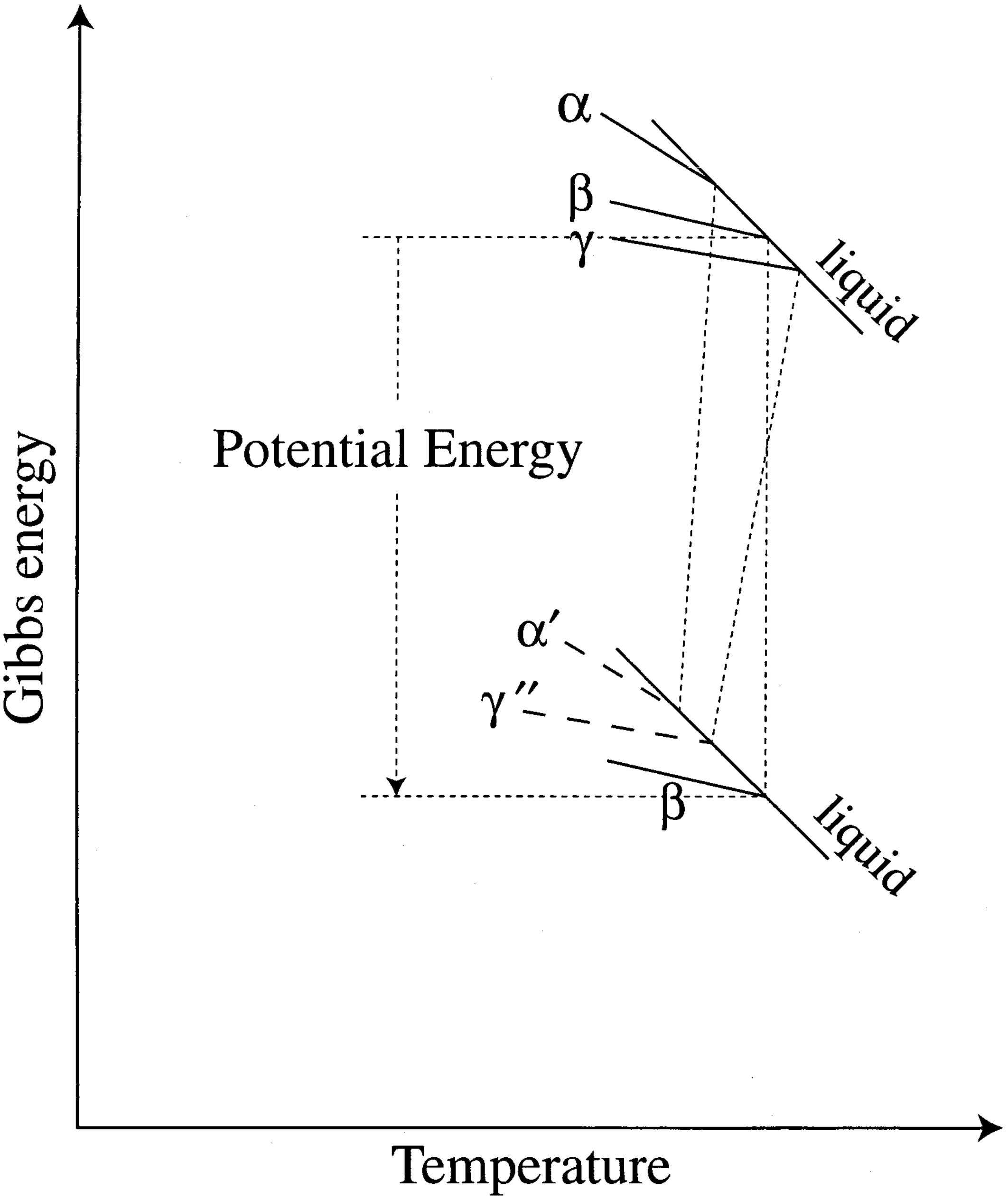

Fig. 4.25: Schematic illustration of the Gibbs energies of the bulk phases formed at the position where the γ-beta is most stable. See the details in the text.

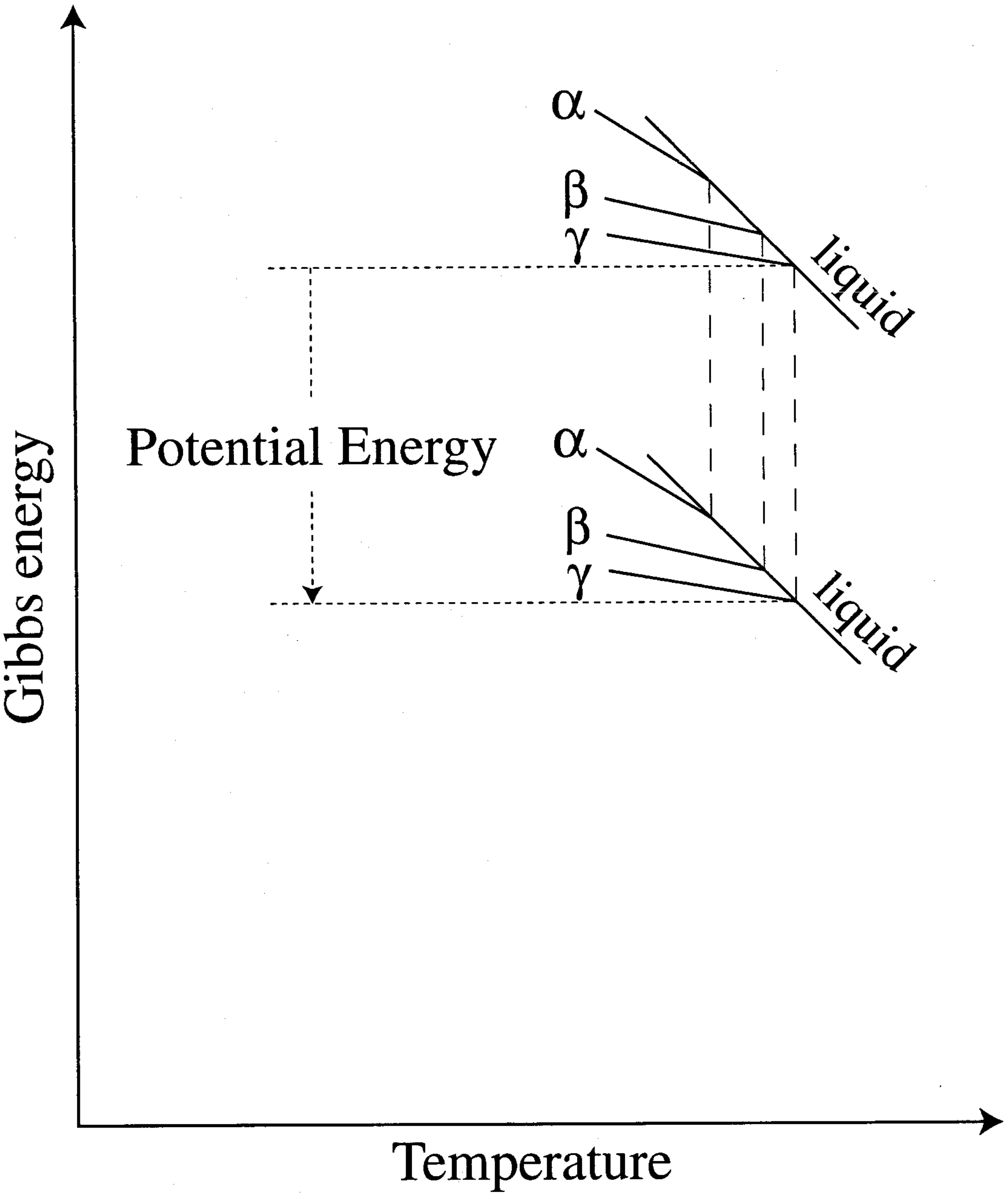

Fig. 4.26: Schematic illustration of the Gibbs energies of the bulk phases formed at the position where the γ-phase is most stable. See the details in the text.

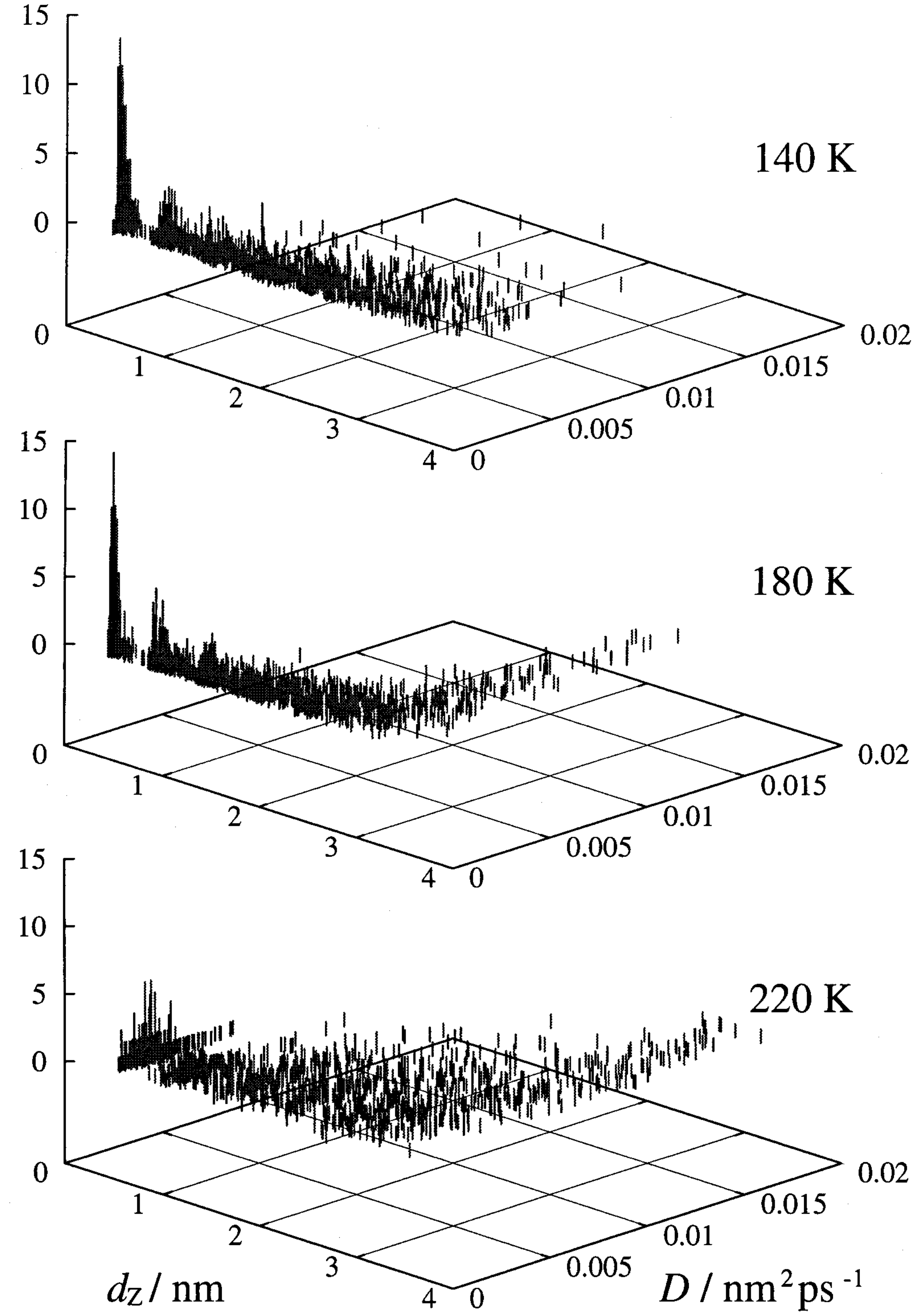

Fig. 4.27: Distribution of the average distance of each molecule from the graphite surface, and the slope of the mean-square displacement of each molecule. Note that the mean-square displacement is calculated with regard to the in-plane displacement.

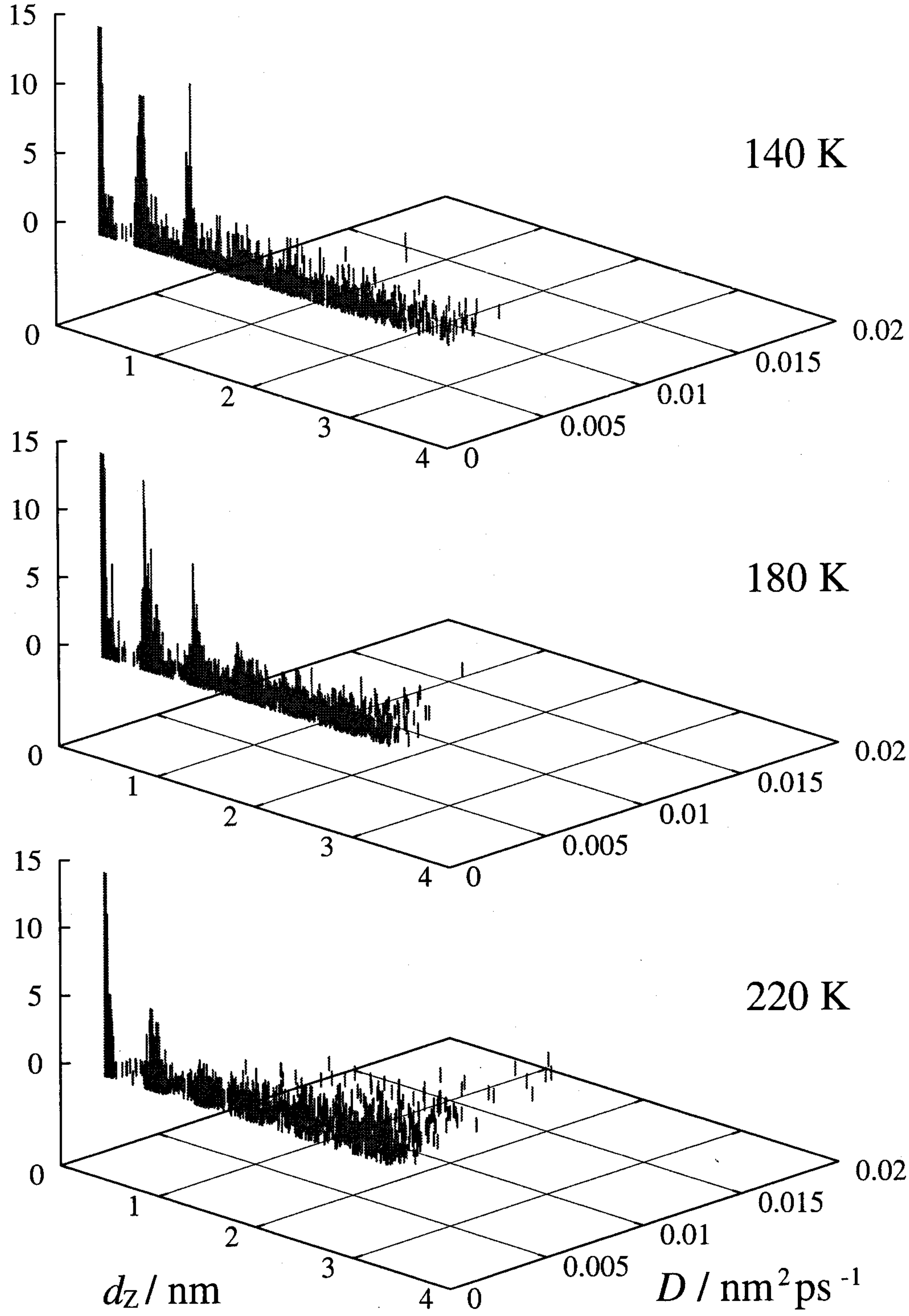

Fig. 4.28: Distribution of the average distance of each molecule from the graphite surface, and the slope of the mean-square displacement of each molecule. Note that the mean-square displacement is calculated with regard to the out-of-plane displacement.

Chapter 5

Conclusion

We have investigated the TMS condensed phase at the mono- and multilayer coverages physically adsorbed both on the surface of graphite on the (100) surface of MgO by means of calorimetry, neutron scattering and MD simulation.

5.1 Monolayer coverage

TMS/graphite

We firstly found a 2-D solid-solid phase transition at 107 K at $\theta < 1$ or at 138 K at $1 < \theta < 2$. The transition involves orientational disorder of the molecules, which has been shown by the large entropy change associated with the transition and the substantial decrease of the elastic intensity of the incoherent neutron scattering across the transition point. Quasielastic scattering components which appear above the transition point are attributed to the molecular motions with different correlation times, the translationally diffusional motion of the molecule and the rotational one. In the high-temperature phase, the molecules are found to undergo fairly excited rotational motion and some of the molecules are supposed to undergo also translational diffusion. Evidences for substantial high mobility of the molecules in the monolayer compared to those in the bulk solid are obtained from the MD simulation as well as from the neutron scattering. We have also pointed out possible formation of a bilayer fluid around T = 220 K. Measurements of the heat of adsorption are required to confirm this model. Vibrational properties of the monolayers were deduced from the incoherent inelastic neutron scattering and MD simulation as well as the low-temperature heat capacities, showing the difference in the lattice vibrations between the monolayer and the bulk solid. This fact is considered to reflect the dimensionality.

One of the most important result of this works is to show the high mobility in the monolayer. Such high mobility is supposed to be one of the nature of the physisorbed monolayers. Further investigations on dynamics of the orientationally-disordered monolayers for various adsorbate–adsorbent systems will give us interesting knowledge on the intermolecular interactions in the monolayers.

TMS/MgO

The monolayer was found to undergo a 2-D solid-solid phase transition around 100 K similar as the one for the monolayer on graphite. However, the molecules on the (100) surface of MgO are less mobile than on the surface of graphite.

5.2 Multilayer coverage

The bulk phases are formed on top of the solid TMS monolayer adsorbed on graphite at low temperature. The solid monolayer persists at the interface between the bulk liquid and the graphite surface, and it melts around 185 K, well above the melting point of any of the bulk solid phases. The monolayer undergoes a solid-solid phase transition at 150 K involving orientational disorder of the molecules. The monolayer also undergoes the glass transition at low temperature (around 60 K). Although the mechanism of the glass transition is not known from our experimental results, it is possibly due to freezing of the some of the orientational degrees of freedom.

The stability among the bulk solid phases was found to be changed near the graphite surface. The α-phase is most stable close to the surface, the γ-phase is most stable far from the surface, and the β-phase is most stable between the region where the α-phase is stable and the one where the γ-phase is stable. The stabilized α-phase formed in this system undergoes a phase transition at 160 K to form an ordered solid at low temperature. We tried to explain the inversion of the stability of the bulk solid phase formed near the graphite surface by the structural commensurability between the solid phase to be formed and the underlying materials. Structural studies on the bulk solid phases as well as on the monolayer are needed to make the discussion clear.

References

[1] J. Timmermans, *J. Chim. Phys.* **25** (1938) 331.

[2] J. N. Sherwood, *The Plastically Crystalline States. Orientationally Disordered Crystals, Wiley, New York, 1979*, p. 186.

[3] J. G. Aston and G. H. Messerly, *J. Am. Chem. Soc.* **58** (1936) 2354.

[4] J. G. Aston, R. M. Kennedy and G. H Messerly *J. Am. Chem. Soc.* **63** (1941) 2343.

[5] L. A. K. Staveley, J. B. Warren. H. P. Paget and D. J. Dowrick *J. Chem. Soc.* (1954) 1992.

[6] H. Enokido, T. Shinoda and Y. Mashiko, *Bull. Chem. Soc. Japan* **42** (1969) 84.

[7] A. J. Valerga and J. E. Kilpatrick *J. Chem. Phys.* **52** (1970) 4545.

[8] T. Shinoda, H. Enokido, Y. Maeda, H. Tomita and Y. Machiko, *Bull. Chem. Soc. Japan* **46** (1973) 48.

[9] M. Harada, T. Atake and H. Chihara, *J. Chem. Thermodyn.* **9** (1977) 523.

[10] J. R. Durig, S. M. Craven and J. Bragin, *J. Chem. Phys.* **52** (1970) 2046.

[11] R. C. Livingston, W. G. Rothschild and J. J. Rush, *J. Chem. Phys.* **59** (1973) 2498.

[12] T. Shinoda, *Bull. Chem. Soc. Japan* **50** (1977) 1382.

[13] G. W. Smith, *J. Chem. Phys.* **42** (1965) 4229.

[14] S. Albert and J. A. Ripmeester, *J. Chem. Phys.* **57** (1972) 2641.

[15] W. C. Allen, N. Liu and J. Jonas, *J. Chem. Phys.* **63** (1975) 3317.

[16] T. Hasebe, G. Soda and H. Chihara, *Proc. Japan. Acad.* **51** (1975) 168.

[17] T. hasebe, G. Soda and H. Chihara, *Bull. Chem. Soc. Japan* **49** (1976) 3684.

[18] T. Hasebe, N. Nakamura and H. Chihara, *Bull. Chem. Soc. Jpn.* **61** (1988) 1803.

[19] A. H. Mones and B. Post, *J. Chem. Phys.* **20** (1952) 755.

[20] T. Atake and H. Chihara, *Chem. Phys. Lett.* **56** (1978).

[21] A. Thomy and X. Duval, *J. Chim. Phys.* **67** (1970) 1101.

[22] H. Taub, K. Carneiro, J. K. Kjems and L. Passell, *Phys. Rev. B*, **16** (1977) 4551.

[23] P. M. Horn, R. J. Birgeneau, P. Heiney and E. M. Hammonds, *Phys. Rev. Lett.* **41** (1978) 961.

[24] R. J. Birgeneau and P. M. Horn, *Science* **232** (1986) 329.

[25] P. W. Stephens, P. Heiney, R. J. Birgeneau and P. M. Horn, *Phys. Rev. Lett.* **43** (1979) 47.

[26] M. Nielsen, J. Als-Nielsen, J. Bohr and J. P. Mctague, *Phys. Rev. Lett.* **47** (1981) 582.

[27] P. W. Stephens, P. A. Heiney, R. J. Birgeneau, P. M. Horn, D. E. Moncton and G. S. Brown, *Phys. Rev. B* **29** (1984) 3512.

[28] U. Volkmann and K. Knorr, *Surf. Sci.* **221** (1989) 379.

[29] T. Shirakami, A. Inaba and H. Chihara, *Thermochim. Acta* **163** (1990) 233.

[30] R. D. Diehl and S. C. Fain, *Surf. Sci.* **125** (1983) 116.

[31] K. Morishige, C. Mowforth and R. K. Thomas, *Surf. Sci.* **151** (1985) 289.

[32] S.-K. Wang, J. C. Newton, R. Wang, H. Taub and J. R. Dennison, *Phys. Rev. B* **39** (1989) 10331.

[33] A. Inaba, T. Shirakami and H. Chihara, *J. Chem. Thermodyn.* **23** (1991) 461.

[34] K. Knorr, *Phys. Rep.* **214** (1992) 113.

[35] A. Inaba, to be published.

[36] W. Caliebe, J. Süssenbach, B. Asmussen and W. Press, *Surf. Sci.* **337** (1995) 92.

[37] H. Schechter, R. Brener, J. Suzanne and S. Bukshpan, *Phys. Rev. B* **26** (1982) 5506.

[38] M. Strzelczyk, N Haack, B Asmussen, J. Süßenbach, W. Press and J. Z. Larese, *Surf. Sci.* **376** (1997) 339.

[39] B. Asmussen, M. Strzelczyk, W. Press and J. Z. Larese, *Surf. Sci.* **406** (1998) 138.

[40] J. P. Coulomb, T. S. Sullivan and O. E. Vilches, *Phys. Rev. B* **30** (1984) 4753.

[41] J. Piper and J. A. Morrison, *Chem. Phys. Lett.* **103** (1984) 323.

[42] J. L. Jordon and J. P McTague, *Surf. Sci.* **150** (1985) L82.

[43] G. Boato, P. Cantini and R. Tatarek, *Phys. Rev. Lett.* **40** (1978) 887.

[44] J. P. Coulomb and O. E. Vilches, *J. Phys. Paris* **45** (1984) 1381.

[45] D. Degenhardt and H. J. Lauter, *Surf. Sci.* **215** (1989) 535.

[46] J. P Coulomb, K. Madih and B. Croset, *Phys. Rev. Lett.* **54** (1985) 1536.

[47] V. Panella, J. Suzanne and J. P Coulomb, *Surf. Sci.* **350** (1996) L211.

[48] M. Trabelsi, J. P Coulomb, D. Degenhardt and H. Lauter, *Surf. Sci.* **377-379** (1997) 38.

[49] K. Madih-Ayadi, A. Celzard, J. P Coulomb, N. Dupont-Pavlovsky, and J. F. Marêché *Surf. Sci.* **443** (1999) 69.

[50] M. V. Smalley, A. Hüller, R. K. Thomas and J. W. White, *Mol. Phys.* **44** (1981) 533.

[51] O. Ferreira, C. C. Colucci, E. Lerner and O. E. Vilches, *Surf. Sci.* **146** (1984) 309.

[52] P. Thorel, J. P. Coulomb and M. Bienfait, *Surf. Sci.* **114** (1982) L43.

[53] J. P. Coulomb and M. Bienfait, *J. Phys. Paris* **42** (1981) 293.

[54] J. P. Coulomb and M. Bienfait, *Faraday Dis. Chem. Soc.*, **80** 79 (1985).

[55] J. P. Coulomb and M. Bienfait, *J. Phys. Paris* **47** (1986) 89.

[56] J. H. Quateman and M. Bretz, *Phys. Rev. B* **29** (1984) 1159.

[57] J. Z. Larese and R. J. Rollefson, *Phys. Rev. B* **31** (1985) 3048.

[58] G. Hess, in: *Phase Transitions in Surface Films*, eds. H. Taub, G. Torzo, H. J. Lauter and S. C. Fain Jr., (Plenum, New York)

[59] M.A. Castro, S.M. Clarke, A. Inaba and R.K. Thomas, *J. Phys. Chem.* **B101** (1997) 8878.

[60] M.A. Castro, S.M. Clarke, A. Inaba, T. Arnold and R.K. Thomas, *J. Phys. Chem.* **B102** (1998) 10528.

[61] S.M. Clarke, A. Inaba, T. Arnold and R.K. Thomas, *J. Thermal Analysis and Calorimetry* **57** (1999) 643.

[62] M.A. Castro, S.M. Clarke, A. Inaba, T. Arnold and R.K. Thomas, *Phys. Chem. Chem. Phys.* **1** (1999) 5203.

[63] M.A. Castro, S.M. Clarke, A. Inaba, T. Arnold and R.K. Thomas, *Phys. Chem. Chem. Phys.* **1** (1999) 5017.

[64] S.M. Clarke, A. Inaba, T. Arnold, R.K. Thomas and M.A. Castro, *J. Phys. Soc. Jpn.* **70** Suppl.A (2001) 300.

[65] M.A. Castro, S.M. Clarke, A. Inaba, R.K. Thomas and T. Arnold, *J. Phys. Chem.* **B105** (2001) 8577.

[66] M.A. Castro, S.M. Clarke, A. Inaba, C.C. Dong and R.K. Thomas, *J. Phys. Chem.* **B102** (1998) 777.

[67] S.M. Clarke, A. Inaba, R.K. Thomas and J. Fish, *J. Phys. Soc. Jpn.* **70** Suppl.A (2001) 297.

[68] H. Preston-Thomas, *Metrologia* **27** (1990) 3.

[69] S. Ikeda, N. Watanabe, K. Inoue, Y. Kiyanagi, A. Inaba, S. Takeda, T. Kanaya, K. Shibata, T. Kamiyama, Y. Izumi, Y. Osaki and C. J. Carlile, *J. Phys. Soc. Jpn.* **60** (1991) 3340.

[70] K. Inoue, Y. Ishikawa, N. Watanabe, K. Kaji, Y, Kiyanagi, H. Iwasa and M. Kohgi, *Nucl. Instr. and Meth.* **A238** (1985) 401.

[71] K. Inoue, T. Kanaya, Y. Kiyanagi, K. Shibata, K. Kaji, S. Ikeda, H. Iwasa and Y. Izumi, *Nucl. Instr. and Meth.* **A327** (1993) 433.

[72] S. Nosé, *Mol. Phys.* **52** (1984) 255.

[73] W. F. van Gunsteren, H. J. C. berendsen, *Mol. Phys.* **34** (1977) 1311.

[74] L. Verlet, *Phys. Rev.* **159** (1967) 98.

[75] S. L. Mayo, B. D. Olafson and W. A. Goddard III, *J. Phys. Chem.* **94** (1990) 8897.

[76] M. Beé, *Quasielastic Neutron Scattering* (Adam Hilger, Bristol and Philadelphia 1988)

[77] W. A. Steele, *Surf. Sci.* **36** (1973) 317.

[78] A. Inaba and J. A. Morrison, *Chem. Phys. Lett.* **124** (1986) 361.

[79] G. B. Guthrie and J. P. McCullough, *J. Phys. Chem. Solids* **18** (1961) 53.

[80] A. Inaba and H. Chihara, *Can. J. Chem.* **66** (1988) 703.

[81] for example, C. Kittel, *Introduction to Solid State Physics*, 7th ed., (Wile and Sons, New York, 1996), p. 122.

[82] D. Fischer, K. Klostermann and K.-L. Oehme, *J. Raman Spectrosc.*, **22** (1990) 19.

[83] N. Sakisato, A. Inaba and T. Matsuo, *J. Thermal Analysis and Calorimetry*, in press.

[84] R. K. Thomas, *Prog. Solid State Chem.* **14**, 1 (1982).